The Dissertation Committee for Vikram Devaraj Certifies that this is the approved version of the following dissertation:

Modeling, Design, Development, and Control of a Pilot-Scale Continuous Coating Line for Proton Exchange Membrane Fuel Cell Electrode Assembly

Committee:

Joseph J. Beaman, Supervisor

Serge M. Prudhomme, Co-Supervisor

Eric P. Fahrenthold

Raul G. Longoria

Jeremy P. Meyers

Modeling, Design, Development, and Control of a Pilot-Scale Continuous Coating Line for Proton Exchange Membrane Fuel Cell Electrode Assembly

by

Vikram Devaraj, B.E.; M.S.E.

Dissertation

Presented to the Faculty of the Graduate School of
The University of Texas at Austin
in Partial Fulfillment
of the Requirements
for the Degree of

Doctor of Philosophy

The University of Texas at Austin
August 2012

To my mother, *for making me believe in myself*

To my father, *for teaching me the art of thinking big*

To my teachers, *for all the knowledge instilled in me*

To Perumal, *for "Mam Ekam Saranam Vrajah"*

and of course

to my little brother, *for putting up with me all the time*

Acknowledgements

I would like to thank Dr. Joseph J. Beaman Jr. for being a wonderful advisor and mentor. I am glad I walked into his office five years ago asking for a research project and words cannot express the happiness and pride I gained being his graduate student. Without his guidance, encouragement and credit card, this research would never have been possible. He always supported me when I tried new things and was there by my side when things did not go as planned.

I spent countless hours with my co-supervisor, Dr. Serge Prudhomme. He taught me the true meaning of the derivative and made me understand, develop, and solve the crazy differential equations that I encountered. When I was clueless on how to proceed, he gave me the hope and confidence that I desperately needed. He treated me like his own student and will be thankful for that forever.

The rest of the committee, Dr. Longoria, Dr. Fahrenthold, and Dr. Meyers, were most helpful and understanding during frantic times. I thank you all for accommodating my requests and questions in the last second. I am proud to have had you in my committee. I also want to thank Dr. Manthiram again for tracking my graduate application when everything was lost. Without his support none of this would be possible.

Probably the biggest hurdle that I faced during my PhD was passing the qualifying exam. If Abhishek “chaddi” Goel, had not “re-taught” the entire undergraduate syllabus to me, I probably would never be in the situation to type this document. I am indebted to his eagerness to share knowledge in the most patient manner possible.

I knew very little in controls before I started this research. Luis Felipe Lopez taught me controls right from the basics and helped me implement it. I met with him morning, evening, and night when I was implementing controls and I will remember the “good times”.

Mark Phillips, Fred “mudbug” Rothhauser, James Sanders, Danny Jares, Curtis Johnson and Michael Slotboom did help me a lot with building the machine, and I consider myself lucky to be their friend. They treated me well and helped me to the fullest extent. I also thank Scott Allen and Aaron Frost for their timely advice and machining suggestions.

A special thanks to Danielle Fournier, Alicia Snyder, Prabhu Khalsa, Rosalie Foster, and Cindy Raman for their superb administrative skills and for making sure that I stayed out of trouble! When I broke my hand, Danielle and Alicia’s personal concern and willingness to help deeply moved me. I am thankful to be a recipient of their care and affection.

Dr. Timothy J Silverman is still one of my best friends and I am indebted to him for helping me solve “YP”s even after he left UT. He did not ignore the desperate calls of a graduate student and I could not have finished this research successfully without his insight and suggestions. Dr. Babar Koraishy was a pillar of strength and shared his insight and intuition when I needed it most. I also thank my other colleagues Abhimanyu Bhat, Kaushik Alayavalli, Gautam Salhotra, Cameron Booth, Dr. Srikanth Tadepalli, Dongwoo Kim, Ahmad El Zaatari, and numerous others who have made invaluable contributions to my research.

I was lucky to have the best batch of interns always and I specially thank Will Scharnberg and Nate Holland for helping me with machine construction and simulation. Will was there from the beginning to the end and I owe him a lot!

I met with some wonderful people and worked on some great projects. Dr. Rodney Horton's ideas and the enthusiasm he brought to the table has never ceased to amuse me.

One of the major driving forces that enabled me to write this dissertation was Dr. James Mikulak. He single handedly helped me correct and fix grammar, sentence construction, and content, in-spite of his extremely busy schedule. I consider him as my mentor and there is a wealth of knowledge with him that I can learn and benefit from. I am glad to be associated with him and once again I am glad I broke his "mold" four years ago!

Everything that I know today is based on what I learned through education, experiences and random hallway conversations. I sincerely thank all my teachers from Chinmaya Vidyalaya, SVCE, UT Austin, Dr. Prudhomme, Saikishan and Chaddi, for their contribution in shaping me.

My friends stood by me during this entire ordeal, and I personally and sincerely thank all them from whom I learned, danced, laughed, ate, fought and did extremely foolish things. When I sit back and look at this journey, there have been good and difficult moments; the interactions I had with the people around me define who I am today and I would never wish it happened any other way.

Vinitha and Mani Subramanian have been my "parents away from home" and will always be grateful for their limitless affection and love. I am glad I came to Austin and will always remember you!

I spent most of my time with Abhimanyu, Akshaya, Aysh, Bharadwaj, Kaushik, Gautam, Irani, Thala, "Left arm", Saikishan and Felipe during the PhD and I also thank them for helping me in the lab till midnight! They probably have to engineer a better, more patient, and understanding roommate than Bharadwaj, and am glad to have his support for everything!

Through Armin Van Buuren, I discovered a new genre of music and it is this music that took the pain away and kept me motivated. During this period, my macbooks, strawberry, and my "Blue Thunder" and "poonai" have still been faithful companions and I probably owe them everything!

This acknowledgement will not be complete if I don't mention my dearest Varun and mother. Varun read this dissertation multiple times and found the smallest of errors in addition to being one of the most important motivating factors to push harder and perform. My parents have always permitted me to do "whatever" I want to do and have supported every decision I have ever made. From the bottom of my soul and the depths of my heart, I want to thank you for everything. The encouragement, love and affection, which my mother and brother have showered on me, make me believe that I am the luckiest man alive! There is lots more coming and this is just the beginning!

VIKRAM DEVARAJ

The University of Texas at Austin
August 2012

This work is supported by the Office of Naval Research MURI grant N00014-07-1-0758.

Modeling, Design, Development, and Control of a Pilot-Scale Continuous Coating Line for Proton Exchange Membrane Fuel Cell Electrode Assembly

Vikram Devaraj, Ph.D.
The University of Texas at Austin, 2012

Supervisor: Joseph J. Beaman

Fuel cells are electrochemical energy devices that convert the chemical energy in a fuel into electrical energy. Although they are more efficient, clean, and reliable than fossil fuel combustion systems, they have not been widely adopted because of manufacturing challenges and high production cost. The most expensive component of a fuel cell is the membrane electrode assembly (MEA), which consists of an ionomer membrane coated with catalyst material. Best performing MEAs are currently fabricated by depositing and drying liquid catalyst ink on the membrane, however, this process is limited to individual preparation by hand due to the membrane's rapid water absorption that leads to shape deformation and coating defects. This work models the swelling and drying phenomena of the membrane and coating during manufacturing, and then applies the results to develop and control a continuous coating line for the production of defect free fuel cell MEAs. A continuous coating line can reduce the costs and time needed to fabricate the MEA, incentivizing the commercialization and widespread adoption of fuel cells.

Membrane swelling is a three-dimensional, transient, coupled mass transfer, heat transfer, and solid mechanics problem. Existing models describe the membrane's behavior in operating conditions, but none predict the behavior during manufacturing. This work develops a novel physics-based model that describes the behavior of the membrane and coating in a continuous manufacturing scenario and incorporates effects that are missing from existing models.

A model that can predict wrinkles, the most commonly observed defect during manufacturing, is presented. Simulation results from the above models are used to design and develop an improved continuous MEA coating process that includes pre-swelling and two-stage drying of the coated membrane. A prototype pilot-scale coating line to implement and test the improved coating process is designed and constructed.

Finally, a Linear-Quadratic-Gaussian type controller is developed using the physics-based model of the manufacturing process to optimally control the temperature and humidity of the drying zones, and its effectiveness when implemented on the coating line is discussed.

Table of Contents

List of Tables

List of Figures

Chapter 1: Introduction

1.1 FUEL CELL

Fuel cells are electrochemical energy devices that convert the chemical energy in a fuel directly into electrical energy. This is achieved by splitting a thermodynamically favorable chemical reaction into two half-cell electrochemical reactions. Catalysts at the anode and cathode of the fuel cell initiate these half-cell reactions. Fuel cells are thermodynamically open systems and can theoretically produce energy as long as the anode is supplied with fuel and cathode with oxidant (Barbir, 2005).

The energy conversion in a fuel cell is done in a single step; hence it is more efficient, cleaner with less harmful emissions, and more reliable than fossil fuel combustion systems (Hayre, 2006). Secondary electrochemical systems like batteries, store a finite amount of energy in their electrodes and recharging them is limited by reaction kinetics and related thermal considerations whereas fuel cells can be renewed by simply adding more fuel to the tank. Power and energy stored can be independently scaled in a fuel cell by modifying the system's stack and tank sizes respectively (Silverman, 2010). These advantages make fuel cells a promising alternative for long-runtime applications such as portable electronics and high-power applications such as vehicle power (Joon, 1998).

Since the original invention of the fuel cell over 160 years ago by Sir William Grove (Koraishy, 2010), several types of fuel cells have been classified based on operating temperatures, fuels and materials systems. The common types of fuel cells and their characteristics are shown in Table 1.1 (Larminie, 2000).

Table 1.1: Summary of common fuel cell types and characteristics

	Electrolyte ion	Cell efficiency	Operating temperature	Applications	Fuel
Proton Exchange Membrane Fuel Cell (PEM fuel cell)	H^+	30 – 70%	20 – 80°C	Portable electronic devices, stationary and mobile applications	Hydrogen, methanol, ethanol, formic acid
Alkaline Fuel Cell (AFC)	H^+	50 – 70%	50 – 200°C	Space vehicles	Hydrogen
Phosphoric Acid Fuel Cell (PAFC)	OH^-	55%	~200°C	Small size stationary power systems	Natural gas
Molten Carbonate Fuel Cell (MCFC)	CO_3^{2-}	55%	~200°C	Medium to large size stationary power systems	Natural gas, biogas
Solid Oxide Fuel Cell (SOFC)	O^{2-}	50 – 70%	600 – 1000°C	Stationary power systems	Methane, butane, propane

There are many types of PEM fuel cells classified based on the fuel used. Hydrogen, methanol, ethanol, and formic acid are some of the fuels used. In this work, only polymer electrolyte membrane or proton exchange membrane (PEM) fuel cells, more specifically direct methanol fuel cells (DMFC) are considered. PEM fuel cells operate at a low temperature and are the most common and simplest type amongst other fuel cell systems. In a typical PEM fuel cell, chemical energy from the fuel is extracted through electrochemical half-cell reactions with an oxidizing agent.

1.2 DIRECT METHANOL FUEL CELL (DMFC)

Direct methanol fuel cell, abbreviated as DMFC, is one of the most widely researched PEM fuel cell systems. Their low operating temperature and high energy density make them an attractive alternative for the consumer electronic device market

(Joon, 1998). DMFCs employ methanol as the fuel, which is preferred for use in the portable electronic device market over the other available fuels for the PEM fuel cell. This is because methanol is easier to store and transport when compared to hydrogen and formic acid (Devaraj, 2009).

1.2.1 Operation of DMFC fuel cells

A classic DMFC with a polymer electrolyte is shown in Figure 1.1. The fuel is a mixture of methanol and water and the oxidant is oxygen (air). At the anode, methanol and water react to produce carbon dioxide, protons and electrons. The protons that are produced migrate from the anode to the cathode side through the polymer electrolyte membrane. It should be noted that the polymer electrolyte membrane (PEM) blocks the passage of all other ions and molecules except protons. Once the protons reach the cathode side, they react with the oxygen to produce water. The electrons generated at the anode flow through the external circuit where they drive an electrical load (Srinivasan, 2006).

The half-cell reactions that occur between methanol and oxygen are shown in Equations 1.1 and 1.2. Since these reactions cannot occur by themselves, catalysts are needed to initiate these reactions. Platinum-ruthenium (Pt-Ru) is the most commonly used anode catalyst while platinum (Pt) is a common cathode catalyst (Dubau *et al*, 2003). There is active research going on to identify a cheaper and more efficient catalyst.

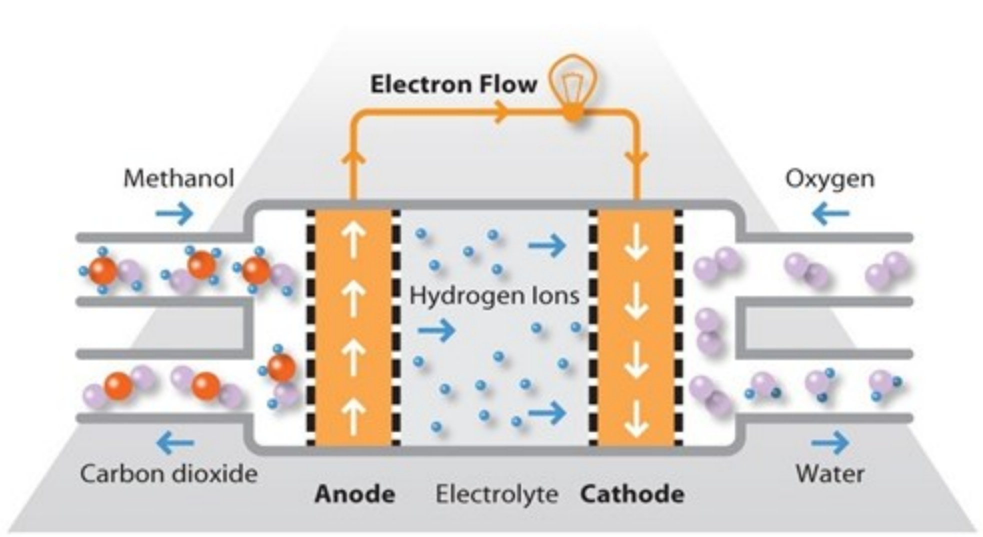

Figure 1.1: Operation of a direct methanol fuel cell (FCT, 2012)

The half-cell and total reactions of the DMFC are

$$\textit{anode reaction}: \mathrm{CH^3OH + H_2O \rightarrow CO_2 + 6H^+ + 6e^-} \tag{1.1}$$

$$\textit{cathode reaction}: \frac{3}{2}\mathrm{O_2 + 6H^+ + 6e^- \rightarrow 3H_2O} \tag{1.2}$$

$$\textit{total reaction}: \mathrm{CH_3OH} + \frac{3}{2}\mathrm{O_2 \rightarrow CO_2 + 2H_2O} \tag{1.3}$$

1.2.2 Components of a DMFC system

The components of a DMFC fuel cell system can be divided into two parts; namely the stack and the balance of plant. The stack consists of multiple DMFC single cells connected in series and is where the electrochemical reactions occur. The balance of plant is responsible for delivering reactants and removing products from the cell. Since a single DMFC cell only produces a voltage of between 0.6 to 0.7 Volts, multiple single cells are connected in series to increase the power capacity. The balance of the plant must also regulate the temperature of the stack and condition the power generated by the stack. The design of the stack thus has a great influence on the system's overall electrical and thermal performance, and is the major challenge in designing and manufacturing a commercially successful DMFC system. (Wheeler and Sverdrup, 2007).

Figure 1.2 shows an illustrated schematic representation of the seven layers or components of each individual cell in a DFMC stack (Silverman, 2010). Starting from the center we find a gas-impermeable, proton conducting, electrically insulating membrane which is called the Proton Exchange Membrane (PEM). The PEM is sandwiched on both sides by catalyst layers. A catalyst layer is typically porous and contains some PEM particles with the electrically conductive catalyst particles. The PEM particles in the catalyst layer are commonly known as the ionomer. The intersection of the catalyst, pore and ionomer provide the reaction sites for the electrochemical reactions.

Figure 1.2: Components of a single cell of a fuel cell stack (Silverman, 2010)

The middle three layers comprising of the PEM and the two catalyst layers are collectively referred to as the membrane electrode assembly (MEA). Products and reactants are distributed to the reaction sites by gas diffusion layers (GDL) as shown above in Figure 1.2. The GDL is typically an electrically conductive sheet of carbon cloth. Moving outward from the GDL are the bipolar plates, as shown also in Figure 1.2, which act to electrically connect the individual cells in series and to also provide channels or pathways to carry the reactants to inner layers and remove the reaction products from inner layers (Hayre, 2006). The bipolar plates provide mechanical support for the MEA, and a pathway to expel the heat generated during operation of the cell.

All the useful electrochemical reactions in a DMFC cell occur in the MEA and it is the single component whose design has the greatest impact on the performance and cost of a fuel cell system (Tsuchiya and Kobayashi, 2004).

1.2.3 Motivation for research

The widespread adoption and commercialization of DMFC fuel cells has been slow, mainly because of the steep costs associated with materials and manufacturing. The costs of materials and manufacturing of the MEA, which again consist of the PEM and the two catalyst layers, make it the most expensive component of a DMFC fuel cell. The most common PEM used in DMFCs is a perfluorinated sulfonic acid, commonly known under the trade name “Nafion”. Nafion is manufactured and trademarked by E.I du Pont de Nemours and Company and is an expensive material with costs at the time of writing running at about $0.35 per square centimeter. Additionally, the catalysts used in the MEA consists of either platinum or an alloy of platinum with another platinum-group metal, which are historically expensive materials. Manufacturing defect-free MEAs has also proven to be expensive as the result of unique set of challenges that will be outlined in the next section. It will greatly benefit the fuel cell industry if alternative materials and cost-effective, defect-free, large-scale manufacturing techniques are developed for the MEA (Mehta and Cooper, 2003).

One part of this research attempts to understand the challenges involved in large-scale manufacturing of MEAs by developing analytical and numerical models of the defects seen during manufacturing of an MEA. As second part of this research, the models are then used to develop an innovative control strategy that is designed to minimize defects when manufacturing MEA modules. Finally effectiveness of this control strategy is demonstrated by using it to control the building of MEA in a custom-built, pilot-scale MEA manufacturing machine.

1.3 MEMBRANE ELECTRODE ASSEMBLY (MEA)

1.3.1 Catalyst coating process and defects

The catalyst layer, as described above and shown in Figure 1.2, is very thin and porous, order of a few microns and is too delicate to be manufactured separately from other components in the DMFC cell. There are three major substrates on which the catalyst layer can be deposited to fabricate an MEA: direct coating of the PEM, direct coating on the GDL, and coating on a decal-transfer medium which is hot pressed onto the MEA later. The catalyst layer is usually formulated as liquid ink and is deposited onto the aforesaid substrates by a variety of coating techniques. Some of the prominent coating techniques include spraying, tape casting, screen-printing, gravure coating and brushing (Mehta and Cooper, 2003) (Vielstich *et al*, 2003).

To manufacture an MEA, one can select a method from the family of available coating procedures and choose a substrate for ink deposition. The performance of the MEA varies based on the choices made. Figure 1.3 illustrates the available manufacturing alternatives in MEA fabrication.

Coating the catalyst layer directly on the PEM exhibits best performance and durability, in addition to it having the fewest manufacturing steps. This can be done in a single process per electrode (anode and cathode) side and it also places the catalyst layer in direct contact with the PEM (Lindermeir *et al*, 2004)(Mao *et al*, 2007). Depositing the catalyst ink on the GDL and a decal-transfer medium, demand a hot-pressing step to assemble the MEA. The pressure required to press the catalyst layers onto the PEM deforms the porous structure of the catalyst layer thereby reducing the sites available for the electrochemical reaction (Prasanna *et al*, 2008).

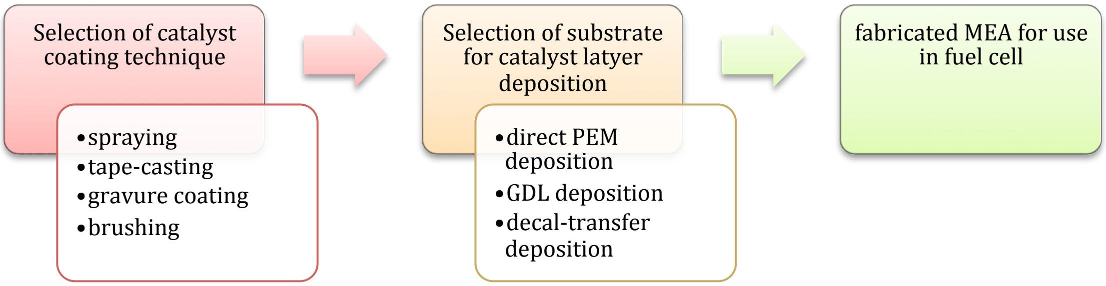

Figure 1.3: Classification of MEA manufacturing alternatives

Although direct catalyst coating of PEM is advantageous with respect to performance, it is most challenging among existing methods. The most significant problem of Nafion is the uptake or absorption of water. The tendency to take up or absorb water causes the PEM to swell and distort, causing wrinkles when the coating is applied on it. Figure 1.4 shows the wrinkles that are formed when ink is applied directly using a tape-casting process.

Figure 1.4: Nafion membrane exhibiting distortion upon contact with liquid ink

This swelling tendency is the main challenge in fabrication of MEA by the direct catalyst coating process. Nafion can swell up to 70% larger than its original volume when exposed to moisture. The wrinkles reappear when the direct catalyst coated PEM is dried (Ladewig, 2007). The wrinkling of Nafion is the single largest reason for coating defects and is the major reason preventing large-scale manufacturing and thus the widespread adoption of fuel cells (Koraishy, 2010). This manufacturing challenge drives the total cost of the MEA up because of wasted catalyst and membrane, both expensive components in a DMFC, in addition to thwarting the fabrication of larger area fuel cells.

1.3.2 State of the art MEA manufacturing

These difficulties in manufacturing have forced the coating of the PEM to be done by hand in small batch processes (Tsuchiya and Kobayashi, 2004). Small pieces of the membrane are held down with a vacuum table and the coating is directly sprayed or brushed on. This process is repeated until the desired thickness of the catalyst layer is achieved.

1.3.3 Existing membrane models

To improve and automate the fabrication of the MEA, it is critical to understand the behavior of the membrane during a typical coating process, which includes exposure to transient, non-uniform water, heat and mechanical stress conditions (Silverman, 2010). Many investigators have extensively modeled the membrane in a fuel cell operating environment (Liu *et al*, 2006)(Springer *et al*, 1991)(Weber and Newman, 2004), but there are fewer models that attempt to model the membrane in a manufacturing environment.

Among the existing models, many are steady-state models and most of them ignore the relationship between swelling and the membrane's water content. The water transport within the membrane is ignored as well (Huang et al, 2006)(Solasi *et al*, 2007)(Solasi *et al*, 2008).

Silverman (2010) was one of the first investigators that attempted a transient, non-uniform model describing water transport, stress and swelling in a membrane.

1.4 CONCLUSION

The MEA in a PEMFC is the single most important component with respect to performance and is also the most expensive and most difficult component to fabricate. Due to the wrinkling problems associated during coating, it is difficult to scale up existing hand-made, batch-type production processes. The industry lacks a well-established, continuous, automated production process to produce high-performance catalyst-coated membranes, which will promote the pervasive commercialization of fuel cells.

The industry will benefit from one such process and the key to such development is to understand the swelling and wrinkling in a manufacturing environment. This research builds upon Silverman's work, with the aim of developing a corrected, restructured and simplified model that can be used to implement model-based control in a custom pilot membrane-coating machine.

1.5 OVERVIEW

In Chapter 2 we develop a complete three-dimensional model that includes the effects of heat transfer, water transport and mechanical stress. We reduce the complexity of this multi-physics, computationally expensive model to make it implementable for real time control. Chapters 3 and 4 deal with the development of the coating model and the wrinkling model respectively. In Chapter 5, we describe the design of the custom pilot-coating machine intended to test the above-mentioned model and to fabricate catalyst-coated membranes in a continuous fashion. We also develop a simplified model of the machine and actuators, which is necessary to implement a model-based controller. Chapter 6 describes the development of the model-based controller and its implementation on the machine. In Chapter 7 we discuss the success of the entire approach and talk about suggestions to continue this research.

Chapter 2: Modeling PEM's swelling

2.1 INTRODUCTION

2.1.1 Background

A key step in the manufacturing of high performance fuel cell membrane electrode assemblies (MEAs), is the direct application of a wet catalyst coating on the proton exchange membrane (PEM). The most common material used for PEMs, is Nafion, which is a sulfonated tetrafluoroethylene that has a hydrophobic polytetrafluoroethylene (PTFE) backbone with hydrophilic sulfonic acid functional groups. When a Nafion membrane is hydrated or exposed to water, the water molecules attach themselves to the clusters of the sulfonic acid functional groups. Volume of the membrane-water system is conserved when the membrane absorbs water and each mole of the membrane can accommodate 22 moles of water, leading to large deformation in the membrane during the hydration process (Hayre, 2006). Figure 2.1 shows an example of large deformations in Nafion that are possible as it absorbs a bead of liquid water. This swelling results in subsequent wrinkling of the membrane and thus makes the application and drying of a wet catalyst ink on to the membrane difficult to accomplish in a satisfactory manner (Frey, 2005).

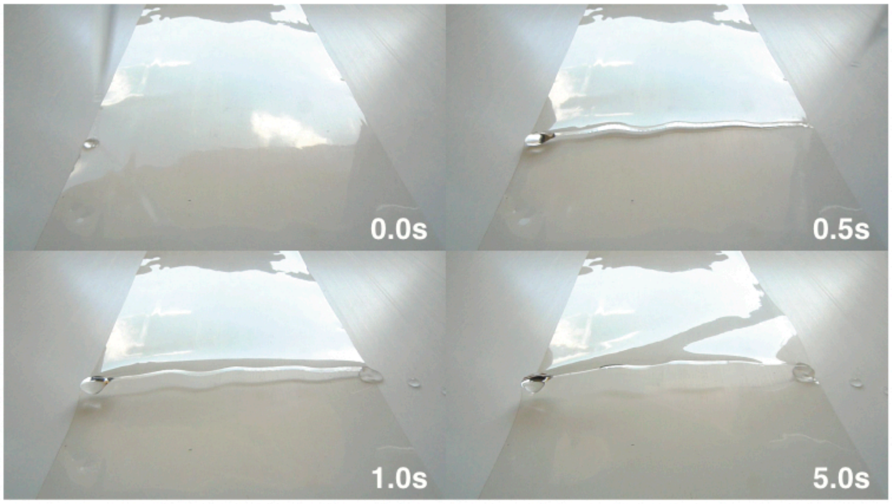

Figure 2.1: A free piece of Nafion undergoing large deformations as it absorbs a bead of liquid water (Silverman, 2010)

Although it is generally assumed that the wrinkling behavior of the PEM is the main cause for manufacturing defects, it should be noted that the manufacturing fuel cell MEAs is still in its infancy and the underlying science of the coating process and it's interaction with membrane is not completely understood. However in the absence of abundant data about the defects in coated membranes, we feel safe in assuming that for the purposes of this work we can consider that wrinkle formation during coating is the major defect that needs to be addressed in order to advance the understanding of this manufacturing process. It should be noted that wrinkles that appear during a continuous fabrication process are not necessarily permanent; some investigators have reported that elastic deformations that occur due to the heat applied in a drying process only become permanent because they are pulled into creases on a roller (Beisel and Good, 2011).

2.1.2 Method of approach

During the manufacture of a high-performance MEA, the membrane goes through a wetting and drying cycle, while the coating which is usually applied after the wetting of the membrane goes through only a drying cycle. And if a continuous roll-to-roll process is used, external forces and thus, stresses have to be applied to the membrane in order to move the membrane. While it is important to understand and model the overall process, it is very difficult to take all these effects, the wetting and drying cycle of the membrane, the application and drying of the coating and the stresses developed by moving the membrane into consideration in a single model. We have thus developed three independent models, which deal with each of the above-mentioned effects. By modeling the effects separately, we are able to develop a more flexible and fundamental understanding of each and then apply those results to the combined actual physical manufacturing system. Additionally the independent models are computationally less intensive.

We start by developing a swelling model for the PEM, which accounts for the wetting and drying of a free piece of membrane. This model will allow us to predict the movement of water into, out and within the membrane under various conditions.

The second model we develop is a coating model that primarily focuses on the drying of the coating. Although water is the main solvent in the coating, its method for desorption is different when compared to the PEM. Hence we have developed a separate set of equations that describe the evolution of water content in the coating. In order to model the entire coating process, the swelling and coating models can be used in conjunction with each other, with the appropriate interfacial boundary conditions.

It is important to note that the swelling or coating models do not include or account for any of the applied tractions. The induced stresses are separately calculated in our third model, the wrinkling model. To predict if the PEM wrinkles under a set of given operating conditions during coating, the water profiles from the combined swelling and coating models are supplied as input to the wrinkling model. The wrinkling model was extensively used, in later stages of this work to aid in designing the pilot coating machine.

The membrane model that was developed is material independent. We simulated these models by applying them to Nafion, but these can be implemented for an alternative membrane like SPEEK (sulfonated poly ether ether ketone), by changing the input parameters and related constants.

Figure 2.2 lists the assumptions, the inputs and the outputs of the three models. The swelling and coating models are designed to be solved in real-time, to allow a later implementation of a model-based controller, which will be addressed at later in this work. The wrinkling model then helped in determining the nominal operating conditions and ultimately the design of the pilot-scale coating machine.

In this chapter, we present the membrane-swelling model. The coating and wrinkling are presented in the subsequent chapters.

Swelling model

- Knowns:
  - Membrane's exterior (hydrating/drying) and initial conditions
- Solves for:
  - Water movement and distribution within the membrane
  - Evolution of water content over time
- Assumptions:
  - Membrane is free to expand/contract with no applied stresses

Coating model

- Knowns:
  - Ink's initial conditions
  - Coating's drying conditions
- Solves for:
  - Evolution of coating's water content over time
- Assumptions:
  - Coating is free to contract with no applied stresses

Wrinkling model

- Knowns:
  - Water profile of the membrane (coated/uncoated)
  - Applied external stresses
- Solves for:
  - Total stresses in the membrane
  - Predicts wrinkling (buckling)

Figure 2.2: The highlights of the three models

2.2 MULTI-PHYSICS SWELLING MODEL

2.2.1 Assumptions

In this three-dimensional model, we model water as a dissolved species within the membrane. A Lagrangian reference frame is used to denote the infinitesimal control volume. In other words, our control volume is fixed with respect to the membrane. The membrane is thus free to expand/contract based on its water content.

The deformation due to change in water content of the membrane is considered elastic. Since we are applying an infinitesimal strain theory, this model is considered or expected to be accurate for reasonably small deviations from the initial conditions.

The model describes physical phenomena associated with mass transfer, heat transfer and solid mechanics. The quantities tracked are the molality of water (number of moles per unit mass), temperature of the membrane, and induced stress represented by

m_0, T, and $\mathbf{T}$, respectively. The membrane can lose or gain water and heat from all the six exposed surfaces.

Water movement inside the membrane is modeled by diffusion and since the concentration of the dissolved water is high, we are unable to assume this to be a dilute solution of water and membrane. We additionally consider the interaction and the resulting resistive drag forces between the water and membrane molecules.

2.2.2 Water Transport

Governing Equations

Membrane and water are the only species present in the system and the generalized continuity equation for a multi-component system is given by (Bird *et al*, 2007)

$$\frac{\partial c_i}{\partial t} + \nabla \cdot \boldsymbol{N}_i = R_{p,i} \tag{2.1}$$

where c_i is the molar concentration, $\boldsymbol{N}_i$ is the molar flux, $R_{p,i}$ is the molar production or consumption rate of species i. Subscript i denotes the relevant quantity for chemical species i. Water is denoted with $i = 0$ and membrane with $i = m$.

In our system, although our control volumes are fixed with respect to the membrane, they are free to change size and shape in response to the swelling effect and thus do not contain a fixed volume. It is inconvenient to express water content when the amount of water and the total volume of the solution keeps changing.

However, the control volume contains a fixed mass of the membrane that does not change with time and hence it is better to express the membrane's water content as a molality rather than a molarity. Molality is defined as the number of moles of water per unit mass of membrane. The relationship between molarity and molality of water is

$$c_0 = \frac{m_0 \rho_m}{1 + \varepsilon_v} \tag{2.2}$$

$$\varepsilon_v = \frac{V - V_0}{V_0} \tag{2.3}$$

where ρ_m is the density of the dry membrane, ε_v is the volumetric strain, V is the total volume that changes with time and V_0 is the reference volume of the dry membrane. In this case, the reference volume is the volume in the absence of swelling, thermal expansion, and stresses.

By using the chain rule, the partial time rate of change of the molarity in Equation 2.1 is

$$\frac{\partial c_i}{\partial t} = \frac{\rho_m}{\varepsilon_v + 1}\frac{\partial m_0}{\partial t} - \frac{\rho_m m_0}{(\varepsilon_v + 1)^2}\frac{\partial \varepsilon_v}{\partial t} \tag{2.4}$$

When Equation 2.4 is substituted in 2.1, and when this is written for water, the conservation equation now becomes

$$\frac{\rho_m}{\varepsilon_v + 1}\frac{\partial m_0}{\partial t} - \frac{\rho_m m_0}{(\varepsilon_v + 1)^2}\frac{\partial \varepsilon_v}{\partial t} + \nabla \cdot \boldsymbol{N}_0 = 0 \tag{2.5}$$

when $R_{p,i} = 0$, since no water is produced or consumed. It should also be noted that, the conservation Equation 2.1 is written only for water with $i = 0$, since the amount of membrane is constant over time and does not change.

The movement of the absorbed water inside the membrane is modeled using multicomponent diffusion. The general equation for the movement of chemical species in a multicomponent mixture is governed by (Newman and Thomas-Alyea, 2004)

$$c_i\left(\nabla\mu_i + \bar{S}_i \nabla T - \frac{\boldsymbol{M_i}}{\rho}\nabla p\right) - RT\sum_j \frac{c_i\, c_j}{c_T\, \mathcal{D}_{ij}}\left(\frac{D_j^T}{\rho_j} - \frac{D_i^T}{\rho_i}\right)\nabla lnT = RT\sum_j \frac{c_i\, c_j}{c_T\, \mathcal{D}_{ij}}\,(\boldsymbol{v}_j - \boldsymbol{v}_i) \tag{2.6}$$

where μ_i is the chemical potential, $\bar{S}_i$ is the partial molar entropy, $\mathcal{D}_{ij}$ is the multicomponent diffusion coefficient, D_i^T's are the thermal diffusion coefficients and $\boldsymbol{v}_i$ refers to the velocity of the moving species i. c_T refers to the total concentration of the entire system.

Equation 2.6 relates the various driving forces for diffusion to the resistive forces due to the relative motion of the species. It considers three different driving forces on the diffusing chemical species, which in our case is water. The terms with $\nabla\mu$, ∇T, and ∇p, refer to the driving forces due to gradients in chemical potential, temperature, and pressure, respectively. The temperature gradients are very modest and thus can be neglected (Silverman, 2010).

The terms involving ∇lnT refer to thermal diffusion, more commonly known as *Soret effect*, which describes the variation of composition of the solution arising from a temperature gradient. This effect does not refer to the diffusing species, but applies to the matrix into which the diffusion is occurring. In simpler terms, in our membrane water system, this effect refers to the compositional gradient in the membrane due to the temperature gradient, and quantifies the driving force that arises from it. *Soret effect* is not important in industrial systems (Newman and Thomas-Alyea, 2004), especially if one of the species is stationary and is ignored in this model.

Finally the term on the right-hand side refers to the drag force that is encountered due to molecular collisions.

Equation 2.6 is a form of the Maxwell-Stefan equation (Newman and Thomas-Alyea, 2004), and it should be noted that there are no acceleration terms present. In this steady state form of the equation, it is assumed that the velocity of the diffusing species reach steady state within a few molecular collisions once diffusion starts.

Equation 2.6 when neglecting the *Soret effect* and the driving forces arising due to gradients in temperature, reduces for water in our system as

$$c_0\left(\nabla\mu_0 - \frac{M_{\mathbf{0}}}{\rho}\nabla p\right) = RT\frac{c_0\, c_m}{c_T\, \mathcal{D}_{0m}}(\boldsymbol{v}_m - \boldsymbol{v}_0) \tag{2.7}$$

Since we are solving the continuity equation in a fixed reference frame with respect to the membrane, $\boldsymbol{v}_m = 0$. We get an expression for the velocity of water, $\boldsymbol{v}_0$, by rearranging Equation 2.7

$$\boldsymbol{v}_0 = -\frac{c_T\mathcal{D}_{0m}}{RTc_m}\left(\nabla\mu_0 - \frac{M_{\mathbf{0}}}{\rho}\nabla p\right) \tag{2.8}$$

In Equation 2.5, the water flux, $\boldsymbol{N}_0$, can be expressed as the product of its concentration and velocity

$$\boldsymbol{N}_0 = c_0\boldsymbol{v}_0 \tag{2.9}$$

and by replacing the velocity from Equation 2.8 in Equation 2.9, one gets

$$\boldsymbol{N}_0 = -\frac{c_0\, c_T\mathcal{D}_{0m}}{RTc_m}\left(\nabla\mu_0 - \frac{M_{\mathbf{0}}}{\rho}\nabla p\right) \tag{2.10}$$

The pressure gradient ∇p will be available from the solid mechanics solution, which is derived later in this chapter. The other undefined variables in Equation 2.10 are c_m, c_T, and $\nabla\mu_0$. The membrane and total concentrations are given by

$$c_m = \frac{\rho_m}{(1+\varepsilon_v)EW} \tag{2.11}$$

$$c_T = c_0 + c_m = \frac{\rho_m}{1+\varepsilon_v}\left(m_0 + \frac{1}{EW}\right) \tag{2.12}$$

where EW is the equivalent weight of Nafion.

Getting an expression for $\nabla\mu_0$ is more elaborate, and it is important to understand the reason for using the chemical potential gradient as opposed to using the concentration gradient directly. The fundamental driving force for diffusion is the activity gradient. Activity gradients are identical to concentration gradients only at very dilute concentrations. At higher concentrations, there is a discrepancy between the activity gradients and the concentrations and it is widely accepted that the chemical potential gradient gives a more accurate representation of the activity than concentration. Moreover, it is very difficult to measure the concentration gradient accurately without introducing external influences, while the chemical potential can be accurately calculated based on the states of the system (Newman and Thomas-Alyea, 2004).

The chemical potential for species i is defined as

$$\mu_i = \frac{\partial G}{\partial n_i} \tag{2.13}$$

where G is the Gibbs free energy and n_i refers to the number of moles or equivalents of species i.

Meyers and Newman (2002), proposed a form for the Gibbs free energy in a multicomponent membrane

$$G = RTn_m \ln \lambda_m^{\circ} + RT \sum_{j \neq m} n_j \left[ln\left(m_j \lambda_j^{\theta}\right) - 1 \right] + RTn_m EW \sum_{i \neq m} \sum_{j \neq m} E_{ij} m_i m_j + \cdots \tag{2.14}$$

where m_i is the number of moles of species i per mass of dry membrane, λ_j^{θ} is the secondary reference state activity for j and E_{ij} is the binary interaction parameter for species i and j. To understand the significance of the secondary reference state, it is important to define the primary reference state. Thermodynamics teaches us that, the absolute chemical potential for any element or compound cannot be defined. It is defined only relative to an arbitrary datum that is called the primary reference state. In most cases, the primary reference state is 298.15 K and 1 bar pressure. The chemical potential at the primary reference state is defined as zero.

The chemical potential of species in a mixture will depend on the composition of the mixture. It is a convention to define an “ideal” dependence of the chemical potential on composition, and to define λ^{θ} that describes the deviation from that ideal state. This new ideal state gives rise to a secondary datum called the secondary reference state. Our quantities are referred to a secondary reference state of saturated water conditions, indicated with a $\star$. Rewriting Equation 2.14 for our system and neglecting the higher-order interactions other than pairwise interactions

$$G = n_m \mu_m^{\star} + RT \sum_{i \neq m}^{n} n_i [\ln(m_i \lambda_i^{\star}) - 1] + RT n_m EW \sum_{i \neq m} \sum_{j \neq m} E_{ij}^{*} (m_i - m_i^{\star})(m_j - m_j^{\star}) \tag{2.15}$$

When membrane and water are the only species present, the Gibbs free energy of a system is given by

$$G = n_m \mu_m^{\star} + RT n_0 [ln(m_0 \lambda_0^{\star}) - 1] + RT n_m EW E_{00}^{*} (m_0 - m_0^{\star})(m_0 - m_0^{\star}) \tag{2.16}$$

Hence, the chemical potential of water in the membrane is

$$\mu_0 = \frac{\partial G}{\partial n_0} = RT ln(m_0 \lambda_0^{\star}) + 2RT E_{00}^{*} (m_0 - m_0^{\star}) \tag{2.17}$$

where, the relationship $m_0 = n_0/(n_m EW)$, was used in the partial differentiation.

The chemical potential gradient for water can be obtained from Equation 2.17, and the binary interaction parameter E_{00}^{*} is fitted to experimental water uptake data (Silverman, 2010)

$$\nabla \mu_0 = RT \frac{\nabla m_0}{m_0} + 2RT E_{00}^{*} \nabla m_0 \tag{2.18}$$

Inserting Equations 2.11, 2.12 and 2.18 into 2.10, we get the complete expression for $\boldsymbol{N}_0$

$$\boldsymbol{N}_0 = \frac{m_0 \rho_m}{1 + \varepsilon_v} (m_0 EW + 1) \mathcal{D}_{0m} \left[-\left(\frac{1}{m_0} + 2E_{00}^{*} \right) \nabla m_0 + \frac{M_0}{RT} \frac{1 + \varepsilon_v}{\rho_m (1 + M_0 m_0)} \nabla p \right] \tag{2.19}$$

which is the final form used in our simulations.

To summarize, Equations 2.5 and 2.19, form the system of governing equations for the water transport portion of the three-dimensional multi-physics model.

Boundary Conditions

As mentioned before, a surface evaporation boundary condition is prescribed at the membrane's surface interfaces and we assume a chemical potential driving force to move water into and out of the membrane. The flux at the free boundary can hence be defined as

$$\boldsymbol{N_0} = \begin{cases} \alpha_{\mu,ads}(\mu_{0,eq} - \mu_{0,s}) & \text{for } \mu_{0,eq} > \mu_{0,s} \\ \alpha_{\mu,des}(\mu_{0,eq} - \mu_{0,s}) & \text{for } \mu_{0,eq} > \mu_{0,s} \end{cases} \tag{2.20}$$

where $\alpha_{\mu,ads}$ and $\alpha_{\mu,des}$ are the adsorption and desorption coefficients for a chemical potential driving force. $\mu_{0,eq}$ is the chemical potential of water in the membrane when it has come to equilibrium with the surroundings. This $\mu_{0,eq}$ is called the equilibrated chemical potential and can be obtained from experiments. $\mu_{0,s}$ is the chemical potential that is computed on the boundary.

The absorption and desorption occur at different rates for Nafion (Silverman *et al*, 2010), hence the need to identify the two parameters $\alpha_{\mu,ads}$ and $\alpha_{\mu,des}$ arises.

It is also possible to simulate a small portion of a large membrane, in which case, the symmetry boundary condition shown in Equation 2.21 should be used on the appropriate planes of symmetry

$$\boldsymbol{N_0}.\hat{n} = 0 \tag{2.21}$$

Application of general membrane model to Nafion

Since there is no one authoritative source for the properties of Nafion, we have attempted to select the most relevant and complete source from literature. It is not feasible to measure all the required properties in-house because of the diverse scope and equipment needed.

The reported values for some parameters vary as much as an order of magnitude. In such cases, we performed some simple tests to estimate the values or we used the values that best matched our experiments.

Equilibrium water content

It has been shown that the amount of water contained in a free-swelling piece of Nafion when it has reached equilibrium with its surroundings is a function of the temperature and water activity. Water activity is related to the relative humidity and is expressed between 0 and 1. Zawodzinski *et al* (1993) expressed the water content as a ratio, λ, of moles of water to equivalents of the membrane. The advantage of expressing the water content by this ratio is that it is independent of the size of the membrane and comparisons between two different pieces of Nafion that have different dimensions can be done easily. The relationship between m_0 and λ is defined in

$$\lambda = m_0 EW \tag{2.22}$$

The thermodynamic model of Meyers and Newman (2002) was used to obtain the relationship between the membrane's water content λ, and its temperature T and water activity a_0

$$a_0 = 46.83\times10^{-3} + 958.2\times10^{-3}\mathrm{erf}\,(-69.56\times10^{-3} + 62.87\times10^{-3}\lambda + 277.3\times10^{-6}\lambda T) \tag{2.23}$$

where erf (x) is the Gauss error function defined by

$$erf(x) = \frac{2}{\sqrt{\pi}}\int_0^x e^{-t^2}dt \tag{2.24}$$

Equation 2.23 can be inverted so that the water content λ can be calculated from T and a_0

$$\lambda = \frac{695600 + 1\times10^7 erf^{-1}(-0.0491292 + 1.0491 a_0)}{628700 + 2773T} \tag{2.25}$$

where, erf^{-1} is the inverse function of erf.

If the surrounding's temperature and the water activity are used as arguments in Equation 2.25, the resulting water content is Nafion's equilibrated water content. This equilibrated water content can be used to quantify the initial conditions at the beginning of the simulation. It is also used to calculate $\mu_{0,eq}$ (or similar), which is the driving force for interfacial mass transport.

Diffusion Coefficient

Values of the diffusion coefficient of water in Nafion, $\mathcal{D}_{0m}$, as reported in the literature, vary between $5\times10^{-9}\ \mathrm{cm}^2/s$ to $2.5\times10^{-5}\ \mathrm{cm}^2/s$ (Burnett *et al*, 2006)(Ge *et al*, 2005)(Majsztrik *et al*, 2008). The wide range of values is the result of the variations in water content and temperature, and also differing measurement techniques and assumptions (Silverman, 2010).

For our simulations, we use a temperature and composition dependent diffusion coefficient fitted by Weber (2004). This curve fitting was done under a chemical potential driving force and is adopted in our simulations because of the similarity of other assumptions

$$\mathcal{D}_{0m} = \left(1.8\times10^{-5}\,\frac{\mathrm{cm}^2}{s}\right) f_v \exp\left[\frac{20kJ\ /\ mol}{R}\left(\frac{1}{303.15\ \mathrm{K}} - \frac{1}{T}\right)\right] \tag{2.26}$$

where f_v is the volume fraction of water and is denoted by

$$f_v = \frac{m_0 M_0 \rho_m}{\rho_0(1+\varepsilon_v)} \tag{2.27}$$

Interfacial Mass Transport Coefficient

The transfer of water across the free boundary of the membrane, which is also called the membrane-gas interface, is the rate-limiting step during sorption and desorption (Silverman, 2010). It should be noted that although this rate-limiting step determines the amount of water exchanged at the membrane-gas interface, the rate depends on the surrounding conditions. For example, a strip of fully saturated Nafion, will dry quicker if it is dried with moving air when compared to placing it in a quiescent chamber which has an identical temperature and water activity to the moving air.

Satterfield and Benziger (2008) published a temperature-dependent expression for $\alpha_{c,ads}$ and $\alpha_{c,des}$, given as

$$\alpha_{des} = 10.2\frac{cm}{s}\exp\left(-\frac{31\mathrm{kJ/mol}}{RT}\right)$$
$$\alpha_{ads} = \frac{\alpha_{des}}{2} \tag{2.28}$$

for a mass transport barrier determined for a concentration driving force

$$\boldsymbol{N_0} = \alpha_c(c_{0,s} - c_{0,eq}) \tag{2.29}$$

where $c_{0,eq}$ is the concentration of water at equilibrium with the environment and $c_{0,s}$ is the membrane's free surface concentration. Subscripts des and ads refer to desorption and adsorption respectively.

In our model, the driving force for convection is the chemical potential; interfacial mass transport barrier for a chemical potential driving force is not readily defined, because of which we use Equation 2.28 as the boundary condition at the membrane-gas interface. Converting the molality into molarity at the membrane surface using Equation 2.2 accomplishes this. This conversion essentially implies

$$\boldsymbol{N_0} = \alpha_c(c_{0,s} - c_{0,eq}) = \alpha_\mu(\mu_{0,s} - \mu_{0,eq}) \tag{2.30}$$

which is acceptable as they quantify the same amount of water transferred across the membrane-gas boundary, with two different driving forces.

It should be noted that Satterfield and Benziger's (2008) expressions for $\alpha_{c,ads}$ and $\alpha_{c,des}$, are for quiescent conditions. During continuous MEA fabrication, the membrane will be exposed to moving air generated by fans and heater assembles. The appropriate $\alpha_{c,des}$ was estimated from drying experiments.

In summary, to predict the water content movement inside the membrane we consider two driving forces, namely the chemical potential and the pressure. For the water transport into and out of the membrane we use a concentration driving force due to the limited availability of the interfacial mass transport barrier.

2.2.3 Heat Transfer

Governing Equations

Applying the energy conservation equation to our fixed, infinitesimal control volume (Bird *et al*, 2007)

$$\rho c_p \frac{dT}{dt} = -(\nabla \cdot \mathbf{q}) \tag{2.31}$$

in which ρ and c_p are the density and specific heat of the membrane-water system respectively. The global heat flux $\mathbf{q}$ assumes contributions from three different sources

$$\mathbf{q} = \mathbf{q}_{\mathrm{c}} + \mathbf{q}_{\mathrm{d}} + \mathbf{q}_{\mathrm{x}} \tag{2.32}$$

The heat flux due to conduction, mass transport, and compositional gradient are considered in Equation 2.32 and are represented by $\mathbf{q}_{\mathrm{c}}$, $\mathbf{q}_{\mathrm{d}}$ and $\mathbf{q}_{\mathrm{x}}$. Newman and Thomas-Alyea (2004), explain that the *Dufour effect*, which is the opposite of the previously explained *Soret effect*, is usually insignificant and is neglected. When the other components are applied to water

$$\begin{aligned} \mathbf{q}_c &= -k\nabla T \\ \mathbf{q}_d &= \overline{H}_0 \mathbf{N}_0 \end{aligned} \tag{2.33}$$

where $\overline{H}_0$ is the enthalpy of water per mole. For the enthalpy of water in the membrane, we used values for saturated liquid water at the same local temperature.

Every time there is water movement in the membrane, it carries with it a small portion of heat. This is quantified by $\mathbf{q}_d$ in Equation 2.33.

Equations 2.31 through 2.33 are the governing equations that describe heat transfer in the three-dimensional multi-physics model.

Boundary Conditions

At the membrane's bare or surface interfaces, there exists an evaporation boundary condition. Since radiation is ignored at the membrane-gas interfaces, there are only two modes of heat loss at the boundary. This boundary condition is expressed in Equation 2.34

$$\mathbf{q} = h(T_s - T_{surr}) + \bar{q}_{st}\mathbf{N}_0 \tag{2.34}$$

where the term expressed by $h(T_s - T_{eq})$ is the convection heat loss, while the term comprised by $\bar{q}_{st}$ is the heat carried away (or gained) when water is lost (or gained) at the membrane-gas interface. $\bar{q}_{st}$ is the water's isosteric heat of sorption or desorption, which describes the heat absorbed or released when water moves across the membrane-gas boundary. T_s is the surface temperature of the membrane while T_{surr} is the surrounding temperature that it is exposed to.

In the pilot-scale coating machine, the drying is accomplished by blowing heated air, so the convection heat-transfer coefficient h is expressed as

$$h = \frac{0.037k_a}{L}\left(\frac{L\mathrm{v}}{v_a}\right)^{\frac{4}{5}}\left(\frac{c_{p,a}\mu_a}{k_a}\right)^{\frac{1}{3}} \tag{2.35}$$

The above expression for h is the correlation for the average convection heat transfer coefficient over an isothermal flat plate in cross flow with a turbulent boundary layer (Incropera and DeWitt, 2007) adapted to suit our membrane.

In Equation 2.35, k_a, $c_{p,a}$, v_a, and μ_a are the thermal conductivity, specific heat, kinematic viscosity, and dynamic viscosity of air, respectively. All these properties are evaluated at the membrane's film temperature. L is the length of the membrane in the direction of air flow and v is the air's free stream velocity.

The heat transfer equivalent of Equation 2.21 is given as

$$\mathbf{q}.\hat{n} = 0 \tag{2.36}$$

and should be used along the planes of symmetry when a small portion of a large membrane is simulated.

Application to Nafion

Thermal Conductivity

The thermal conductivity of hydrated Nafion is the weighted volume fraction average of water and dry Nafion. It can be seen from Equation 2.37 that it is a strong function of water content and a weak function of temperature (Khandelwal and Mench, 2006)

$$\begin{gathered} k = \frac{EWk_m\rho_0 + k_0 M_0 \lambda \rho_m}{EW\rho_0 + M_0\lambda\rho_m} \\ k_m \approx A_m - B_m T \\ k_0 \approx A_0 + B_0 T \end{gathered} \tag{2.37}$$

with $A_m = 448.6{\times}10^{-3}\,\frac{\mathrm{W}}{\mathrm{m{\cdot}K}}$, $B_m = 948.5{\times}10^{-6}\,\frac{\mathrm{W}}{\mathrm{m{\cdot}K^2}}$, $A_0 = 283.4{\times}10^{-3}\,\frac{\mathrm{W}}{\mathrm{m{\cdot}K}}$, and $B_0 = 1.107{\times}10^{-3}\,\frac{\mathrm{W}}{\mathrm{m{\cdot}K^2}}$.

Specific heat

The specific heat of Nafion is not available in literature. As cited before, Nation has a PTFE backbone. We assume the specific heat of Nafion to be the same as its backbone while the water in the membrane has the same specific heat of liquid water (Wu *et al*, 2007).

The effective specific heat in Equation 2.38 is the mass-averaged specific heat for the water-Nafion system

$$c_{p,eff} = \frac{c_{p,0}}{1+\frac{1}{m_0 M_0}} + \frac{c_{p,PTFE}}{1+m_0 M_0} \tag{2.38}$$

in which $c_{p,0}$ and $c_{p,PTFE}$ are the specific heats of water and PTFE.

Heat of Sorption

Water entering and leaving Nafion, releases and absorbs heat. This is equivalent to the release and absorption of heat by condensation and evaporation of a liquid. During absorption of water by Nafion, there is an excess heat of sorption above the heat of condensation of water. This is because the water bound to Nafion does not behave as liquid water. It has been shown that this net heat of sorption is almost zero at high water contents, but is finite and quantifiable at lower concentrations (Burnett *et al*, 2006)(Silverman, 2010). The net isosteric heat of sorption and desorption, $\bar{q}_{st}$, is measured with vapor sorption experiments and is expressed as (Burnett *et al*, 2006)

$$\bar{q}_{st} = \begin{cases} -\bar{h}_{fg} + 28.28\times10^3 \frac{\mathrm{J}}{mol}\left[erf\left(\frac{18.68\lambda M_0}{EW} + 0.4016\right) - 1\right] & (2.39a) \\ \bar{h}_{fg} - 55.65\times10^3 \frac{\mathrm{J}}{mol}\left[erf\left(\frac{10.39\lambda M_0}{EW} + 1.116\right) - 1\right] & (2.39b) \end{cases}$$

where 2.39a is for sorption and 2.39b is for desorption. $\bar{h}_{fg}$ is the temperature-dependent heat of vaporization of water, which is tabulated in Incropera and DeWitt (2007).

In summary, the heat transfer section of the high fidelity model predicts the temperature of the membrane-water system. The modes of heat transfer considered for the internal water movement are convection and advection. At the boundary convection heat transfer is considered in conjunction with the heat lost due to heat of sorption of water that goes across the membrane-gas interface.

2.2.4 Elasticity

Governing Equations

The equation of motion in the fixed Lagrangian reference frame as published in Malvern (1969) is

$$\nabla \cdot \mathbf{T} + \rho \mathbf{b} = \rho \frac{d\mathbf{v}}{dt} \tag{2.40}$$

where $\mathbf{T}$ is the stress tensor and $\mathbf{b}$ is the body force per unit mass. If we choose to ignore the inertial effects and body forces acting on Nafion, Equation 2.40 reduces to

$$\nabla \cdot \mathbf{T} = 0 \tag{2.41}$$

Following the Duhamel-Neumann form of Hooke's law (Malvern, 1969), the constitutive law for the linear elastic solid with thermal stress is given as

$$\mathbf{T} = \mathbf{C}:[-\beta(\theta - \theta_0) + \epsilon] \tag{2.42}$$

where $\mathbf{C}$ is the tensor of elasticity, ϵ is the strain tensor, β is related to the linear coefficient of thermal expansion for the membrane-water system as $\beta = Ka$ and $(\theta - \theta_0)$ is the temperature difference that drives the thermal strain. Silverman (2010) represented this swelling stress by augmenting Equation 2.42 with an additional term due to the presence of water. This "swelling strain" term was made to resemble the thermal stress term

$$\mathbf{T} = \mathbf{C}:[-K\bar{V}_0 m_0 \rho_m - \beta(\theta - \theta_0) + \epsilon] \tag{2.43}$$

in which $\bar{V}_0$ is the partial molar volume of water, ρ_m is the dry density of the membrane and K is the bulk modulus of the membrane.

The stiffness tensor $\mathbf{C}$ is dependent on the elastic modulus and Poisson's ratio. Typically the elastic modulus for a membrane changes with temperature and water content, hence, the stiffness tensor, c, depends on temperature and water content as well. The swelling and thermal expansion constants are assumed to be independent of water content and temperature.

The strain induced due to water is assumed to be equal in all directions.

Boundary Conditions

Since the forces applied during fabrication of the MEA are not considered in the swelling model, all the membrane-gas interfaces are assumed a “free” boundary condition, in which there are no loads or constraints specified at the boundaries. The wrinkling model deals with the stresses encountered by the membrane during manufacturing.

Application to Nafion

Elastic Modulus

As discussed before, the elastic modulus for Nafion was shown to be dependent on temperature and water content (Kusoglu *et al*, 2006). A polynomial data was fit to data published by Tang *et al* (2006)

$$E = 1.739\times10^{3} - 272.7a_0 + 15.63a_0^2 - 7.870T + 345.0\times10^{-3}a_0T + 9.688\times10^{-3}T^2 \tag{2.44}$$

where E is the elastic modulus in MPa.

Poisson’s Ratio and Density

Nafion’s Poisson’s ratio was found to be 0.4 (Huang et al, 2006)(Solasi *et al*, 2007) and its dry density is 1.98 g/cm^3 (DuPont, 2004).

Coefficient of Thermal Expansion

The coefficient of thermal expansion is reported to be 147x10^{-6} K^{-1} (Takamatsu and Eisenberg, 1979). Since the thermal expansion coefficient is very small compared to the swelling effect of water it is neglected. It should be noted that, the glass transition temperature of Nafion is approximately 373 K and the temperature of the membrane-water system should never approach this temperature during the coating-drying process, else Nafion will begin softening.

In summary, the elasticity section of this model tracks the change in dimensions of the Nafion due to water content. We refer to this change as water induced strain. We ignore the temperature-induced expansion because it is several orders of magnitude smaller than the water-induced strain.

2.2.5 Testing the Multi-Physics Model and Simulation Results

Solution method

The water transport, heat transfer and elasticity governing equations were solved using COMSOL, which is a Finite Element simulation package available commercially. The high-fidelity model was solved using a four-core, hyper-threading 2.5 GHz CPU with 16 GB of RAM. Although simulations with some boundary conditions were solved quicker than others, the high-fidelity model took between two and ten hours for completion. It would benefit the entire modeling process if the cost of computation were brought down with a reduced order model.

All the three physics that were simultaneously solved used the same quadrilateral mesh. A backward difference function (BDF) transient solver was used at each time step. This BDF solver implemented a damped Newton nonlinear solved in conjunction with a MUMPS linear solver.

Simulation Results

We obtained desorption data from Surface Measurement Systems, UK for a 2 mm x 2 mm Nafion 115, which has a dry thickness of 127 microns. This data was obtained using a commercially available Dynamic Vapor Sorption Advantage 1 system. Dynamic Vapor Sorption, commonly abbreviated as DVS, is an expensive measurement technique to study and quantify the bulk and surface adsorption of water and other organic vapors. This technique has the capability to record the mass change of the specimen for constantly changing chamber conditions. The chamber has the capability to control the humidity and temperature simultaneously. Although there is slow mixing in the chamber to prevent temperature or humidity gradients, for calculation purposes it is considered quiescent.

Desorption tests

The high-fidelity swelling model was simulated by imposing boundary conditions very similar to the actual tests. A three-dimensional illustration is shown in figure 2.3 to illustrate the boundary conditions used.

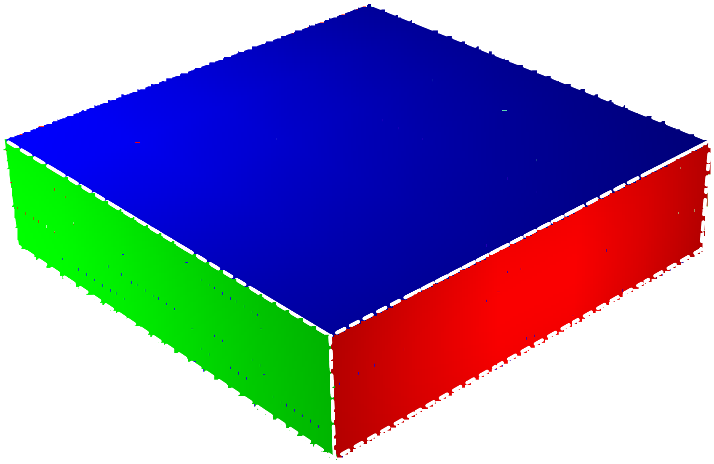

Figure 2.3: An out of scale rendering of membrane to illustrate the boundary conditions

In the DVS test machine, our piece of Nafion was constantly weighed on a microbalance that has an insulated weighting surface. Because the bottom of the membrane is in direct contact with the balance, we expect no heat and mass transfer from the bottom face. In our simulation, mass and heat transfer was permitted on five faces of

Nafion, except the bottom face (directly opposite the blue face, not shown in figure). It should be noted that a "free" boundary condition was imposed on all the faces for the solid mechanics module of the simulation.

Figure 2.4 shows the humidity profile of the chamber with respect to time. Relative humidity (RH) is expressed between 0 and 100% while water activity is expressed between 0 and 1. The scaling between them is linear. This particular test was performed at a constant temperature of 303 K.

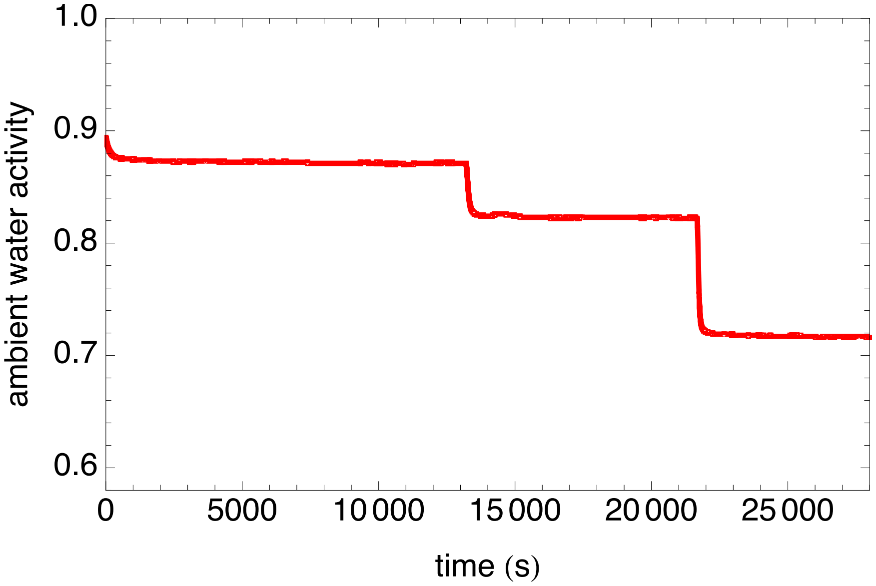

Figure 2.4: Ambient water activity vs. time in DVS desorption experiment

Plot shown in figure 2.5 shows the mass change of the membrane normalized by the final change in mass for the actual and simulated experiment. The data is normalized so that the change is easily visualized and it is easier to compare the results.

Figure 2.6 shows the simulated temperature at the membrane's mid-point; the chamber's temperature during the actual experiment was set at 303 K and variations were within 0.1 % of the absolute value.

It can be seen that the simulated results agree well with the actual experiment. It should also be noted that the discussed results are one among a several desorption experiments performed on a DVS-1000 system by Surface Measurement Systems, Alperton, UK. When data from the experiments were compared with the results obtained from the simulation, the resulting error was always within 2%.

We were unable to test the model with any absorption data due to its unavailability.

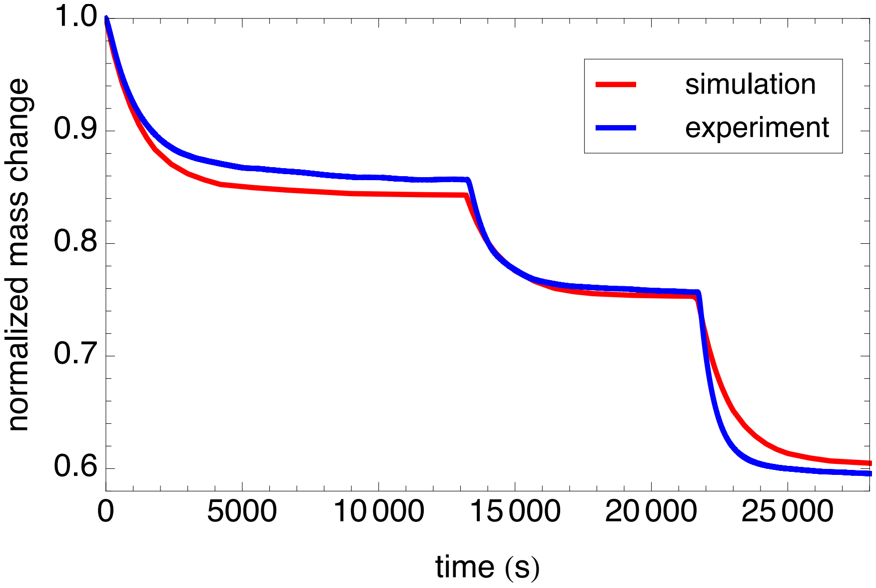

Figure 2.5: Normalized mass change for actual and high-fidelity model simulated experiment

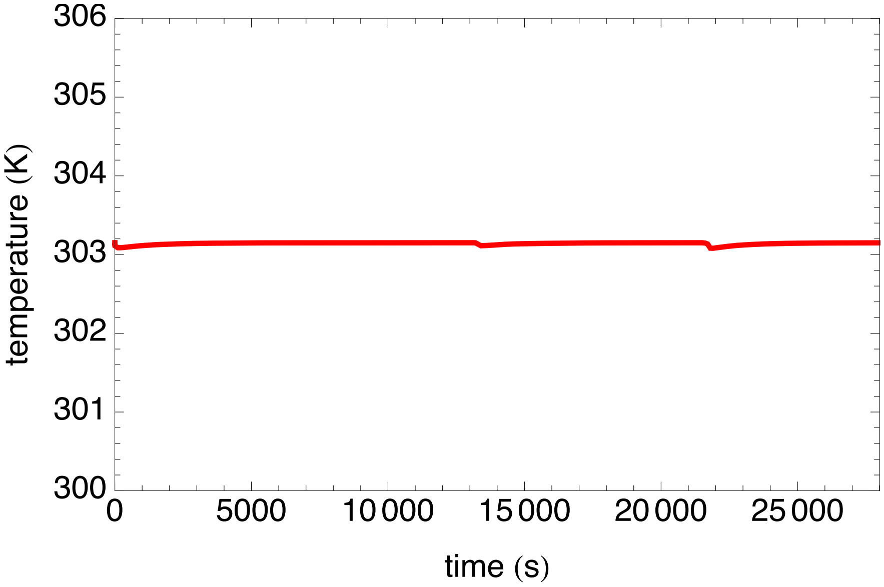

Figure 2.6: Simulated mid-point temperature during model testing

Since our simulations were three-dimensional, we have the temperature, water content and strain distributions for all points in our mesh. We are attaching some two-dimensional plots showing the distribution of the said quantities at various instances in time.

Figures 2.7 and 2.8 show water content λ for a two-dimensional slice through the mid-point at times t=300 and t=20005 seconds after the start of the simulation. It should be noted that although the colors shown in the figures indicate a dramatic gradient, the gradient is almost negligible. This is visible from the scale on the right side of the figure. We noticed no appreciable water content gradients in the Nafion at any instance in our simulations.

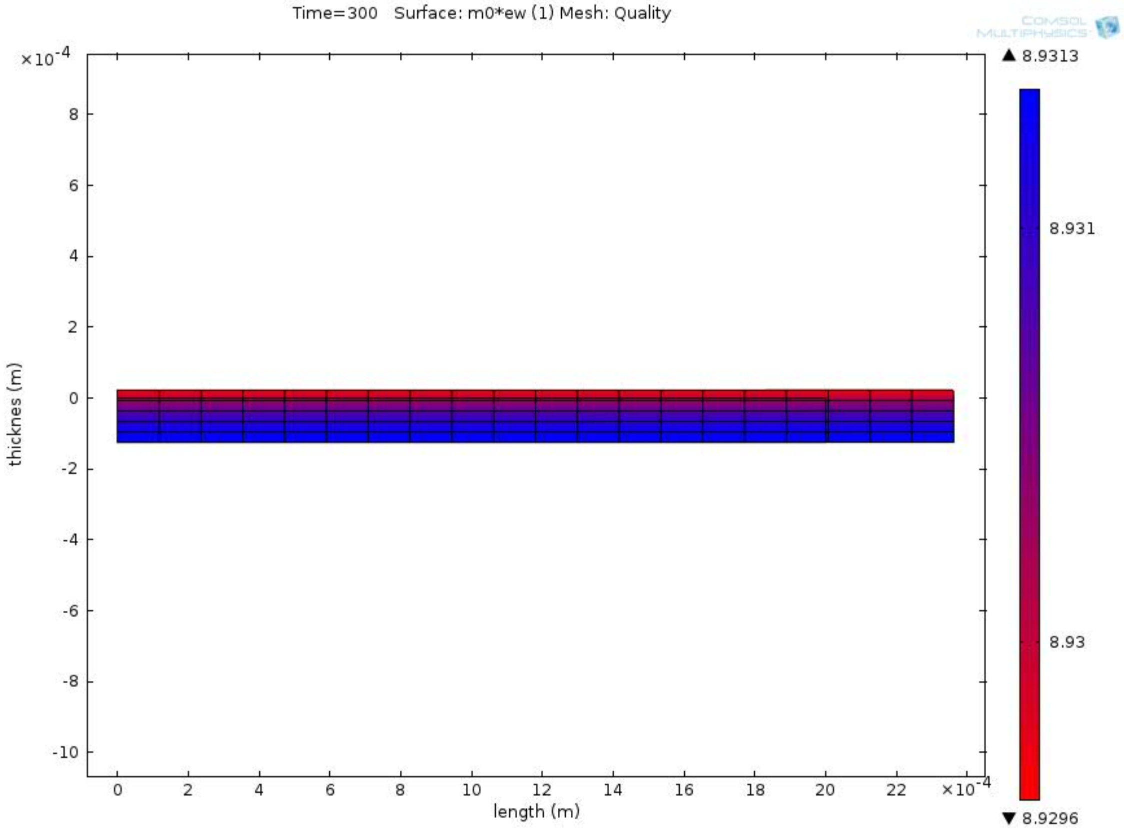

Figure 2.7: Water content profile λ of middle slice at t=300 for simulation

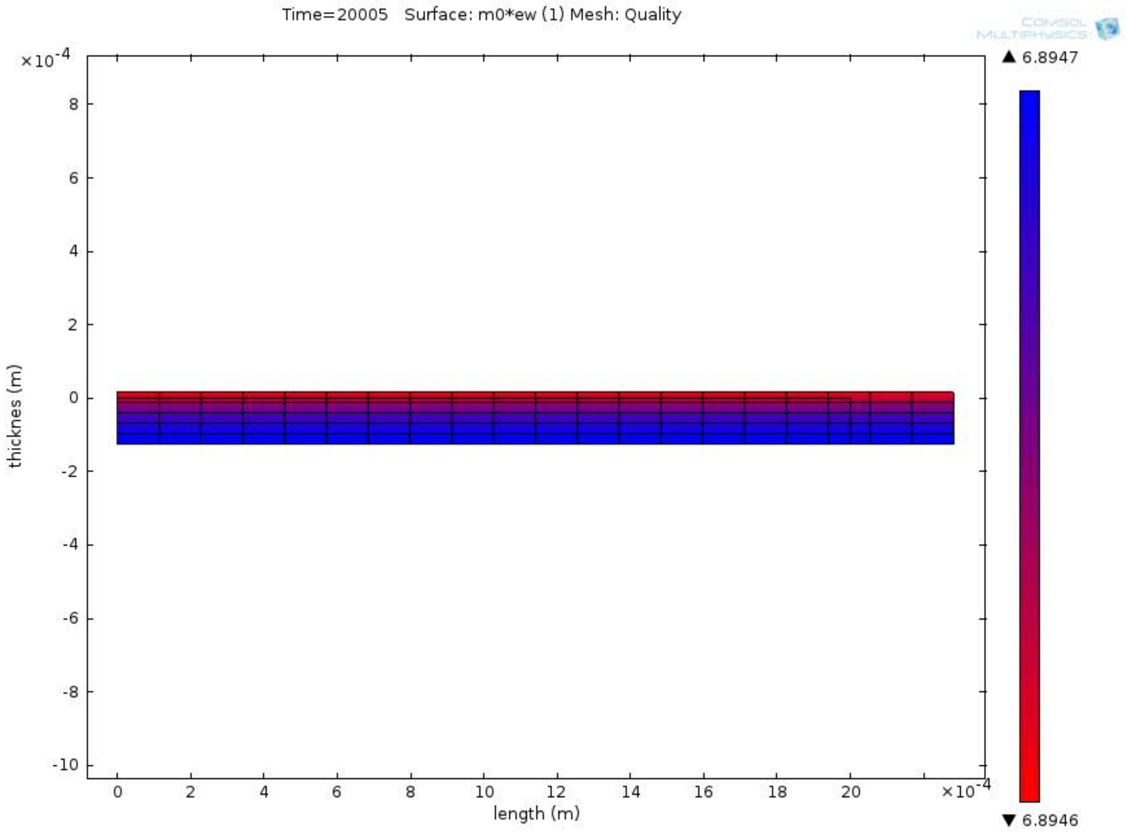

Figure 2.8: Water content profile λ of middle slice at time t=20005 s for simulation

Similarly, figure 2.9 show the temperature profile at identical contexts. There exists a uniform temperature throughout the entire simulated Nafion piece. The strong variation in color is after the third decimal place, and is because of the round-off artifacts that occur in simulation.

It should be noted that these uniform distributions of the said quantities, occur because of the uniform boundary conditions. In other words, if the Nafion is dried non-uniformly, we may notice gradients. There is no accurate way to experimentally test this, but we will aim at uniformly drying and wetting the membrane in our manufacturing process.

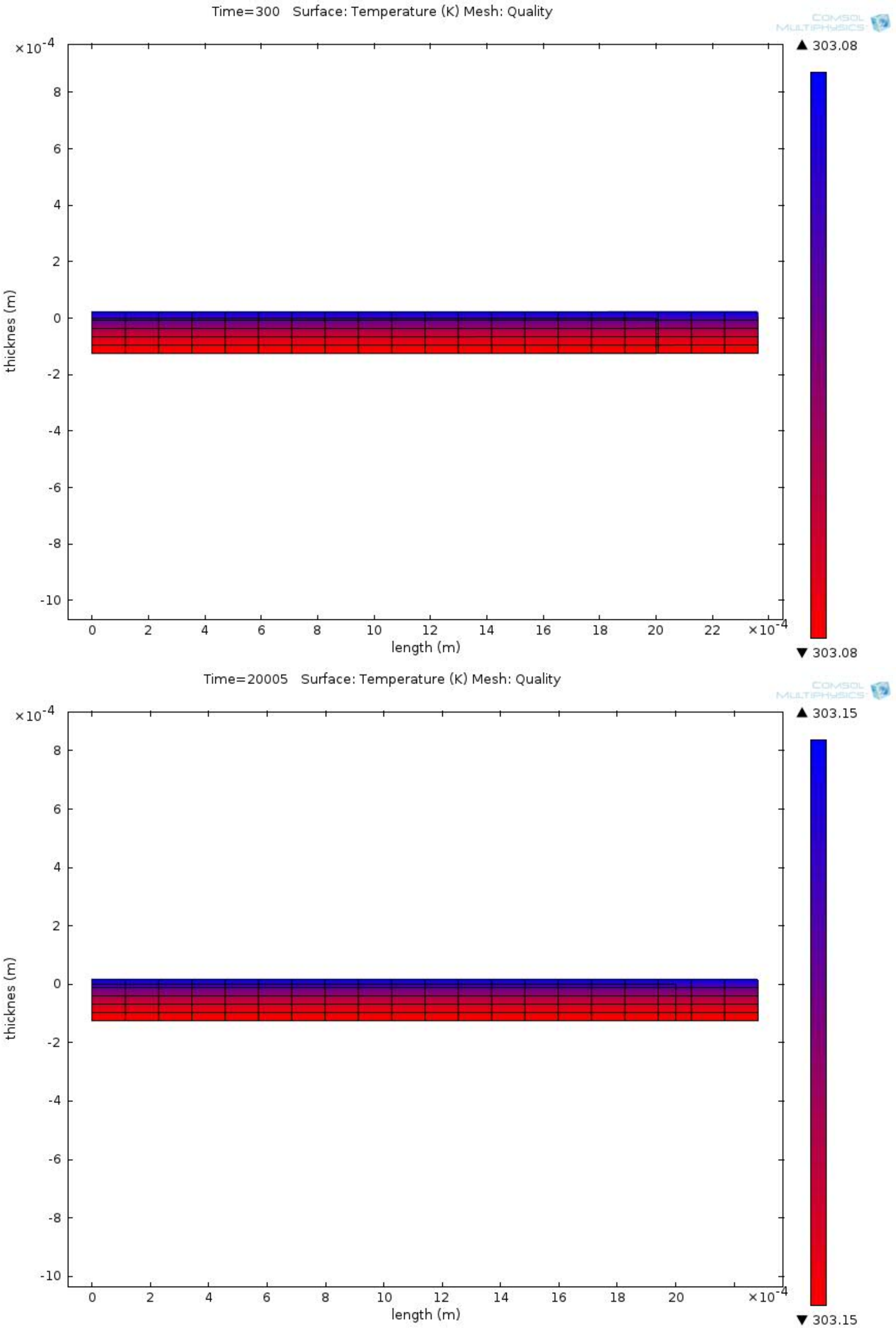

Figure 2.9: Temperature profiles of middle slice at times t=300 s and t=20005 s for the high-fidelity model's simulation

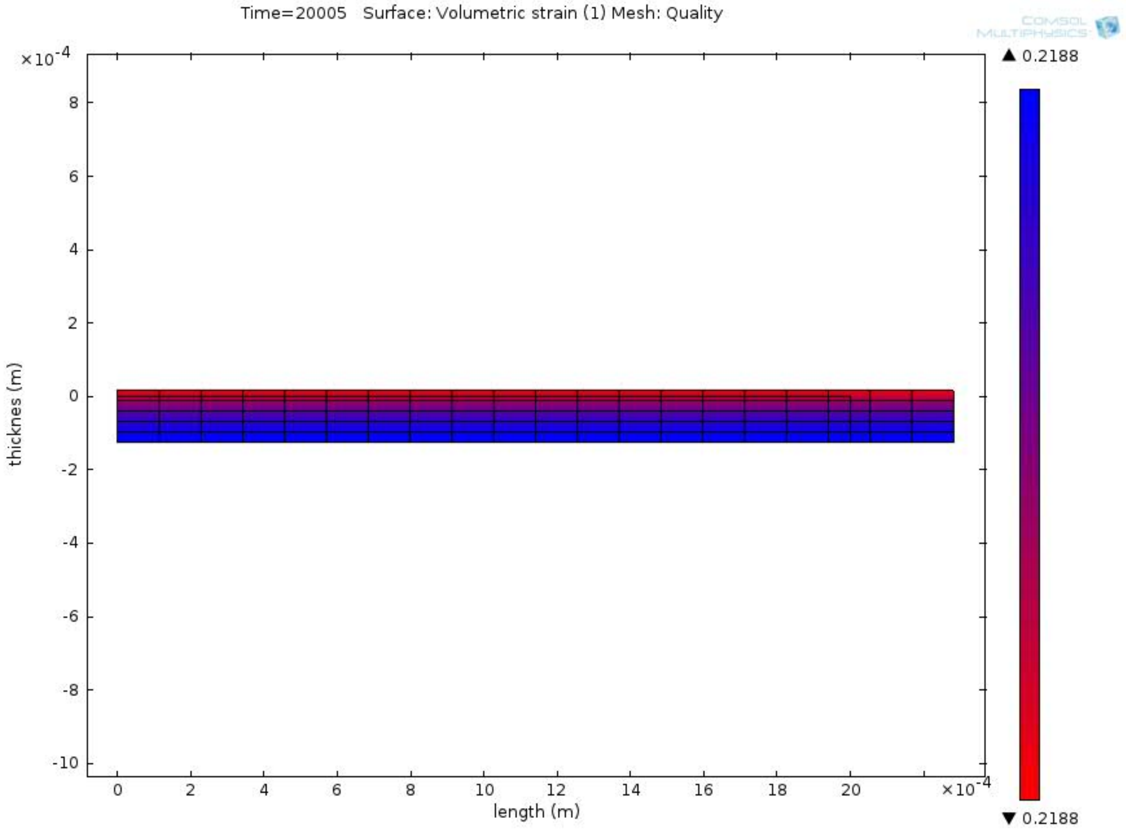

Figure 2.10: Volumetric strain distribution at time t=20005 s

Figure 2.10 shows the overall volumetric strain for the midpoint slice at t=20005 s, and we can see no appreciable gradient. This is an expected result, as in this high-fidelity model the stresses and strains are dependent on the water content. We have good agreement between the solid mechanics and the mass transfer part of the model.

Highlights from high-fidelity model

The high fidelity model was tested with actual desorption experiments carried out with a commercial DVS system. The results predicted by the model are in agreement with the actual experiments lasting over seven hours. By studying the simulated results, it was established that the water content, temperature and strains were constant in all the directions, and there were no appreciable gradients in these quantities. It may be safely concluded that these quantities will not exhibit any appreciable variation if the membrane is uniformly dried or humidified.

2.3 REDUCED ORDER SWELLING MODEL

2.3.1 Need for a Reduced Order Model

The high-fidelity model consists of three major governing equations that are coupled with each other. Solving these equations with the current computational resources available is computationally expensive and more importantly time consuming. It is not feasible to solve such a model in real time and the structure of the model is not optimal to implement model-based control, which is a further goal of this research.

It was established in Section 2.2.5 that for uniform boundary conditions, there are no variations in the temperature and water content along the length and width. The variation through the thickness is also negligible.

The design of an MEA fabrication process and implementation of control can benefit from a faster model, provided the boundary conditions during drying are similar to the ones tested. In other words, if we ignore the variations along the length, width, and thickness, the model can be greatly simplified without loss in accuracy in order to efficiently predict properties during uniform drying.

In the case of our high-fidelity model, we put together three separate physics in a three-dimensional mesh and solved it in terms of time. Although, all our governing equations and assumptions are justified, not all of them may have a large impact on the final result. In this section, we aim to see if we can identify and omit some effects that may improve computational performance and thus allow the usage in a real time control strategy without any significant loss of accuracy.

2.3.2 Model Reduction and Comparison to the High-Fidelity Model

The high-fidelity model developed above is both highly non-linear and coupled. Table 2.1 shows the various non-linear governing equations and the interdependent terms. We attempted computational cost reduction by decoupling some of the equations and by omitting some interdependent terms, then comparing the resulting solution to the high-fidelity model.

Table 2.1: Governing equations, solved and coupled quantities

Physics	Governing equations	Solved quantity	Coupled quantity
Mass transfer	Equations 2.5 & 2.19	m_0 (water content)	p (from solid mechanics) ε_v (from solid mechanics) T (from heat transfer)
Heat transfer	Equations 2.31 & 2.33	T (temperature)	m_0 (from mass transfer)
Solid mechanics	Equation 2.43	ϵ (strain)	m_0 (from mass transfer) T (from heat transfer)

Omitting the effect of pressure gradient from mass transfer

The gradient of pressure, ∇p, is one of the driving forces for internal water movement in Equation 2.19. The gradient of pressure is related to the gradient of strain, and since we did not see any appreciable variation in the strain distribution from the high fidelity model, the internal water movement due to ∇p must be small. This fact is confirmed by comparing the water profiles with and without ∇p at various times. Figure 2.11 shows the before and after distributions through the thickness at t=20,005 s and it can be seen that the difference that exists is after the third decimal place and can be neglected.

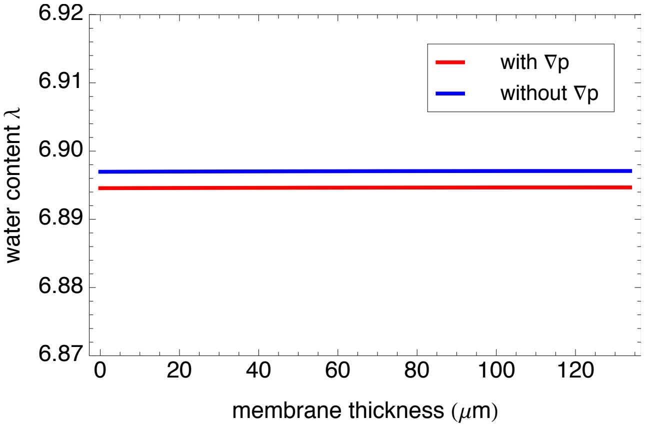

Figure 2.11: Water content through the thickness with and without contribution from ∇p in internal water flux $\boldsymbol{N_0}$ at t=20,005 s

Figure 2.12 shows the water profile through the thickness for the high-fidelity model. It should be noted that the parabolic shape was preserved in the result obtained without the pressure driving force ∇p. It is not explicitly seen in figure 2.11 because of the y-axis scale. Although the profile is parabolic, the variation is largely negligible.

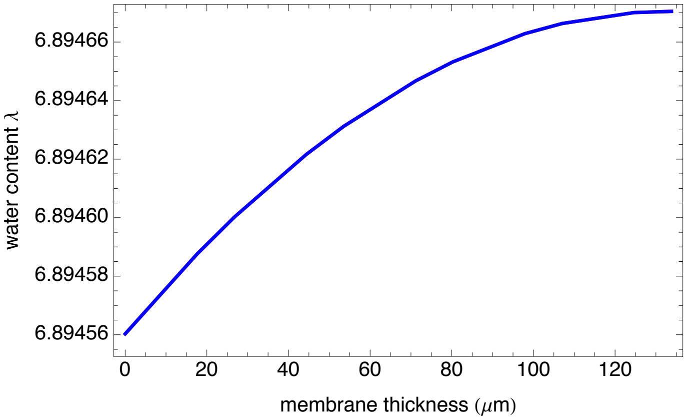

Figure 2.12: Water content through the thickness for the high-fidelity model highlighting the parabolic profile at t=20,005 s

Replacing volumetric strain with calculated water strain

Mass transfer Equations 2.5 and 2.19, are still coupled to the solid mechanics equations because they contain the volumetric strain term ε_v. It was assumed in this model that the volumetric strain is only due to water (Silverman, 2010), and this can be calculated and expressed as

$$\varepsilon_v = \frac{m_0 M_0 \rho_m}{\rho_0} \tag{2.45}$$

where M_0 is the molar mass of water, ρ_m and ρ_0 are the densities of the membrane and water, respectively.

Figure 2.13, shows the comparison between the multi-physics model and the model in which ∇p is omitted and ε_v is replaced by Equation 2.45. This reduced model has the solid mechanics equations completely decoupled from the mass transfer governing equations. Since the solid mechanics equations play no role in the water transfer and heat transfer, and the strains are uniform throughout the membrane, it can be completely omitted from the reduced order model. We will calculate the strains during the production process in the wrinkling model, which is defined in Chapter 4.

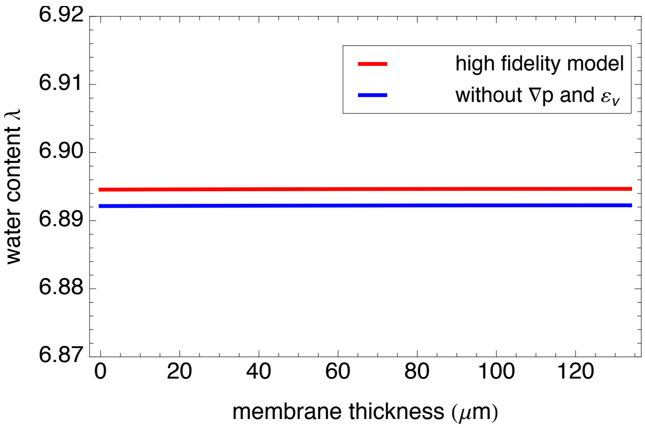

Figure 2.13: Comparison between high fidelity model and solid mechanics decoupled model at t=20,005 s.

Model reduction: from three-dimensional to a zero-dimensional model

The above-mentioned solid mechanics decoupled model is still a three-dimensional model. Condensing it to a lumped model can further reduce the computational overhead. This can be justified, since the temperature and water content do not vary along the length and width directions. Moreover, our previous simulations have shown very little variation through the thickness as well and thus that can be neglected. The derivation of the reduced-order model is shown in section 2.3.3.

The reduced-order model is then obtained by assuming that the water content and temperature within the control volume are uniform in space. This is consistent with what we noted in the results of the high-fidelity model. The computational overhead dramatically decreases and we observe that the simulated results obtained from the reduced order model (lumped model) continue to match the experimental data obtained from Surface Measurement Systems, UK.

Figure 2.14 shows the performance of the reduced order model alongside the high-fidelity model and experimental data.

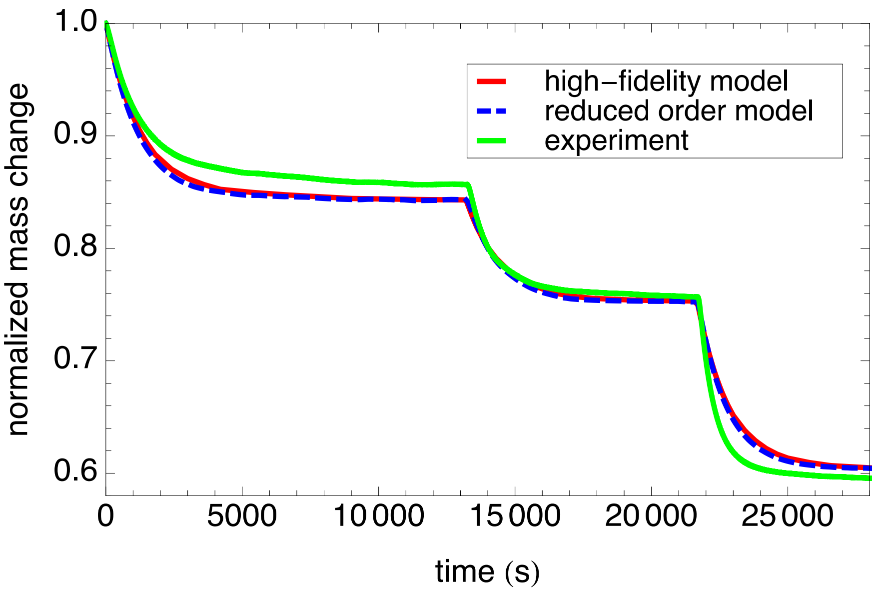

Figure 2.14: Comparison between experimental, high-fidelity model and reduced order model results at t=20,005 s

As mentioned in Section 2.2.5, the high-fidelity model took between two and ten hours for completion. The reduced order model is solved in under a second with the same computing resources and we can see from Figure 2.14 that the results from the two models are almost identical.

The reduced order model is computationally inexpensive when compared to the high-fidelity model and can be solved in real time allowing us to use the reduced order model to implement a real time control strategy for controlling uniform drying.

2.3.3 Consolidated Reduced Order Swelling Model Equations

In the previous section, the performance of the reduced order lumped model consisting of mass and heat transfer was discussed. In this section we derive the lumped model from the high-fidelity model.

Water Transport

Substituting Equation 2.45 into 2.5, and rewriting the governing equations for water transport

$$\frac{{\rho_0}^2\rho_m}{(\rho_0+M_0\rho_m m_0)^2}\frac{\partial m_0}{\partial t}+\nabla\cdot\boldsymbol{N}_0=0\ in\ \Omega \tag{2.46}$$

where in the membrane domain shown in Figure 2.3, the volume is represented by Ω and the boundary surfaces by $d\Omega$. For desorption, the boundary conditions are given by

$$\boldsymbol{N_0}.\hat{n}=\alpha_c\left(c_{0,s}-c_{0,eq}\right)\ on\ \Gamma\subset d\Omega \tag{2.47}$$

Integrating Equation 2.46 over Ω, we get

$$\int\limits_{\Omega}\frac{{\rho_0}^2\rho_m}{(\rho_0+M_0\rho_m m_0)^2}\frac{\partial m_0}{\partial t}dV+\int\limits_{\Omega}\nabla\cdot\boldsymbol{N}_0dxdydz=0 \tag{2.48}$$

Where $dV=dxdydz$ refers to a volume element and x,y and z represent the three directions. Applying Green’s theorem (Strang and Fix, 2008) to the second term

$$\int\limits_{\Omega}\frac{{\rho_0}^2\rho_m}{(\rho_0+M_0\rho_m m_0)^2}\frac{\partial m_0}{\partial t}dV+\int\limits_{d\Omega}\boldsymbol{N_0}.\hat{n}\,dS=0 \tag{2.49}$$

where dS represents an appropriate surface element. Substituting flux from Equation 2.47 and since $\boldsymbol{N_0}$ is assumed as zero on $d\Omega\setminus\Gamma$, then

$$\int\limits_{\Omega}\frac{{\rho_0}^2\rho_m}{(\rho_0+M_0\rho_m m_0)^2}\frac{\partial m_0}{\partial t}dV+\int\limits_{\Gamma}\alpha_c\left(c_{0,s}-c_{0,eq}\right)dS=0 \tag{2.50}$$

which reduces to

$$\frac{{\rho_0}^2\rho_m}{(\rho_0+M_0\rho_m m_0)^2}\frac{d}{dt}\int\limits_{\Omega}m_0\,dV+\alpha_c\left(c_{0,s}-c_{0,eq}\right)\int\limits_{\Gamma}dS=0 \tag{2.51}$$

when integration is performed, Equation 2.51 reduces to

$$\frac{{\rho_0}^2\rho_m}{(\rho_0+M_0\rho_m m_0)^2}\frac{dm_0}{dt}\boldsymbol{V}+\alpha_c\left(c_{0,s}-c_{0,eq}\right)\boldsymbol{A}=0 \tag{2.52}$$

where $\boldsymbol{V}$ is the volume of the domain and $\boldsymbol{A}$ is the surface area in Γ over which drying is considered. For the boundary conditions at which the multi-physics model was solved

$$\boldsymbol{A}=2lt+2wt+lw \tag{2.53}$$

where l, w, and t represent membrane's length, width and thickness, respectively. Equation 2.52 can be simplified to

$$\frac{{\rho_0}^2 \rho_m}{(\rho_0 + M_0 \rho_m m_0)^2} \frac{dm_0}{dt} = -\frac{\boldsymbol{A}}{\boldsymbol{V}} \alpha_c \left(c_0 - c_{0,eq}\right) \tag{2.54}$$

where c_0 is calculated from m_0. The absence of $c_{0,s}$ in Euqation 2.54 is a consequence of the lumped approximation.

Heat Transfer

Similar to the method used to derive the new equation for water transport, the heat transfer governing equation can be expressed as

$$\rho c_p \frac{dT}{dt} = -\frac{\boldsymbol{A}}{\boldsymbol{V}} \left[h(T - T_{surr}) + \bar{q}_{st} \alpha_c \left(c_0 - c_{0,eq}\right)\right] \tag{2.55}$$

The fraction $\boldsymbol{A}/\boldsymbol{V}$ can be approximated for extremely large and thin domains. This will be explained in Chapter 3.

2.3.4 Justification of the Lumped Model

The use of the lumped model to explain water and heat transfer in Nafion can be justified by looking at the mass transfer and heat transfer Biot numbers. If this number is small compared to 0.1, then the lumped assumption is justified (Incropera and DeWitt, 2007)(Mills, 2001).

The mass transfer Biot number, Bi_m, applied to our membrane system can be defined as

$$Bi_m = \frac{\alpha_c * t}{\mathcal{D}_{0m}} \tag{2.56}$$

And its heat transfer analogue, Bi_h, is expressed as

$$Bi_h = \frac{h * t}{k} \tag{2.57}$$

Parameters $\alpha_c, h, \mathcal{D}_{0m}$, and k have been defined in the preceding sections and our calculated Bi_m and Bi_h satisfy the conditions specified in Mills (2001).

2.4 CONCLUSION

We developed a three-dimensional, transient high-fidelity model that included mass transfer, heat transfer and elasticity. This model describes the behavior of a PEM during absorption and desorption. This model, when applied to Nafion, although computationally expensive, matched well with data obtained from experiments.

When the boundary conditions were uniform, we noticed no variation in the solution along the length and width, and minimal variation through the thickness. This prompted us to revisit the governing equations and develop a reduced-order lumped model that performed as well as the high-fidelity model at a fraction of the computational cost. We would be using this model along with the coating model explained in Chapter 3 to implement control in MEA fabrication.

Chapter 3: Modeling of the Coating Process

3.1 INTRODUCTION

3.1.1 Background

In Chapter 2, we developed a model that described the absorption and desorption of the PEM. During the actual fabrication of an MEA, following the hydration of PEM, a liquid ink is deposited on the saturated membrane and the combination of the two is further dried. In order to better understand this drying process, and as a step to implementing improved control of the MEA manufacturing process, we develop a model in this chapter that describes the drying behavior of the coating. We then combine this newly developed coating drying model with the hydration model developed for the PEM in the preceding chapter, to allow us to predict the behavior of the these components when they interact during the drying step involved in fabrication of direct methanol fuel cells.

During fabrication of MEA, the PEM is coated with a catalyst ink which typically contains water, alcohol, an ionomer, and a catalyst which is dispersed on a carbon black carrier. The water and alcohol evaporates during drying leaving behind a porous structure that consists of the ionomer and the catalyst coated carbon black. The catalyst is coated on carbon black to allow maximum active surface area for a given mass of catalyst (Higuchi *et al*., 2005).

The relative proportion of the ink constituents can be varied to suit the coating technique and to achieve different catalyst loading on the MEA. For example, the Doctor Blade method of ink application requires a formulation that results in a higher viscosity ink in order to evenly spread the ink across the membrane, while application methods that utilize spraying requires formulations that results in a less viscous ink again to achieve even distribution of the ink across the membrane (Koraishy, 2010). In this chapter we attempt to develop a generalized coating model that will work for all water based ink formulations and still allow for future modifications based on variations in the proposed formulations.

3.1.2 Method of Approach

We start by developing a lumped model that describes and quantifies water lost by the coating while drying. The boundary conditions defined in this model are similar to conditions used when modeling the drying of the PEM in preceding chapter. We then implement this model for one specific water-based ink recipe or formulation that is discussed in Section 3.2. It should be noted that we apply ink in our pilot-scale membrane coating machine using a doctor blade, this method is also commonly referred to as tape casting.

After developing the generalized model, we then apply specific values for our specific formulation and application method, the model is then simulated and compared with experimental data to verify its accuracy. Finally, we combine the coating and the membrane models together and define interfacial boundary conditions that define water movement from the coating to the membrane. This combined membrane/coating dry model will later be used in formulation of a new manufacturing control strategy.

3.2 THE CATALYST INK

As mentioned above, a typical fuel cell ink formulation consists of water, a solvent, an ionomer, and a catalyst-coated carbon black. As measured by volume, water is by far the largest constituent of the mixture and acts as the carrier medium for the components of the ink. A small amount of a solvent, typically methanol or isopropyl alcohol, is used to reduce the surface tension of water and to promote better distribution of the solid particles. The purpose of adding an ionomer to the ink is to ensure adhesion to the ionomer based PEM membrane as well as to make the catalyst layer itself flexible. The catalyst-coated carbon black contains the actual catalyst that initiates the fuel cell reactions.

It is also common for fuel cell catalyst inks to contain some small quantities of a surfactant to better disperse the particulate matter, especially in higher solid content inks (Prabhuram, 2003). Common surfactants include polyvinylpyrrolidone (PVP), polyvinylsulfonate (PVS), sodium lauryl sulfate (SLS), and tetraoctylammonium bromide (TOAB). The ink blends that we tested had relatively lower solid content, about 5%, and hence we did not use a formulation that contains any surfactants.

Although the typical fuel cell ink contains a catalyst in it, the blends that we used did not contain the actual catalyst. Instead we substituted the catalyst-coated carbon black with plain carbon black. We used XC-72R, a dispersion grade carbon black manufactured by Cabot Corporation. XC-72R is widely used in fuel cell ink applications (Huang *et al*., 2011). Since the aim of our work was to develop a controlled continuous coating process for Nafion and since the accuracy of the modeling and controlling could be verified from the quality of the coated Nafion membrane and not the actual fuel cell performance, it therefore was not justified to use expensive catalyst materials to formulate the ink and hence the substitution of XC-72R was made.

It should be noted that the model that we developed can also be implemented for fuel cell inks that contains catalyst by simply recalculating input constants like ink density, viscosity, etc.

3.2.1 Ink composition

The actual composition or formulation of the ink that we used is listed below in Table 3.1. This ink formulation is adapted from Park *et al*. (2010) with minimal variation. The table lists the quantities needed to make a batch of ink.

Table 3.1: Composition of the ink used

Component	Quantity
Water HPLC grade	4 ml
10 wt% Nafion solution (ionomer dispersed in water)	6 ml
Iso-propanol	0.6 ml
XC-72R carbon black	0.53 grams

The components mentioned above can be proportionally increased to make a larger quantity of ink.

3.2.2 Mixing Technique

We followed the ink mixing technique described by Xie *et al*. (2008). It involves repeated mechanical stirring and sonication, which is a method of agitating particles in solution using ultrasonic energy. We stirred using a magnet and a stir plate and our sonication was done using a Branson 6510 sonicating bath. Sonication was done in a closed vial at room temperature to prevent the alcohol from evaporating. Ink prepared by the above method was later coated in our pilot-scale coating machine, and those results are discussed later in Chapter 6.

3.3 REDUCED ORDER COATING MODEL

3.3.1 Assumptions

The zero-dimensional coating drying model was developed assuming that the coating is applied uniformly and is itself homogenous. As water dries from the applied coating, the volume change due to the water lost needs to be considered. We are thus able to model the water loss in the coating in a way similar to the one where water loss in the membrane was modeled. It should be noted that as this water is lost, it results in a thickness reduction of the coating and this reduced thickness is then used to determine the state of the coating in additional calculations detailed later in Chapter 6.

Again, this model, like the hydration model for the membrane, ignores the effect of any applied stresses, which are considered later. The coating can be considered elastic because of the presence of an ionomer, and can be assumed to expand and contract with the underlying membrane without failing, ripping, or tearing (Mehta, 2002).

We start by applying the lumped mass transfer and heat transfer governing equations, as developed in Chapter 2, to the coating. We are thus able to track the water content, expressed as molality, m_{0c}, and the temperature, defined as T_c, of the coating. It is important to note that subscript c refers to the coating.

Although some ionomer is present in the coating, that will absorb and hold water as analyzed in Chapter 2, and because of its low relative concentration compared to the other components, we choose to ignore it. It is also assumed that all the water in the coating is homogenously distributed and has the same tendency to move out of the coating.

Additionally, since the coating has such high water content, it is assumed that the membrane remains fully hydrated until all liquid water from the coating is lost. In other words, when the coating is applied on a piece of membrane, the coating has sufficient water to transfer to the membrane, replacing the other water lost elsewhere from the membrane allowing the membrane to remain fully saturated as long as the coating has water remaining (Silverman, 2010). The coating acts like a reservoir of water that can move into the membrane or evaporate into the surrounding air. This assumption is implemented in the boundary conditions when the swelling and coating models are combined allowing us to piecewise consider, first the drying of the coating, with the membrane remaining saturated, and then consider the drying of the membrane itself.

3.3.2 Water Transport

Governing Equations and Boundary Conditions

Since our coating is about ninety-five percent water by volume, the volume changes resulting from evaporation are significant and need to be addressed. Similar to our development in Section 2.2.2, we use the molality of the water in the coating to track the water content. Molality, m_{0c}, is the ratio of moles of water in the coating to grams of dried coating. It should be noted that when m_{0c} goes to zero, the coating is completely dry of liquid water.

We can derive a lumped water transport governing equation for m_{0c} in a manner very similar to Section 2.3.3

$$\frac{{\rho_0}^2 \rho_s}{(\rho_0 + M_0 \rho_s m_{0c})^2} \frac{dm_{0c}}{dt} = -\frac{\boldsymbol{A_c}}{\boldsymbol{V_c}} \alpha_{coat} \left(c_{0c} - c_{0c,surr} \right) \tag{3.1}$$

where ρ_s is the density of the dry coating, $\boldsymbol{A_c}$ is the area over which the drying is considered, and $\boldsymbol{V_c}$ is the volume of the coating. Parameter α_{coat} is the mass transfer coefficient for the coating and $c_{0c,surr}$ is the surroundings liquid water concentration. It should be noted that Equation 3.1 considers a concentration driving force similar to Equation 2.29. Parameter $c_{0c,surr}$ was set to zero in our simulations because we assume the water content in the surrounding air is always negligible compared to the amount of water present in the coating.

During the development of Equation 3.1, we do not consider the water transferred from the coating to the membrane, and this is studied when we combine the coating and swelling models in Section 3.4.

Because we consider the concentration a driving force, the water concentration of the coating c_{0c} is to be defined and it is expressed as

$$c_{0c} = \frac{m_{0c}\rho_0\rho_s}{\rho_0 + M_0 m_{0c}\rho_s} \tag{3.2}$$

which is obtained by combining equations in an analogous manner to how we combined Equations 2.2 and 2.3 in the preceding chapter.

Application to the Ink Mixture

Dry density of the coating

The density of the dry coating is calculated by

$$\rho_s = \frac{\sum mass\ of\ solids}{\sum volume\ of\ solids} \tag{3.3}$$

where in our ink formulation, the solids refer to the carbon black and nafion.

Mass transfer coefficient for the coating

The mass transfer coefficient α_{coat} is assumed to be dependent on temperature and Reynolds number of the moving air that is used for drying the coating. It is obtained from convection mass transfer correlations (Incropera and DeWitt, 2007)(Mills, 2001). For a cross flow with a turbulent boundary layer, the mass transfer coefficient α_{coat} can be modeled as

$$\alpha_{coat} = \frac{0.037\mathcal{D}_{0,air}}{L_c}\left(\frac{L_c \mathrm{V}}{\nu_a}\right)^{\frac{4}{5}}\left(\frac{\nu_a}{\mathcal{D}_{0,air}}\right)^{\frac{1}{3}} \tag{3.4}$$

where $\mathcal{D}_{0,air}$ and v_a, respectively, refer to the diffusion coefficient of water in air and kinematic viscosity of air. All these properties are evaluated at the coating's temperature. L_c is the length of the coating in the direction of air flow, and v is the air's free stream velocity. It should be noted that when the coating drying model and the membrane hydration/swelling model are used in together, L and L_c would be equal because we are assuming the coating process to apply ink on the entire surface of the membrane.

Equations 2.35 and 3.4 assumes that at the edge of the Nafion membrane or the coating, the boundary layer is "tripped" and thus causes a turbulent condition over the entire membrane or coating. This assumption is reasonable based on the fact that it is very difficult to perfectly align the flow to be perpendicular to the membrane or coating.

3.3.3 Heat Transfer

Governing Equations and Boundary Conditions

Convection and advection are the two modes of heat transfer modeled in the governing heat transfer equations. The coating's temperature is referred to as T_c, and the lumped differential equation used for simulation is

$$\rho_{coat} c_{p,coat} \frac{dT_c}{dt} = -\frac{\boldsymbol{A_c}}{\boldsymbol{V_c}} \left[h_{coat}(T_c - T_{surr}) + \bar{h}_{fg} \alpha_{coat} \left(c_{0c} - c_{0c,surr} \right) \right] \tag{3.5}$$

where ρ_{coat} and $c_{p,coat}$ refer to the effective density and specific heat of the coating, respectively. It should be noted that ρ_{coat} and $c_{p,coat}$ depend on the water content of the coating. h_{coat} refers to the convection heat transfer coefficient for the coating, T_{surr} is the temperature of the surroundings and $\bar{h}_{fg}$ refers to the heat of vaporization of water which is tabulated in Incropera and DeWitt (2007).

Application to the Ink Mixture

Effective density of the coating

Determining the effective density of the coating requires considering the masses and volumes of the dry coating as well as the water present in the coating, and is expressed as

$$\rho_{coat} = \frac{\rho_0(\rho_s + M_0 m_{0c}\rho_s)}{\rho_0 + M_0 m_{0c}\rho_s} \tag{3.6}$$

The above equation was obtained by dividing the total mass of the individual constituents of the ink mixture by its total volume. Since this density calculation takes into account the water content of the coating, it is dependent on m_{0c}. When the coating is completely dry, $\rho_{coat} = \rho_s$ because .

Effective specific heat of the coating

The effective specific heat of the coating can be computed with the general equation

$$c_{p,coat} = \frac{\sum_i mass_i \, c_{p,i}}{\sum_i mass_i} \tag{3.7}$$

where index i cycles through all the individual constituents present in the coating.

Convection heat transfer coefficient

The convection heat transfer coefficient can be calculated from

$$h_{coat} = \frac{0.037 k_a}{L_c}\left(\frac{L_c \mathrm{V}}{v_a}\right)^{\frac{4}{5}}\left(\frac{c_{p,a}\mu_a}{k_a}\right)^{\frac{1}{3}} \tag{3.8}$$

This equation is similar to Equation 2.35 and is a correlation adapted from Incropera and Dewitt (2007).

3.3.4 Justification of Lumped Model

As explained in Section 2.3.4, the mass transfer and heat transfer Biot numbers can be used to justify the lumped assumption (Mills, 2001). The mass transfer Biot number for the coating is expressed as

$$Bi_m = \frac{\alpha_{coat} * coating\ thickness}{\mathcal{D}_{0,coat}} \tag{3.9}$$

In Equation 3.9, $\mathcal{D}_{0,coat}$ is the diffusion coefficient of water in the coating. This number tends to infinity when the coating is fully wet due to its low viscosity, and gradually drops as water content decreases. Because of this, Bi_m will be extremely small when computed for the wet coating. Since the dependence of $\mathcal{D}_{0,coat}$ as a function of water content is not quantified in literature, we assume that the usage of the lumped model is justified throughout the entire drying process of the coating.

The heat transfer Biot number when calculated for the coating is very small when compared to 0.1 and can readily justify the usage of the lumped assumption to describe heat transfer.

3.3.5 Simulation

Equations 3.5 and 3.1 were solved in COMSOL and the resulting predictions compared with experimental data. The experimental data was obtained by coating a sheet of Teflon with our carbon black ink using a doctor blade. Teflon is a non-stick polymer that does not absorb or react with water. By coating it on Teflon instead of Nafion, we were able to study the drying of the coating in an isolated manner, without any moisture transfer to or from the saturated PEM membrane.

The experiment was performed at room temperature with air movement similar to what will be encountered during drying. The wet coating thickness was 0.890 mm, and the mass change of evaporating water was measured and reported every 30 seconds.

Figure 3.1 compares the normalized mass change obtained from experiments and our simulation. It can be seen that there is good agreement between the two.

Since Teflon is impermeable to water, the coating can dry only from the top and the sides. Hence an adjusted $\boldsymbol{A_c}$ is used for this simulation and it is given by

$$\boldsymbol{A_c} = 2l_c t_c + 2w_c t_c + l_c w_c \tag{3.10}$$

in which l_c, w_c, and t_c represent coating's length, width and thickness, respectively. This Teflon coating experiment does not mimic actual membrane coating conditions during manufacturing as it does not account for water movement from the coating to the membrane; this simulation is performed with the sole aim of computing and verifying our coating model and the value of α_{coat}. The interaction of the coating with the membrane is considered in Section 3.4.

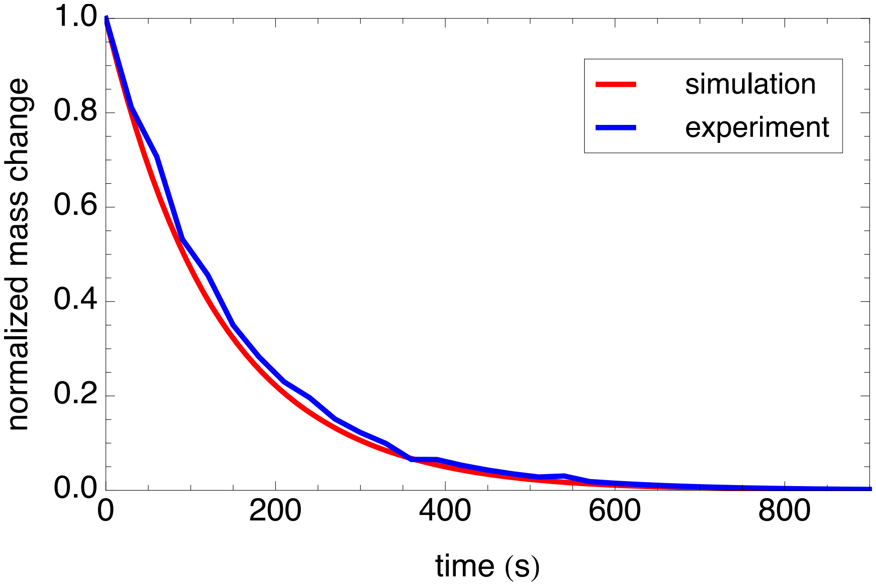

Figure 3.1: Comparison between experimental and simulation during drying of coating on Teflon

3.4 COMBINING THE MEMBRANE SWELLING AND COATING DRYING MODELS

3.4.1 Assumptions

Previous research has shown that increased fuel cell performance and minimum wrinkling defects are obtained if the Nafion membrane is pre-swelled before coating. During the pre-swelling process the Nafion membrane is completely saturated with water or some other solution (Park *et al.*, 2010) (Jones and Roziere, 2008). We will be pre-swelling the Nafion membrane in our pilot scale coating machine, details of which are discussed in the next chapter.

Since we plan to pre-swell the membrane before coating to minimize defects it is implemented in our modeling with appropriate initial conditions. In our combined coating and swelling models, we simplify the problem by considering a single sided coating only.

As mentioned before, we assume the coating to be a reservoir of water for the membrane as long as there is water present in the coating. This means that the membrane stays hydrated as long as the coating is wet and starts to lose water only after all the liquid water has completely dried from the coating.

Hence we analyze the entire membrane coating process by decomposing it into two steps. In the first, we solve for the water content in the coating, and in the second we solve for the water content in Nafion membrane, while solving for temperature T in the two cases. It should be noted that the membrane and coating are assumed to be at the same temperature since they are in contact with each other.

More simply put, we solve for m_{0c} and T while the coating is still wet, and we solve for m_0 and T as soon as the coating has dried.

3.4.2 Governing Equations and Boundary Conditions

When the coating is wet

Since the mass and heat transfer equations are written considering different control volumes, it is essential to clearly define them. The control volumes that are considered for the different equations are shown in Figures 3.2 and 3.3, which shows a cross-section of the membrane-coating assembly.

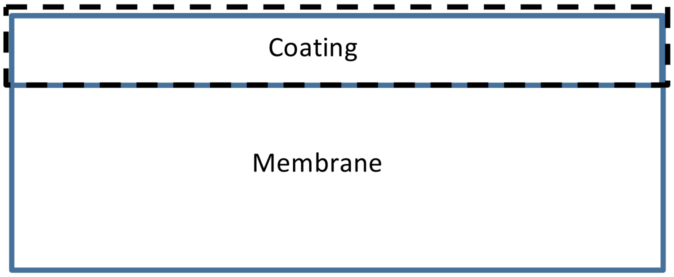

Figure 3.2: Illustration showing the control volume considered for mass transfer when the coating is wet

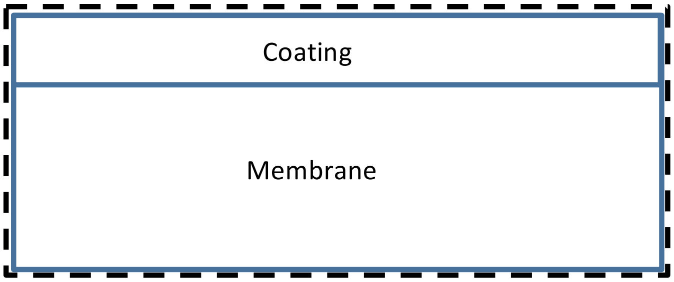

Figure 3.3: Illustration showing the control volume considered for heat transfer when the coating is wet

Figure 3.4 shows the various fluxes that we consider for solving water content in the coating. We account for the convection mass transfer from the top of the coating, and we consider water loss from the saturated Nafion membrane from the bottom. Although water is lost from the bottom surface of Nafion, it is replenished from the coating.

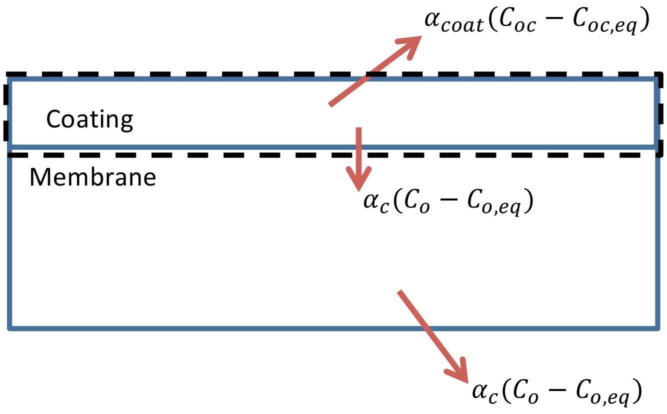

Figure 3.4: Illustration of the various water fluxes in the membrane-coating assembly

Again as explained above we ignore variation in the water content of Nafion membrane while the coating is wet, assuming that it remains saturated but account for the water lost from the coating to Nafion membrane while the coating is drying. We adapted Equation 3.1 to reflect this water loss term to get

$$\frac{{\rho_0}^2\rho_s}{(\rho_0+M_0\rho_s m_{0c})^2}\frac{\partial m_{0c}}{\partial t}=-\frac{\boldsymbol{A_c}}{\boldsymbol{V_c}}[\alpha_{coat}(c_{0c}-c_{0c,surr})+\alpha_c(c_0-c_{0,eq})] \qquad (3.11)$$

Equation 3.11 has two terms for water loss, and the term consisting of α_c refers to the water lost to Nafion membrane. Since the membrane is fully saturated, in Equation 3.11, c_0 refers to the Nafion membrane's saturated water concentration and $c_{0,eq}$ is calculated from the surrounding temperature and water activity.

The heat transfer equation shown in Equation 3.5 is then modified to include the extra water lost to the membrane. It is now given by

$$\rho_{eff}c_{p,eff}\frac{dT}{dt}=-\frac{\boldsymbol{A_{eff}}}{\boldsymbol{V_{eff}}}[2h(T-T_{surr})+\bar{h}_{fg}\alpha_{coat}(c_{0c}-c_{0c,surr})+\bar{q}_{st}\alpha_c(c_0-c_{0,eq})]$$

(3.12)

In the above equation, it can be seen that heat loss due to convection is considered from the top of the coating and bottom of the Nafion membrane. The heat loss associated with advection is also considered from the top of the coating and bottom of the membrane. These fluxes can be identified from Figure 3.5. Equations 2.35 and 3.8 are identical in this case as L and L_c have the same value. Since the convection heat loss has the same driving force $(T - T_{surr})$ for top and bottom of the system, it is combined and expressed as $2h$.

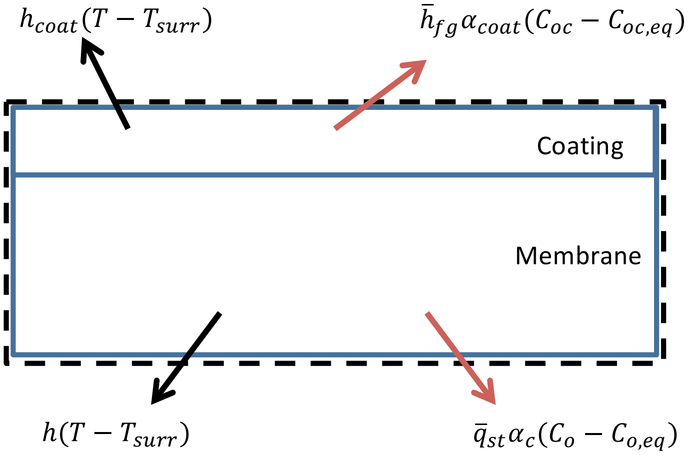

Figure 3.5: Illustration identifying the various heat fluxes in the membrane-coating assembly

In Equation 3.12, ρ_{eff} and $c_{p,eff}$ refer to the coating-membrane system's density and specific heat capacity respectively. It is calculated in a manner similar to Equations 3.3 and 3.7.

Ratio $\boldsymbol{A_{eff}/V_{eff}}$ can be reduced to $1/t_{total}$ where t_{total} refers to the overall thickness of the membrane-coating system. The total thickness is the sum of Nafion membrane's dry thickness, coating's dry thickness, and the thickness due to water present in the coating and the membrane. It is given by

$$t_{total} = t_{nafion\ dry} + t_{coating\ dry} + \frac{m_0 \rho_m M_0 t_{nafion\ dry}}{3\rho_0} + \frac{m_{0c} \rho_s M_0 t_{coating\ dry}}{\rho_0} \tag{3.13}$$

where t_{total} is time dependent because it is a function of m_{0c} and m_0 which change with time due to water loss from the membrane-coating system.

It should be noted that in Equations 3.11 and 3.12, heat loss from the sides are neglected, since the heat and mass transfer from the sides are insignificant, compared to the surfaces parallel to the airflow.

<u>When the coating is dry</u>

After the molality of water in the coating m_{0c} has approached zero, the membrane will begin to lose water. Hence the combined equations described in this section solve for m_0 and T. Figure 3.6 shows the control volume considered for mass transfer while the entities considered for T does not change and has already been outlined in Figure 3.3.

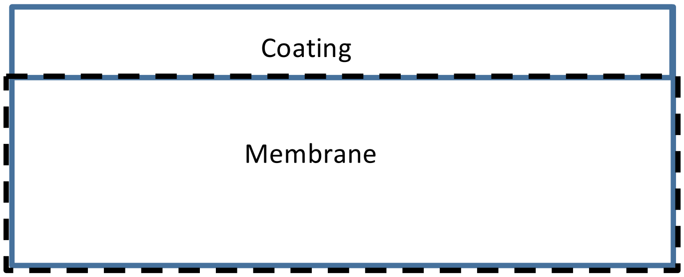

Figure 3.6: Illustration showing the control volume considered for mass transfer when the coating is dry

As mentioned before, we now consider the membrane to be able to lose water from the top and bottom after the coating has dried. We model the now dry coating to be a porous structure and model the water loss through the coating as diffusion through a porous media (Grathwohl, 1998). Figure 3.7 shows the water loss from the system after the coating has dried.

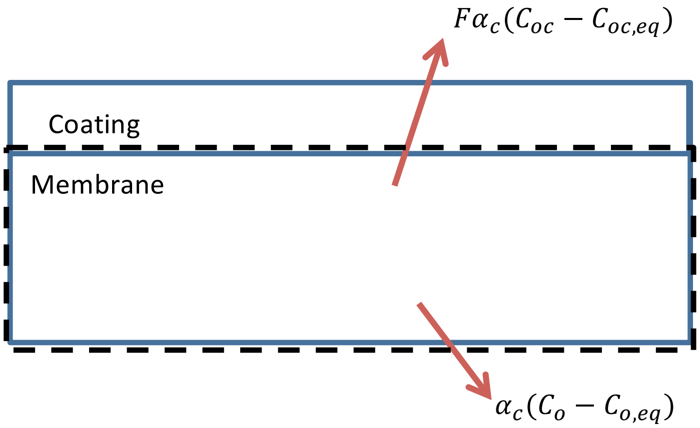

Figure 3.7: Water loss from the membrane after the coating has dried

The mass transfer equation that describes the water transport can be given by

$$\frac{\rho_0{}^2\rho_m}{(\rho_0 + M_0\rho_m m_0)^2}\frac{dm_0}{dt} = -\frac{\boldsymbol{A}}{\boldsymbol{V}}\left[F\alpha_c\left(c_0 - c_{0,eq}\right) + \alpha_c\left(c_0 - c_{0,eq}\right)\right] \tag{3.14}$$

where F is the effective diffusion coefficient factor, defined by

$$F = \frac{\varepsilon_t\delta}{\tau} \tag{3.15}$$

in which ε_t, δ, and τ are the porosity, constrictivity, and tortuosity, respectively. It should be noted that these constants can be experimentally calculated for the dry coating and are dimensionless. Values of F are necessarily less than unity, and this shows reduced flux due to the presence of porous media between the membrane and air.

The equation that describes heat transfer can be derived as

$$\rho_{eff}c_{p,eff}\frac{dT}{dt} = -\frac{\boldsymbol{A_{eff}}}{\boldsymbol{V_{eff}}}\left[2h(T - T_{surr}) + F\bar{q}_{st}\alpha_c\left(c_0 - c_{0,eq}\right) + \bar{q}_{st}\alpha_c\left(c_0 - c_{0,eq}\right)\right] \tag{3.16}$$

The various components that contribute to the heat flux in the above equation are illustrated in Figure 3.8.

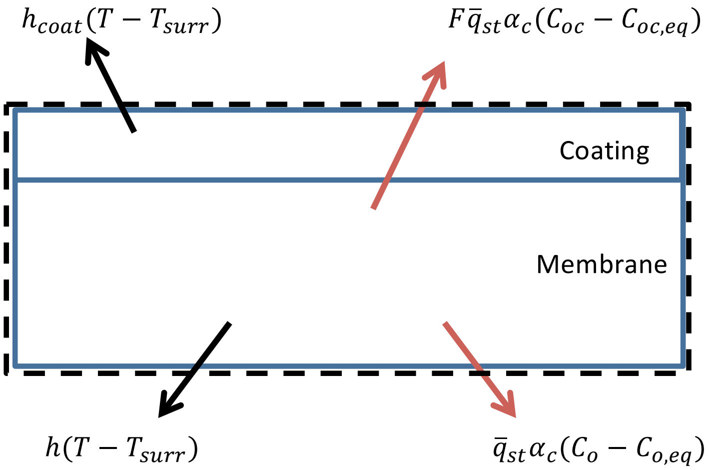

Figure 3.8: Heat loss from the system after the coating has dried

The initial condition for T in Equation 3.16 is obtained by solving Equation 3.12 and using the solution at the time when m_{0c} reaches zero.

The simulation of the combined model and its implementation for controlling the manufacturing process are further discussed in Chapter 6.

3.5 CONCLUSION

We have developed a lumped zero-dimensional model that keeps track of the water content and temperature of the coating by writing equations that solve for water molality and temperature of the coating. The results of the model compare agreeably with experimental data.

The zero-dimensional membrane swelling model and the zero-dimensional coating drying model must be combined for use in modeling an MEA manufacturing design and control strategy. Although the two models were developed separately, they were coupled together by considering the appropriate interfacial boundary conditions. Since this model is defined for a fully saturated membrane on which the coating is applied, it can be solved in two steps: The first step that tracks the molality of water in the coating along with the system’s overall temperature that is valid when the coating is still wet; And a second step that tracks the Nafion membrane’s molality along with the system temperature that is valid after the coating has dried.

Chapter 4: Modeling the Wrinkling Process

4.1 INTRODUCTION

4.1.1 Background

In order to design and control a process that successfully produces a catalyst-coated MEA for use in PEM fuel cell, a process that functions in an automated, continuous, and controlled fashion, the mechanical and thermal processes of the coating, the drying and the shrinking of the hydrated ionomeric membrane needs to be well understood. In the first part of this work, models describing these hydrating, coating and drying processes have been developed and described in detail. We now turn our attention to the question of how to prevent the formation of wrinkles during the continuous manufacturing of MEA. Wrinkling in this work is assumed to mean any critical failure in coating process that results from buckling initiated changes in the mechanical deformation gradient.

In this chapter, we develop a model that predicts the formation of creases, wrinkles, and furrows in the ionomeric membrane, based on the external forces applied to the said membrane as function of its water content distribution. As mentioned earlier, external mechanical forces, i.e. tension forces, are necessary to move the membrane through the machine. In this work, the external forces are modeled in a configuration based on processing the membrane in a continuous web form.

The moisture distribution profile needed to predict material buckling which leads to wrinkles can be obtained by combining and expanding the membrane swelling and coating drying models, as shown in the subsequent calculations. We have to add an additional dimension to the analysis since the membrane is moving through our control volume, which creates a water content gradient along the direction of motion.

We additionally point out that the combination model developed in Chapter 3 has a Lagrangian reference frame and this will not allow us to add this new dimension to the model. We later address this in Chapter 6 when we convert the model into an Eulerian reference frame and solve for the water profile in the direction of web motion.

4.1.2 Method of Approach

We started our analysis of wrinkle prediction by first developing a two-dimensional thin plate model that models the tensile and compressive stresses. We then develop a buckling criterion that applies to our membrane, apply the buckling criteria to membrane two-dimensional plate model and thus predict wrinkles.

In a later part of this work, this model will then be used to design the pre-swelling section of the pilot-scale coating line, as well as being used to select nominal operating conditions during the control of manufacturing line. The details of the application of this model in the pilot-scale manufacturing system, and its control system, are addressed in Chapters 5 and 6.

4.2 TWO-DIMENSIONAL WRINKLING MODEL

4.2.1 Assumptions

Because the membrane is in tension, wrinkles are assumed to form when the induced compressive stresses exceed a critical stress. When the critical stress value is exceeded, the equilibrium state becomes unstable and the plate begins to buckle (Timoshenko and Gere, 1961).

We can assume that all the applied forces are parallel to the membrane and uniformly distributed over the thickness. Hence the tensile and shear stresses along the thickness are assumed to be zero. This by definition is a plane stress condition and we can solve for the stresses in the mid-plane of the membrane (Timoshenko and Goodier, 1970). We can assume that the mid-plane stresses are constant through the thickness and only vary along the lateral directions.

When we model a membrane web during manufacturing, the lateral dimensions quickly become very large compared to the membrane's thickness. In this model we again consider the elastic modulus as a function of water content as given in Equation 2.44, and also include the size variations that are caused due to the presence of water as developed earlier. We also continue to assume as stated in Chapter 3, that the membrane is considered a load-bearing member, and that the coating is assumed to be flexible and free to expand and contract with the membrane without loading the membrane.

Since the mass of the membrane is negligible compared to the forces applied to the web during manufacturing, the body forces are ignored. Moreover, since the membrane moves with a constant velocity through the machine, its inertial forces are also ignored.

4.2.2 Governing Equations and Boundary Conditions

We consider the web's mid-plane to have a rectangular geometry and the tensile forces, denoted by F, that are applied during manufacturing are shown in Figure 4.1 along with the coordinate directions x and y.

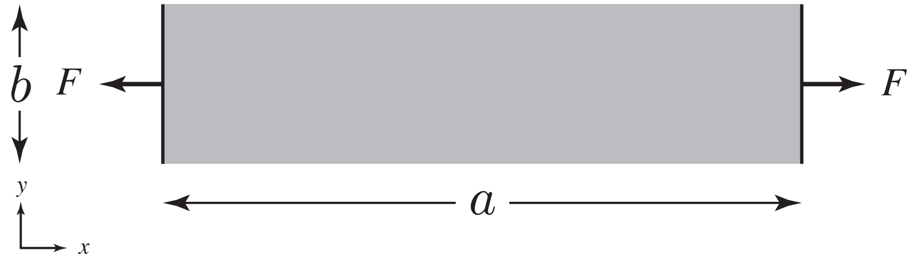

Figure 4.1: Forces applied to a section of the web during manufacturing

It should be noted that the piece of the membrane shown above is a small section of the continuous web between two adjacent rollers moving through the machine. The rollers are assumed to behave in a simply supported fashion, hence, the simply supported edge boundary conditions is implemented for the two short edges.

It is also assumed that the longer edges are free to translate and rotate because of their free boundary. In the model these are implemented as free edge boundary conditions for the two longer edges. It should be noted that the simply supported and the free edge boundary conditions as implemented are used to calculate the reaction forces at the boundaries.

Since we decided to ignore the inertial and body forces, the equation of motion for an infinitesimal two-dimensional control volume (Malvern, 1969) as expressed previously in Equation 2.41 is

$$\nabla \cdot \mathbf{T} = 0 \tag{4.1}$$

with the accompanying Duhamel-Neumann form of the Hooke's law modified to include the effect of swelling due to water

$$\mathbf{T} = \mathbf{C}\colon [-K\bar{V}_0 m_0 \rho_m + \epsilon] \tag{4.2}$$

where the expansion due to temperature is neglected. The various constituents of Equation 4.2 has been explained previously in Chapter 2.

Equations 4.1 and 4.2 were then solved in COMSOL for the membrane piece shown in Figure 4.1, with the boundary conditions described above, using the finite element method. The output of this model is the stress tensor $\mathbf{T}$, whose components provide the induced tensile and compressive stresses. It is expected that the compressive stress σ_y causes buckling when it exceeds the critical buckling stress, explained in Section 4.2.3.

Above equations can be solved for multiple and various moisture content profiles with identical boundary conditions in order to determine the moisture profile that causes the least wrinkles or defects.

4.2.3 Buckling Criteria

Let us consider a rectangular web with dimensions a and b and let us assume it is stressed in a fashion as shown in Figure 4.2. It can be understood from Poisson's effect that as σ_x increases (more tensile), there is an induced stress, represented by $\sigma_{y,ind}$, that decreases (more compressive). It is understood from Timoshenko (1940) that this $\sigma_{y,ind}$ has a limit called the critical compressive stress, $\sigma_{y,cr}$, which if exceeded causes buckling. This buckling is an elastic deformation in the thickness, but when it is pulled into crease on the roller, it becomes a permanent wrinkle.

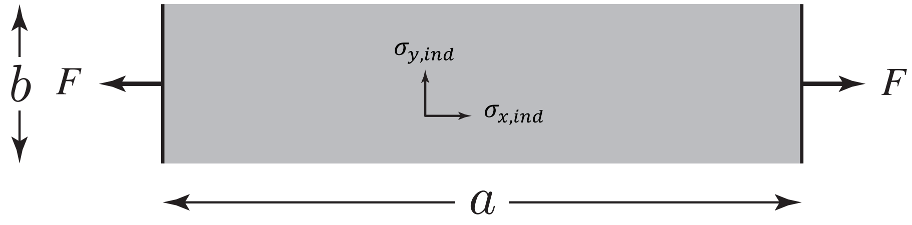

Figure 4.2: Stresses applied to a rectangular web

Saint-Venant derived an equation that describes the deflection of a surface when forces per unit distance N_x, N_y and shear force N_{xy} act on an infinitesimal two-dimensional control volume

$$\frac{\partial^4 w}{\partial x^4} + 2\frac{\partial^4 w}{\partial x^2 y^2} + \frac{\partial^4 w}{\partial y^4} = \frac{1}{D}\left(N_x \frac{\partial^2 w}{\partial x^2} + N_y \frac{\partial^2 w}{\partial y^2} + 2N_{xy}\frac{\partial^2 w}{\partial x \partial y}\right) \tag{4.3}$$

where w is the out-of-plane deflection and D is flexural rigidity that is expressed by

$$D = \frac{Et^3}{12(1-\nu^2)} \tag{4.4}$$

with ν the Poisson's ratio, E the elasticity modulus defined in Equation 2.44, and t the thickness of the membrane. The LHS of Equation 4.3 describes the effect due to bending and the terms on the RHS describe the effect due to the applied forces. In this equation body forces are ignored.

The deflections at the edges of the plate are assumed to be zero, and the solution to Equation 4.3 is assumed to be of the form

$$w = \sum_{m=1}^{\infty}\sum_{n=1}^{\infty} a_{mn} sin\frac{m\pi x}{b} sin\frac{n\pi y}{a} \tag{4.5}$$

where m and n are the number of half-waves in the membrane's buckled shape in the x and y directions, respectively. The form shown in Equation 4.5 is chosen such that the solution to w satisfies the assumed deflections on the boundaries. An energy method can be used to obtain a solution to the equation where the work done by the bending moments are equated to the work done by the compressive stresses (Timoshenko, 1940).

Using the energy method to derive a solution to Equation 4.3 in the form expressed in Equation 4.5, one gets: (Roark and Young, 1975)

$$\sigma_{x,cr}\frac{m^2}{a^2} + \sigma_{y,cr}\frac{n^2}{b^2} = 0.823\frac{Et^2}{1-\nu^2}\left(\frac{m^2}{a^2}+\frac{n^2}{b^2}\right) \tag{4.6}$$

where $\sigma_{x,cr}$ and $\sigma_{y,cr}$ are the critical stresses in the x and y directions respectively. In Equation 4.6, compressive stresses are assumed to be positive and tensile stresses negative. During the derivation of Equation 4.6, N_{xy} is assumed to be zero. It should also be noted that N_x and N_y are assumed to be uniform throughout the boundary that they represent.

In our manufacturing case, we are interested to know $\sigma_{y,cr}$ for a given N_x. Since it is assumed that the applied force per unit length N_x, induces stresses $\sigma_{x,ind}$ and $\sigma_{y,ind}$ in the x and y directions, this is obtained by fixing $m = 1$ and calculating the ranges for $\sigma_{x,ind}$ for positive incremental values for n using (Roark and Young, 1975)

$$0.823\frac{Et^2}{(1-\nu^2)a^2}\left[1-n^2(n-1)^2\frac{a^4}{b^4}\right] > \sigma_x > 0.823\frac{Et^2}{(1-\nu^2)a^2}\left[1-n^2(n+1)^2\frac{a^4}{b^4}\right] \tag{4.7}$$

The ranges for $\sigma_{x,ind}$ are used to calculate $\sigma_{y,cr}$ using a variation of Equation 4.6

$$\sigma_{x,ind}\frac{m^2}{a^2}+\sigma_{y,cr}\frac{n^2}{b^2}=0.823\frac{Et^2}{1-\nu^2}\left(\frac{m^2}{a^2}+\frac{n^2}{b^2}\right) \tag{4.8}$$

4.2.4 Usage of the Buckling Criterion

For a given moisture distribution profile and applied tensile forces, Equation 4.2 is solved to find the induced $\sigma_{x,ind}$ and $\sigma_{y,ind}$ for a particular value of N_x. We find the minimum $\sigma_{x,ind}$ in this stress distribution and use Equation 4.7 to find n. This n is used in Equation 4.8 to calculate $\sigma_{y,cr}$. We then compared $\sigma_{y,cr}$ to $\sigma_{y,ind}$ at the short edges of the membrane piece and predict wrinkle formation if $\sigma_{y,ind}$ exceeds $\sigma_{y,cr}$.

4.2.5 Application to Nafion

As discussed in Section 2.2.4, the elastic modulus of Nafion is dependent on water content and temperature. Equation 2.44 was used to calculate the elastic modulus for different conditions for Nafion. Figure 4.3 shows the variation of the elastic modulus to Nafion's water activity at 298 K.

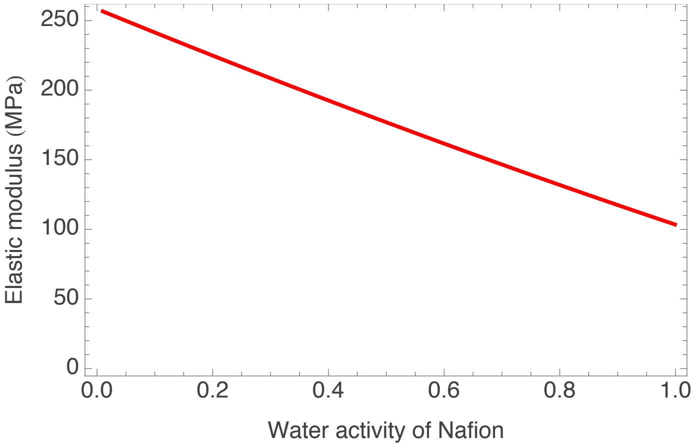

Figure 4.3: Elastic modulus of Nafion vs water activity at 298 K

The relationship between $\sigma_{y,cr}$ and the induced σ_x for $a = 0.4$ and $b = 0.1$ is shown in Figure 4.4. It should be noted that a and b are in meters, and the elastic modulus $E = 99.95$ MPa, which is calculated when Nafion is fully saturated with water.

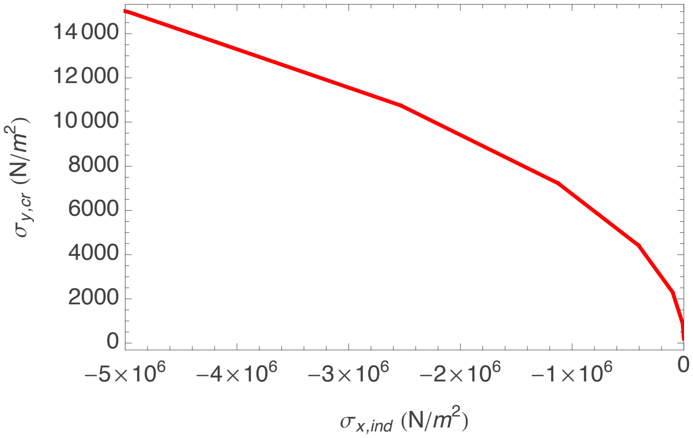

Figure 4.4: $\sigma_{y,cr}$ vs $\sigma_{x,ind}$ when Nafion is fully saturated

Figure 4.4 is plotted following the convention that tensile stresses are negative and compressive stresses are positive.

4.2.6 Justification of Applying Buckling Criteria to our membrane

The buckling criterion was derived assuming that the membrane is rectangular. Our membrane however will not be perfectly rectangular because of its varying water content and the strains associated due to the water uptake.

We tried to quantify this deviation by calculating a geometric transformation function that transforms the distorted trapezoidal shape to a rectangular shape. The coefficients of this function will determine the extent of this deviation (Mortenson, 1995).

Figure 4.5 shows the actual trapezoidal membrane shape super imposed on a rectangular shape. This is for $a = 0.4$ and $b = 0.1$ meters. The left boundary is completely saturated whereas the right boundary is fully dry with the profile between them linear.

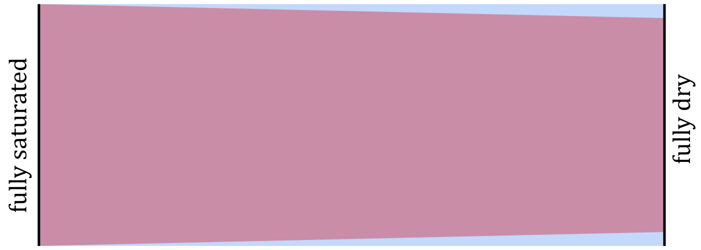

Figure 4.5: Membrane's trapezoidal shape superimposed on a rectangle

A transformation function that permits translation, rotation and scaling is calculated to be

$$\begin{aligned} \hat{x} &= -0.00102168 + 1.0067x \\ \hat{y} &= -0.00039344 + 1.0067y \end{aligned} \tag{4.9}$$

where $\hat{x}$ and $\hat{y}$ represent the coordinate system of the transformed rectangle, while x and y are the coordinate system of the membrane. It can be seen that the coefficients of the Equation 4.9 can be approximated to a one to one mapping because of their magnitude, and hence it is justified to apply the derived buckling criterion to our membrane system.

The dimensions used to calculate the transformation function are similar to the ones encountered in the actual pilot-scale coating line constructed as part of this work. It should be noted that in the assumptions used to calculate Equation 4.9, the membrane goes from being fully hydrated to completely dry over a very short distance, and this is a very steep gradient compared to what is implemented in the pilot-scale coating line. In other words, no section of our coating process has a water profile gradient as severe as the ones assumed to derive the transformation function, hence it is valid to approximate the membrane's shape as a rectangle for much less severe cases like the ones encountered in our pilot-scale machine.

4.3 CONCLUSION

We developed a two-dimensional plane stress model and solved that model in COMSOL by calculating the stresses induced in the web during manufacturing. This model takes into account the water content gradient and the external forces that are applied.

We adapted a buckling criterion that predicts wrinkles based on the comparison between the induced and critical compressive stresses. We developed this model under the assumption that buckling that occurs near the rollers, will be creased on to the membrane as permanent defects, and we anticipate to use this model to design the process operating conditions that avoids such defects.

Chapter 5: Design of a Pilot-Scale Proton Exchange Membrane Coating Line

5.1 INTRODUCTION

5.1.1 Background

In the previous chapters, we first developed and then partly tested a computer model that describes the rather drastic moisture content based behavior of a coated ionomeric membrane during the manufacturing process. We additionally developed a model that predicts buckling behavior or so called wrinkles based on the membrane's water content and applied forces.

As mentioned briefly in the introduction to this work, one of the goals was to address issues associated with implementing a model-based controller with the ultimate aim of using a model-based strategy to minimizing defects due to wrinkling. In order to experimentally test our hypothesis and the reliability of our model and controller, we constructed a pilot-scale coating line, which in addition to ultimately allowing implementation of the designed coating process on actual hardware, also acted as test bed for developing fundamental understanding of the steps in the coating process.

5.1.2 Pilot-Scale Coating Line Design Approach

We begin with the design of the coating line by first selecting the conditions under which the coating is to be applied and then dried. Our pilot scale line was mechanically designed to accept rolls of uncoated membrane, advance the membrane to a pre-swell section, to a coating section, and then to a drying section in a continuous fashion. Below we describe and discuss the design under consideration associated with each processing step and the integration of these steps and components into a pilot scale coating line that was constructed as part of this work. We note that our wrinkling model as described in the previous chapters was used to optimize the design of the machine parameters and control strategy.

5.2 COATING PROCESS DESIGN

5.2.1 Pre-Swelling

As mentioned before, a significantly lower number of coating defects have been observed when the PEM is pre-swelled or saturated with water prior to coating (Park *et al*, 2010). The decrease in coating defects happens because the sudden or uneven water uptake that occurs during direct application of the liquid coating on a dry membrane is avoided (Hsu and Wan, 2003). When the membrane is fully saturated with water, it simply cannot absorb any water from the liquid coating, knowing this helps us track or "do the bookkeeping" of the water contents in the membrane and coating more quickly and effectively by putting the material into a known state. Moreover, it has been found through practical experimentation that it is easier to apply a wet coating on a saturated membrane. This is because coating a saturated membrane rather than a dry one, results in avoiding the sudden change of membrane shape that occurs when a dry membrane is first brought in contact with liquid (Wheeler and Sverdrup, 2007). The MEA fabrication process could benefit from a better design and model-based control of the pre-swelling or saturation step.

Two mechanical possibilities for pre-swelling the membrane were then considered; pre-swelling by humidified air and pre-swelling by immersion in water. For humidified air pre-swelling, there exists an appreciable mass transport barrier when the membrane is exposed to humidified environments with different water activities that limit the rate of moisture adsorption by the membrane. This has been demonstrated previously in Equation 2.28. However, the mass transport barrier when exposed directly to liquid water can be neglected (Weber and Newman, 2009). This means that liquid water can be drawn into the membrane as quickly as it can diffuse through the bulk of the membrane, thus arguing for pre-swelling by water immersion on grounds of speed.

Moreover, pre-swelling with humidified air requires extremely long coating lines owing to the time needed for sufficient moisture to overcome the mass transport barrier. If long coating lines are to be avoided, and pre-swelling by humidified air still utilized, then alternatively the velocity of the web through the pre-swelling section could be slowed to achieve necessary absorption time. However making the design commitment to a slow speed strategy would have prevented the pilot-scale line from acting as a test bed for higher yield rates upon further scales up. These considerations support the selection of water immersion pre-swelling.

5.2.2 Two-Stage Drying

The molality of water in the wet ink coating when it has just been applied is very large when compared to the molality of water in the saturated membrane to which it is being applied. For a given size of saturated ionomeric membrane that has just been coated, the ratio between the number of moles of water in the coating to the number of moles of water in the membrane is approximately thirty. The manufacturer's recommended storage conditions for Nafion are 50% relative humidity at 23°C and it is ideal if the finished coated membrane exits the process line equilibrated at these temperature and humidity conditions (DuPont, 2004). However, if the coated membrane were dried at these recommended storage conditions, it would again imply that the coating line has to be very long or run at a very low speed.

Earlier in this work we concluded that during the drying of the freshly coated saturated membrane the coating rehydrates the membrane, keeping it fully hydrated as long as water is present in coating. Even if using some potentially harsh drying conditions that quickly remove water from the membrane, no undesirable effects have been reported in the membrane's shape because it remains hydrated (Silverman, 2010).

This suggests that it is possible to employ two-stage drying, where a first stage rapidly removes the water from the coating and a second stage that then brings the membrane to the recommended storage conditions. Introduction of two-stage drying in coating line would be a useful addition to the ionomeric membrane coating process and we address that issue below.

Since the ionomeric membrane holds such a small quantity of water compared to the amount of water in the coating, the excess drying potential available in a first hot and dry section will likely over-dry the membrane, requiring that it will have to be re-swelled to the storage conditions. Recalling Equation 2.28, it can be seen that the mass transport barrier, α_c, for absorption is greater than desorption, and this will further affect the design of the coating line, by adding to its length.

Previous research on two-stage drying has shown that controlling the time spent in the hot/dry zone and the timing of the transition from the hot and dry zone to the second, cooler zone is very important (Silverman, 2010). Transitioning too early results in the coating not being completely dry, while transitioning too late would mean that the membrane is over dried. One additional aspect of this work was to design and build in the pilot-scale line two-stage drying, with the further aim of using our model based control system to control the time of the first stage drying and the timing of the transition between stages.

5.3 MACHINE DESIGN

As a major part of this work, we designed, constructed, and tested a pilot scale membrane coating line, which can produce a catalyst-coated membrane in a continuous fashion using rolls of uncoated membrane. At the time of writing this dissertation, Nafion is the only PEM that is available in rolls, Subsequently the pilot scale coating line was designed to accommodate Nafion ionomeric membrane available in 10 cm wide roll form.

Since it is a continuous process, there needs to be a control of the web's tension, and velocity. We have discussed the design considerations and rational for adding a water immersion pre-swelling and two-staged drying to our pilot scale coating line and we now turn our attention to the details of machine construction.

An overview of our pilot scale membrane coating line is shown in Figure 5.1. It should be noted that the Nafion web moves in a clock-wise direction through the machine. The uncoated and coated rolls of Nafion are in the left most chamber.

This machine has the capability to independently change the unwind and rewind tensions in the web. There is a traction roller that friction-feeds the membrane web and advances it through the machine at a set point velocity. The membrane web is supported throughout the machine by aluminum idle rollers.

In addition to this, the machine has a pre-swelling section and seven independent temperature-humidity controllable drying chambers. Although we employ a doctor blade method to coat ink, it can be changed to any other method of ink application for future research. Since this line deals with aqueous swelling and wet coating of ionomeric membranes, most of the critical components were procured and built to withstand prolonged moisture exposure.

Since roll-to-roll processes are common in the textile and print industry, a large base of knowledge exists on the topic. The motor drives and roller mechanisms are adapted from readily available off the shelf parts. The machine's super structure and frame was constructed from T-Slotted aluminum available from 80/20 Inc. (8020, 2012).

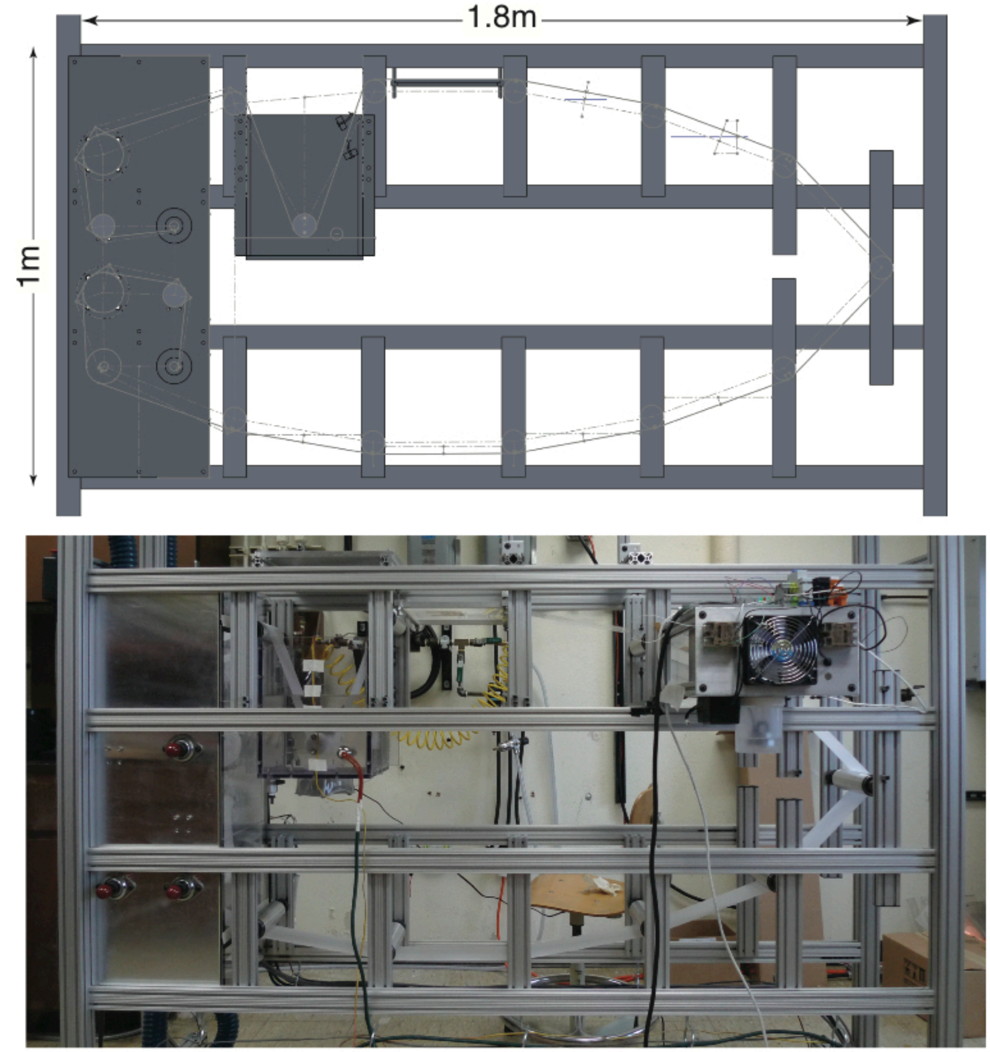

Figure 5.1: Overview of the membrane coating machine

5.3.1 Uncoated and Coated Membrane Storage

Since it is best to store the coated and uncoated Nafion rolls at the recommended storage conditions, it is essential to have a start and end block, that is temperature and humidity controlled, as shown in Figure 5.2. This can prevent damage to the roll when left in the machine for extended periods of time. A stand-alone Proportional-Integral-Derivative (PID) controller is used to control the humidity and temperature of the start block. This controller was implemented using an Arduino Duemilanove programmable microcontroller, necessary relays, and related accessories.

This section has a dedicated heater, humidifier, and supply of dry air to control the temperature and humidity.

Figure 5.2: Coated and uncoated membrane roll storage

5.3.2 Web Tension and Velocity

Pneumatically actuated expanding chucks secure the rolls of coated and uncoated Nafion. On one side of the storage chamber described in Section 5.3.1, there are two brushed DC motors mounted on the side that apply opposing torques for the unwind and rewind chucks. These torques that are applied to the chucks, translate as tensions in the web during manufacturing. To measure the unwind and rewind tensions in the web during manufacturing, there are two tension transducers (polished rollers in Figure 5.2).

There is another brushed DC motor that is geared to a rubber traction roller for moving the Nafion at a controlled speed. An optical encoder mounted on the motor is used to measure the speed. This traction roller is positioned just in front of the chuck on which the coated Nafion roll is gripped.

Figure 5.3 shows the positioning of the three DC motors. These motors have their own dedicated amplifiers cum controllers and are manufactured by Minarik Automation and Control.

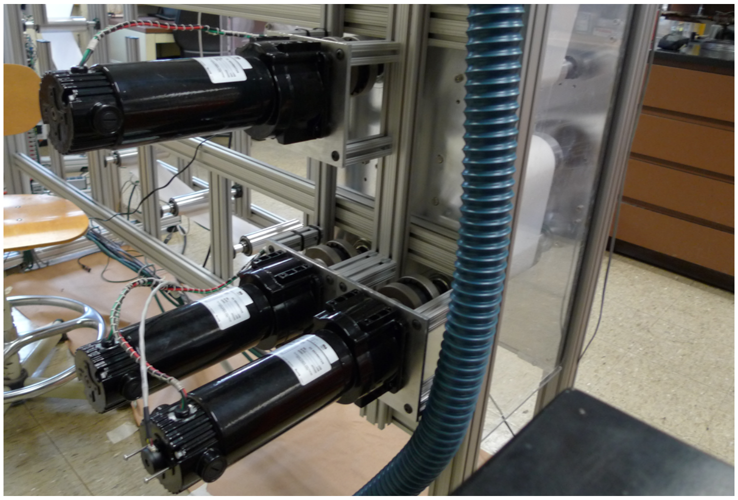

Figure 5.3: Two DC motors employed to apply unwind and rewind torques to the chucks and the third motor drives the traction roller

5.3.3 Design of the Pre-Swelling Section

Although the general design of the machine was fairly straightforward, the swelling tank design was poorly documented in literature. Since the mass transport barrier for Nafion is negligible when contacted with liquid water, the membrane will experience a rapid swelling as it passes through the tank. This sudden swelling can give rise to elastic buckling, which will become permanent when passing over one of the rollers.

For the scope of this work, the design of the pre-swelling section was very critical, in that it is the first location in the coating process workflow where wrinkles become permanent. We used the output of the wrinkling model analysis as developed in Chapter 4 to set the design parameters of the swelling tank and associated rollers, shown in Figure 5.4.

In the pre-swelling section of the machine, a piece of Nafion, equilibrated at 50% RH and 23°C, is dunked or quenched in liquid water. The membrane immediately changes shape and starts to buckle at the membrane-water-air interface. This is because of a mismatch in the water-induced strain. This elastic buckling propagates along the direction of web motion before vanishing after some distance from the membrane-water-air interface. Idler rollers are used to support the membrane and to manipulate the direction of the web throughout the entire coating process. The buckling due to the sudden swelling becomes permanent if it passes over the idler rollers. Moreover, there needs to be a minimum distance defined between the membrane-water-air interface and the next immediate idler roller. This distance is expected to depend on the tension and speed used to move the membrane through the machine.

Figure 5.4: The pre-swelling tank

In Figure 5.4, Nafion enters the swelling tank from the top on the left side and leaves the tank on the right side. There is an idler roller made from polycarbonate that is submerged in water. The formation of permanent wrinkles depends on the distance between the submerged roller and the roller on the top left, the level of water above the submerged roller, and the force used to pull the web through the pre-swelling section. Due to space constraints on the machine, the distance between the two rollers was set to 0.32 meters. The minimum force required to advance the web through the machine overcoming friction at the bearings, etc. was 4.5 N and this was determined experimentally.

Figure 5.5 shows the simulation results of the wrinkling model for different water levels in the tank. It can be noted from the simulation results that too little water in the tank will cause permanent deformations at the submerged roller, and too much water in the tank may cause permanent deformations at entry roller. This means that the membrane-water-air interface must be at a minimum distance from both the rollers to prevent permanent defects. The shaded regions in Figure 5.5 are the regions where the induced compressive stress in the y direction, $\sigma_{y,ind}$, exceeds the critical compressive stress, $\sigma_{y,cr}$, and is where wrinkles are initiated.

Based on the simulation results that were performed for a 0.32 x 0.1 m web, the preferred water height in the tank was chosen to be 0.19 m above the submerged roller. It should be noted that the wrinkling model could be used to design a swelling-tank for other operating conditions or membrane types.

In can be recalled from Section Three that a very small concentration of iso-propanol is added to the ink to decrease its surface tension. We matched the concentration of iso-propanol in the water present in our swelling tank to that of the test ink. However, our calculations are based on pre-swelling with water and the concentration of alcohol in the swelling tank is ignored because of its negligible concentration and unavailability of Nafion uptake and swelling data.

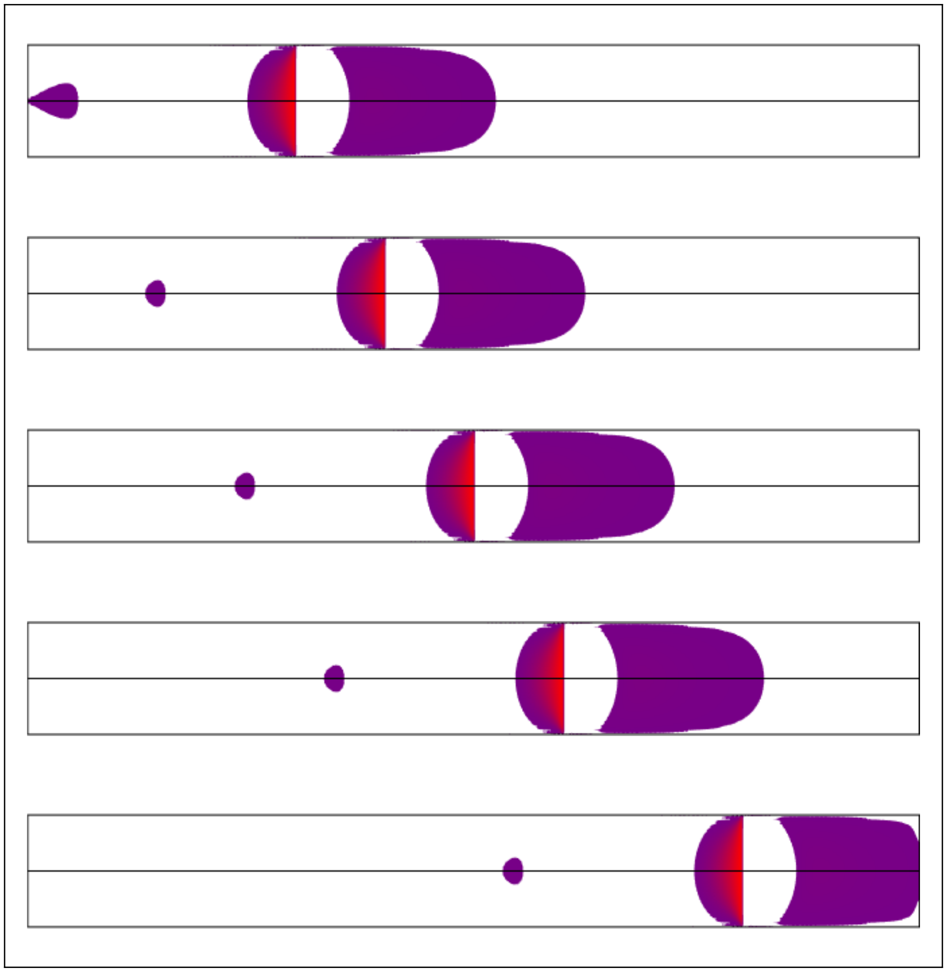

Figure 5.5: Wrinkling model simulation results showing regions exceeding critical compressive stress for water heights of 22, 19, 16, 12 and 7 cm from the submerged roller (figures from the top)

It should also be noted that the pre-swelling tank has a heater that can pre-heat the water if needed. A J-type thermocouple is used to measure the temperature, which is controlled by a Eurotherm auto-tune PID temperature controller. The magnetic stirrer shown in Figure 5.4 is used to prevent any temperature gradients in the water that arise due to insufficient mixing.

5.3.4 Ink Application

As mentioned before, a doctor blade coating system is used to apply the coating on the membrane. This coating is applied on a flat PTFE-coated glass plate to reduce friction. Figure 5.6 shows the doctor blade along with a peristaltic pump. The pump feeds the wet catalyst ink into the doctor blade and helps maintain a uniform head of ink. The ink flow rate may be adjusted by adjusting the peristaltic pump depending on doctor blade gate height, coating speed, etc.

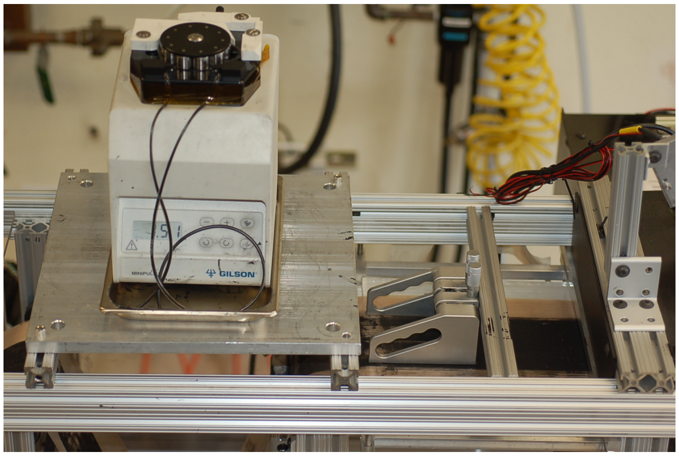

Figure 5.6: The doctor blade and peristaltic pump in the coating section

When Nafion exited the swelling tank, some droplets of water were found to cling onto the membrane's top and bottom surfaces. This interferes with uniform coating application, so a wiping step was added before coating. To wipe the surface droplets of water, a simple absorbency-based pad was used as shown in Figure 5.7. In future implementations, the task of removing the excess droplets of water could also be achieved by an air-knife or a squeegee arrangement.

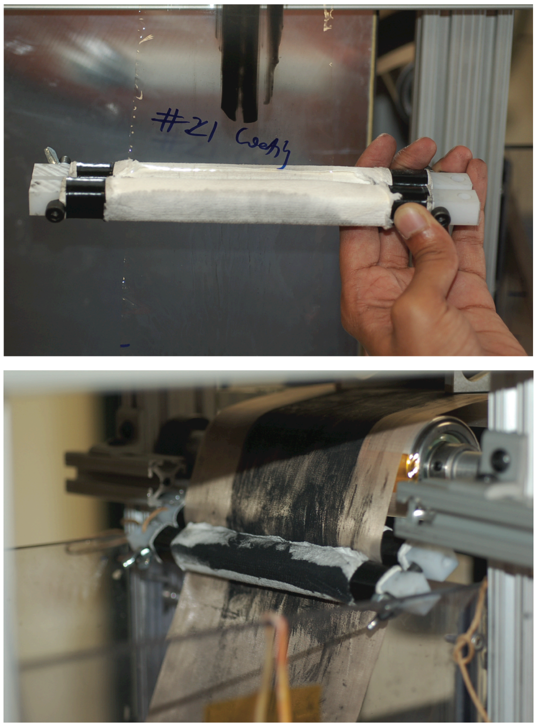

Figure 5.7: Absorbency-based pad to wipe excess water after pre-swelling

5.3.5 Humidity and Temperature Controlled Drying Zones

Our membrane-coating pilot scale line has seven independently controllable temperature-humidity drying zones. Although in this research we used only two distinct zones to test the effectiveness of a model-based controller, the seven zones were constructed to accommodate future research.

Figure 5.8 shows a drying zone, viewed from the upstream and downstream sides.

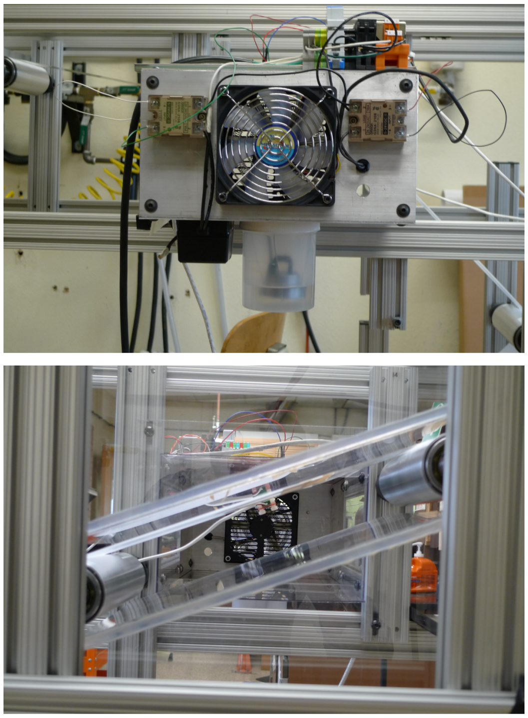

Figure 5.8: Upstream (top photo) and downstream (bottom photo) of a temperature-humidity controlled drying zone

Each drying zone dries a span of web that is approximately 30 cm long. Each zone forces heated humidified air in the transverse direction and contains an axial blower, a resistive heater, an ultrasonic humidifier, and water reservoir. The temperature and humidity of the eight zones can be controlled independently using PID controllers. The heater and humidifier are switched on and off using solid-state relays. SHT15 is a digital temperature and humidity sensor that is used to measure the conditions of the zone. The PID controller, necessary measurements, and on-off commands are handled on the computer using LabView and their Data Acquisition system.

5.3.6 Electrical Panel

The machine's electrical panel is shown in Figure 5.9. This panel bears the power supplies for the machine and related accessories, amplifiers and controllers for the DC motors, amplifiers for the tension transducers, swelling-tank temperature controller, and Labview's Data AcQusition system (DAQ). All the measurement sensors are read on the computer through the DAQ.

Figure 5.9: The electrical panel of the machine

The on-off commands for the heaters and humidifiers, web tension and web velocity set points are processed and sent by the LabView program through the DAQ.

5.4 CONCLUSION

In this chapter a candidate process was designed for the production of continuous defect-free roll-to-roll MEAs. This process involves pre-swelling and two-staged temperature-humidity controlled drying of the membrane. We built a machine to test this manufacturing process by implementing model-based control. It should be noted that the knowledge gained from the models developed in Chapters 2 and 3 were used to design the coating process while the wrinkling model was used in designing the pre-swelling section of the machine.

Chapter 6: Implementation of Model Based Control

6.1 INTRODUCTION

6.1.1 Background

One significant aim of this research was to develop a model-based controller for a continuous roll-to-roll MEA fabrication process. Our intent was to implement this controller using the combined coating-membrane hydration model that was developed in the first part of this work. In the previous chapter we discussed how we designed a pilot-scale coating line to implement a coating process utilizing pre-swelling and a two-staged drying strategy. In this chapter we now describe how we used the previously developed dynamic models to develop and implement the model-based controller on our pilot-scale coating line.

Although the differential equations that we previously developed were tested to be accurate when compared against individual sets of experimental data, we start with the assumption that the model is not perfect. And since it is also not possible to measure all the state variables at once without significant measurement noise, it is necessary to implement an estimator that combines some measurements from the machine with predictions from the model in order to obtain an estimate with improved accuracy. We chose to implement a discrete-time Linear Quadratic Gaussian (LQG) type controller, which is a combination of a discrete-time Linear-Quadratic Regulator (LQR) and a Linear Kalman Filter. The development process of this type of stochastic control is explained in this chapter.

6.1.2 Method of Approach

To successfully design the controller, it is necessary to have the model and its equations in a control-friendly form. We achieve this by converting our combined

Lagrangian reference frame model to an Eulerian reference frame, and then using the "method of lines" to convert the resulting partial differential equations into a set of ordinary differential equations. We use these ordinary differential equations to obtain the nominal operating conditions, and then use these conditions to linearize the ordinary differential equation system. This linearized state-space model is used to design the linear-quadratic regulator and Kalman estimator, while the non-linear model was used to test the LQG's performance when dealing with nonlinearities.

It should be noted that we have divided the modeling of the drying process into two distinct processes as explained in Chapter 3; in the first only the coating's water content is computed during drying and in the second the water content in the membrane is tracked when the system is brought to storage conditions. This two-staged drying is implemented in our control strategy. The region where only the coating loses water is referred to as zone one and the region in which the membrane dehydrates is referred to as zone two. We intent to control the transition between the two zones, so that the transition happens when the coating becomes just dry.

As stated, the linearized state-space model was used to develop the linear quadratic regulator (LQR), which is then the controller for the pilot-scale coating line. The selection of the weight matrices for the state and input vectors are discussed and its closed loop response is simulated assuming full-state feedback. Finally, the design of the linear quadratic estimator (LQE) commonly known as the Kalman filter is discussed (Kalman, 1960). The selection of the measurements, configuration and selection of practical values for the measurement covariance matrix are discussed before the estimator and controller are implemented on the pilot-scale line.

Developing the equations necessary to implement control for the two drying zones is discussed; however, the development of the LQG is shown only for the first zone and not repeated for the second zone because of the similarity in procedure.

6.2 EQUATIONS FOR MODEL BASED CONTROL (ZONE 1)

In the first drying zone, the governing equations that represent the evolution of the molality of the coating, m_{0c}, and the temperature of the membrane coating assembly, T, is given by Equations 3.11 and 3.12. These equations do not account for the movement of the web through the first drying zone, as they are scalar functions. However, because of steady motion of the web through the drying zone, some sections of the membrane will enter the zone before others and will thus get dryer since they have spent more time in the hot environment of the drying zone than sections entering at a later time. The moving web thus causes a gradient in the water content and the temperature of the membrane along the direction of motion. We need to "bookkeep" the gradients caused by the web motion by adding another dimension to the analysis we do this by converting from a Lagrangian to a Eulerian Reference Frame as explained below.

6.2.1 Conversion from Lagrangian to Eulerian Reference Frame

By rewriting Equations 3.11 and 3.12 and replacing $\boldsymbol{A_c/V_c}$ and $\boldsymbol{A_{eff}/V_{eff}}$

$$\frac{{\rho_0}^2\rho_s}{(\rho_0+M_0\rho_s m_{0c})^2}\frac{dm_{0c}}{dt}=-\frac{1}{t_{coating}}[\alpha_{coat}(c_{0c}-c_{0c,surr\,1})+\alpha_c(c_0-c_{0,eq\,1})] \tag{6.1}$$

$$\rho_{eff}c_{p,eff}\frac{dT}{dt}=-\frac{1}{t_{total}}[2h(T-T_{surr\,1})+\bar{h}_{fg}\alpha_{coat}(c_{0c}-c_{0c,surr\,1})+\bar{q}_{st}\alpha_c(c_0-c_{0,eq\,1})] \tag{6.2}$$

where $c_{0c,surr\,1}$ represents the exterior water molality for the coating and $c_{0,eq\,1}$ the membrane's equilibrated water concentration at the drying conditions specified for the first zone. The first zone's temperature is denoted by $T_{surr\,1}$, with the addition of the '1' to the already existing subscript to notate the drying conditions in zone one to prevent confusion with the second zone during the implementation of two-stage drying.

Converting the above equations from a Lagrangian reference frame to the Euleraian reference frame allows us to account for the convection heat and mass transfer gradients occurring due to web motion. We achieve this by replacing the regular derivative operator d with the material derivative operator D. This operator when implemented on an example function ζ yields

$$\frac{D\zeta}{Dt} = \frac{\partial\zeta}{\partial t} + \mathbf{v}.\nabla\zeta \tag{6.3}$$

where $\mathbf{v}$ represents the velocity vector and $\mathbf{v} = v_x\hat{\imath} + v_y\hat{\jmath} + v_z\hat{k}$ where $\hat{\imath}$, $\hat{\jmath}$, and $\hat{k}$ are the unit vectors in x, y, and z respectively. In our pilot-scale line, since the web moves only in one direction, we can set $v_y = v_z = 0$.

When operator D as shown in Equation 6.3 is implemented in our system of equations instead of the d operator, Equations 6.1 and 6.2 become

$$\frac{{\rho_0}^2\rho_s}{(\rho_0 + M_0\rho_s m_{0c})^2}\frac{Dm_{0c}}{Dt} = -\frac{1}{t_{coating}}[\alpha_{coat}(c_{0c} - c_{0c,surr\,1}) + \alpha_c(c_0 - c_{0,eq\,1})] \tag{6.4}$$

$$\rho_{eff}c_{p,eff}\frac{DT}{Dt} = -\frac{1}{t_{total}}[2h(T - T_{surr\,1}) + \bar{h}_{fg}\alpha_{coat}(c_{0c} - c_{0c,surr\,1}) + \bar{q}_{st}\alpha_c(c_0 - c_{0,eq\,1})] \tag{6.5}$$

which then simplifies to become

$$\frac{{\rho_0}^2\rho_s}{(\rho_0 + M_0\rho_s m_{0c})^2}\left[\frac{\partial m_{0c}}{\partial t} + \mathbf{v}.\nabla m_{0c}\right] = -\frac{1}{t_{coating}}[\alpha_{coat}(c_{0c} - c_{0c,surr\,1}) + \alpha_c(c_0 - c_{0,eq\,1})] \tag{6.6}$$

$$\rho_{eff}c_{p,eff}\left[\frac{\partial T}{\partial t}+\mathbf{v}.\nabla T\right] = -\frac{1}{t_{total}}\left[2h(T-T_{surr\ 1})+\bar{h}_{fg}\alpha_{coat}\left(c_{0c}-c_{0c,surr\ 1}\right)+\bar{q}_{st}\alpha_c\left(c_0-c_{0,eq\ 1}\right)\right] \tag{6.7}$$

As mentioned above, we have velocity components only in the x direction in our line, and this will likewise result in a molality and a temperature gradient only in the x direction. Hence, in our case

$$\begin{aligned}\mathbf{v}.\nabla m_{0c} &= v_x\frac{\partial m_{0c}}{\partial x}\\ \mathbf{v}.\nabla T &= v_x\frac{\partial T}{\partial x}\end{aligned} \tag{6.8}$$

When Equation 6.8 is then substituted in Equations 6.6 and 6.7, we get the governing equations in partial differential equation (PDE) form, on which the controller for zone one can be implemented

$$\frac{{\rho_0}^2\rho_s}{(\rho_0+M_0\rho_s m_{0c})^2}\left[\frac{\partial m_{0c}}{\partial t}+v_x\frac{\partial m_{0c}}{\partial x}\right] = -\frac{1}{t_{coating}}\left[\alpha_{coat}\left(c_{0c}-c_{0c,surr\ 1}\right)+\alpha_c\left(c_0-c_{0,eq\ 1}\right)\right] \tag{6.9}$$

$$\rho_{eff}c_{p,eff}\left[\frac{\partial T}{\partial t}+v_x\frac{\partial T}{\partial x}\right] = -\frac{1}{t_{total}}\left[2h(T-T_{surr\ 1})+\bar{h}_{fg}\alpha_{coat}\left(c_{0c}-c_{0c,surr\ 1}\right)+\bar{q}_{st}\alpha_c\left(c_0-c_{0,eq\ 1}\right)\right] \tag{6.10}$$

6.2.2 Implementing Method of Lines

The governing equations in the Eulerian framework are two partial differential equations, one for mass transfer (molality of the coating) and one for heat transfer (temperature). In order to be able to implement the Linear Quadratic Gaussian as the control strategy, it is necessary to have a system of ordinary differential equations that can then be linearized about a given point and converted into the state space form (Athans, 1971).

We can use the method of lines to convert the partial differential equations to a set of ordinary differential equations. Applying the method of lines involves construction of a numerical methods solution for the partial differential equations, in which all the spatial derivatives are discretized and the time variable is left continuous (Verwer and Sanz-Serna, 1984).

We use a finite difference method in which we divide our control volume into an equi-spaced grid, and then we used a first order backward difference for discretizing the spatial derivatives that are given by (Moin, 2010)

$$\begin{gathered}\left(\frac{dm_{0c_{x=i}}}{dx}\right) \approx \frac{m_{0c_{x=i}} - m_{0c_{x=i-1}}}{\Delta x_1} \\ \left(\frac{dT_{x=i}}{dx}\right) \approx \frac{T_{x=i} - T_{x=i-1}}{\Delta x_1}\end{gathered} \tag{6.11}$$

where the subscript $x = i$ and $x = i - 1$ represent the position on the grid, and $\Delta x_1 = l_1/n$ with l_1 being the grid length and n referring to the number of elements in the first drying zone. Figure 6.1 shows the finite difference grid for the piece of web in the first drying zone.

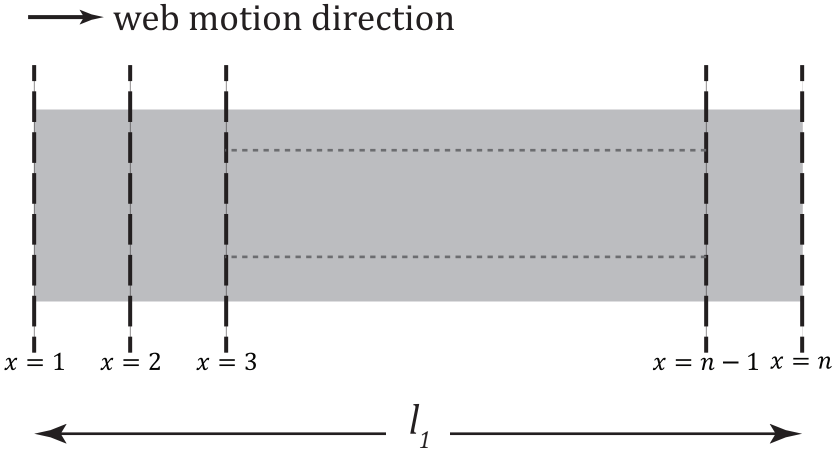

Figure 6.1: Finite difference grid applied to the web in the first drying zone

When method of lines is implemented in Equation 6.9 we get a system of ordinary differential equations for mass transfer

$$\begin{aligned}
&\frac{{\rho_0}^2\rho_s}{(\rho_0 + M_0\rho_s m_{0c})^2}\left[\frac{\partial m_{0c_{x=2}}}{\partial t} + v_x\frac{m_{0c_{x=2}} - m_{0c_{x=1}}}{\Delta x_1}\right] \\
&\qquad = -\frac{1}{t_{coating}}\left[\alpha_{coat}\left(c_{0c_{x=2}} - c_{0c,surr\,1}\right) + \alpha_c\left(c_0 - c_{0,eq\,1}\right)\right] \\
&\frac{{\rho_0}^2\rho_s}{(\rho_0 + M_0\rho_s m_{0c})^2}\left[\frac{\partial m_{0c_{x=3}}}{\partial t} + v_x\frac{m_{0c_{x=3}} - m_{0c_{x=2}}}{\Delta x_1}\right] \\
&\qquad = -\frac{1}{t_{coating}}\left[\alpha_{coat}\left(c_{0c_{x=3}} - c_{0c,surr\,1}\right) + \alpha_c\left(c_0 - c_{0,eq\,1}\right)\right] \\
&\frac{{\rho_0}^2\rho_s}{(\rho_0 + M_0\rho_s m_{0c})^2}\left[\frac{\partial m_{0c_{x=4}}}{\partial t} + v_x\frac{m_{0c_{x=4}} - m_{0c_{x=3}}}{\Delta x_1}\right] \\
&\qquad = -\frac{1}{t_{coating}}\left[\alpha_{coat}\left(c_{0c_{x=4}} - c_{0c,surr\,1}\right) + \alpha_c\left(c_0 - c_{0,eq\,1}\right)\right] \\
&\qquad\qquad\vdots \\
&\frac{{\rho_0}^2\rho_s}{(\rho_0 + M_0\rho_s m_{0c})^2}\left[\frac{\partial m_{0c_{x=n}}}{\partial t} + v_x\frac{m_{0c_{x=n}} - m_{0c_{x=n-1}}}{\Delta x_1}\right] \\
&\qquad = -\frac{1}{t_{coating}}\left[\alpha_{coat}\left(c_{0c_{x=n}} - c_{0c,surr\,1}\right) + \alpha_c\left(c_0 - c_{0,eq\,1}\right)\right]
\end{aligned} \tag{6.12}$$

And, when the method of lines is implemented in Equation 6.10, we get a system of ordinary differential equations for heat transfer

$$\rho_{eff}c_{p,eff}\left[\frac{\partial T_{x=2}}{\partial t}+v_x\frac{T_{x=2}-T_{x=1}}{\Delta x_1}\right] = -\frac{1}{t_{total}}\left[2h\left(T_{x=2}-T_{surr\,1}\right)+\bar{h}_{fg}\alpha_{coat}\left(c_{0c_{x=2}}-c_{0c,surr\,1}\right)+\bar{q}_{st}\alpha_c\left(c_0-c_{0,eq\,1}\right)\right]$$

$$\rho_{eff}c_{p,eff}\left[\frac{\partial T_{x=3}}{\partial t}+v_x\frac{T_{x=3}-T_{x=2}}{\Delta x_1}\right] = -\frac{1}{t_{total}}\left[2h\left(T_{x=3}-T_{surr\,1}\right)+\bar{h}_{fg}\alpha_{coat}\left(c_{0c_{x=3}}-c_{0c,surr\,1}\right)+\bar{q}_{st}\alpha_c\left(c_0-c_{0,eq\,1}\right)\right]$$

$$\rho_{eff}c_{p,eff}\left[\frac{\partial T_{x=4}}{\partial t}+v_x\frac{T_{x=4}-T_{x=3}}{\Delta x_1}\right] = -\frac{1}{t_{total}}\left[2h\left(T_{x=4}-T_{surr\,1}\right)+\bar{h}_{fg}\alpha_{coat}\left(c_{0c_{x=4}}-c_{0c,surr\,1}\right)+\bar{q}_{st}\alpha_c\left(c_0-c_{0,eq\,1}\right)\right]$$

$$\vdots$$

$$\rho_{eff}c_{p,eff}\left[\frac{\partial T_{x=n}}{\partial t}+v_x\frac{T_{x=n}-T_{x=n-1}}{\Delta x_1}\right] = -\frac{1}{t_{total}}\left[2h\left(T_{x=n}-T_{surr\,1}\right)+\bar{h}_{fg}\alpha_{coat}\left(c_{0c_{x=n}}-c_{0c,surr\,1}\right)+\bar{q}_{st}\alpha_c\left(c_0-c_{0,eq\,1}\right)\right] \tag{6.13}$$

Equations 6.12 and 6.13 are the discretized ordinary differential equations that describe the molality of the water and the coating temperature of the membrane-coating assembly at the grid points. It should be noted that they are coupled and are solved together in the process of implementing the controller.

In the above equations, the values of $m_{0c_{x=1}}$ and $T_{x=1}$ are necessary to solve the equations. They are the conditions of the membrane-coating assembly at the first zone's entry and these are known because we have knowledge of the ink's composition and pre-swelled membrane's temperature.

6.2.3 Modeling Machine Actuators

By changing $c_{0c,surr\,1}$, $c_{0,eq\,1}$, and $T_{surr\,1}$ in Equations 6.12 and 6.13, we can change the evolution of the various molalities and temperatures. This can be achieved by changing the temperature, $T_{surr\,1}$, and water activity, $a_{0,surr\,1}$ of the drying zone as discussed in the preceding chapters.

Unfortunately, $T_{surr\,1}$ and $a_{0,surr\,1}$ cannot be changed instantaneously, because of their relatively slower response. As explained in the previous chapter, PID controllers, which are embedded in LabView™ , are used to control the heaters and the humidifiers that affect the drying zone. However, we can instantaneously change the set points of the PID controller, which can be used as the line's inputs in our Linear Quadratic Gaussian design.

Because there will be a time lapse or lag between a change in the PID set points and the actual change in zone temperature, it is necessary to model the relationship between the set point temperature and the actual temperature in zone.

We start by assuming a first-order response for the drying zone's temperature and water activity for a change in the respective set points. The response of zone one is assumed to be of the form

$$\frac{da_{0,surr\,1}}{dt} = -\alpha_{\star 1}(a_{0,surr\,1} - a_{0,setpt\,1})$$

$$\frac{dT_{surr\,1}}{dt} = -h_{\star 1}(T_{surr\,1} - T_{setpt\,1}) \tag{6.14}$$

where $\alpha_{\star 1}$ and $h_{\star 1}$ represent the mass and heat transfer barriers for the first drying zone and are obtained by matching them to fit actual experiments. The zone's water activity and temperature set points are given by $a_{0,setpt\,1}$ and $T_{setpt\,1}$.

In Equation 6.14, we note that the overshoot caused by the PID controller is ignored and as the LQG is designed to control the system for small deviations from the nominal state values, hence the exponential structure in Equation 6.14 was chosen.

6.2.4 Summary of Equations Used in Control

Equations 6.12, 6.13, and 6.14 were used to develop the model-based regulator and estimator for zone one, these equations are coupled, and $T_{surr\,1}$ along with $a_{0,surr\,1}$ are the physical conditions that we can change externally or control in the given zone. We identify the state variables, inputs, and outputs for the zone later in Section 6.4.

6.3 EQUATIONS FOR MODEL BASED CONTROL (ZONE 2)

Following the procedure outlined in Section 6.2, we can then also derive all the equations necessary to implement control for the second zone. Recalling that in zone two, we track the molality of water in the membrane along with the temperature of the entire membrane-coating assembly. We begin with Equations 3.14 and 3.16, followed by conversion from the Lagrangian to the Eulerian reference frame and then again implement the method of lines, thus we obtain

$$\frac{{\rho_0}^2\rho_m}{(\rho_0+M_0\rho_m m_0)^2}\left[\frac{\partial {m_0}_{x=n+1}}{\partial t}+v_x\frac{{m_0}_{x=n+1}-{m_0}_{x=n}}{\Delta x_2}\right]$$

$$=-\frac{1}{t_{membrane}}\left[F\alpha_c\left({c_0}_{x=n+1}-c_{0,eq\,2}\right)+\alpha_c\left({c_0}_{x=n+1}-c_{0,eq\,2}\right)\right]$$

$$\frac{{\rho_0}^2\rho_m}{(\rho_0+M_0\rho_m m_0)^2}\left[\frac{\partial {m_0}_{x=n+2}}{\partial t}+v_x\frac{{m_0}_{x=n+2}-{m_0}_{x=n+1}}{\Delta x_2}\right]$$

$$=-\frac{1}{t_{membrane}}\left[F\alpha_c\left({c_0}_{x=n+2}-c_{0,eq\,2}\right)+\alpha_c\left({c_0}_{x=n+2}-c_{0,eq\,2}\right)\right]$$

$$\frac{{\rho_0}^2\rho_m}{(\rho_0+M_0\rho_m m_0)^2}\left[\frac{\partial {m_0}_{x=n+3}}{\partial t}+v_x\frac{{m_0}_{x=n+3}-{m_0}_{x=n+2}}{\Delta x_2}\right]$$

$$=-\frac{1}{t_{membrane}}\left[F\alpha_c\left({c_0}_{x=n+3}-c_{0,eq\,2}\right)+\alpha_c\left({c_0}_{x=n+3}-c_{0,eq\,2}\right)\right]$$

$$\vdots$$

$$\frac{{\rho_0}^2\rho_m}{(\rho_0+M_0\rho_m m_0)^2}\left[\frac{\partial {m_0}_{x=n+m}}{\partial t}+v_x\frac{{m_0}_{x=n+m}-{m_0}_{x=n+m-1}}{\Delta x_2}\right]$$

$$=-\frac{1}{t_{membrane}}\left[F\alpha_c\left({c_0}_{x=n+m}-c_{0,eq\,2}\right)+\alpha_c\left({c_0}_{x=n+m}-c_{0,eq\,2}\right)\right]$$

(6.15)

$$\rho_{eff}c_{p,eff}\left[\frac{\partial T_{x=n+1}}{\partial t}+v_x\frac{T_{x=n+1}-T_{x=n}}{\Delta x_2}\right]$$
$$=-\frac{1}{t_{total}}[2h(T_{x=n+1}-T_{surr\ 2})+F\bar{q}_{st}\alpha_c\left(c_{0_{x=n+1}}-c_{0,eq\ 2}\right)$$
$$+\bar{q}_{st}\alpha_c\left(c_{0_{x=n+1}}-c_{0,eq\ 2}\right)]$$
$$\rho_{eff}c_{p,eff}\left[\frac{\partial T_{x=n+2}}{\partial t}+v_x\frac{T_{x=n+2}-T_{x=n+1}}{\Delta x_2}\right]$$
$$=-\frac{1}{t_{total}}[2h(T_{x=n+2}-T_{surr\ 2})+F\bar{q}_{st}\left(c_{0_{x=n+2}}-c_{0,eq\ 2}\right)+\bar{q}_{st}\alpha_c\left(c_{0_{x=n+2}}-c_{0,eq\ 2}\right)]$$
$$\rho_{eff}c_{p,eff}\left[\frac{\partial T_{x=n+3}}{\partial t}+v_x\frac{T_{x=n+3}-T_{x=n+2}}{\Delta x_2}\right]$$
$$=-\frac{1}{t_{total}}[2h(T_{x=n+3}-T_{surr\ 2})+F\bar{q}_{st}\left(c_{0_{x=n+3}}-c_{0,eq\ 2}\right)+\bar{q}_{st}\alpha_c\left(c_{0_{x=n+3}}-c_{0,eq\ 2}\right)]$$
$$\vdots$$
$$\rho_{eff}c_{p,eff}\left[\frac{\partial T_{x=n+m}}{\partial t}+v_x\frac{T_{x=n+m}-T_{x=n+m-1}}{\Delta x_2}\right]$$
$$=-\frac{1}{t_{total}}[2h(T_{x=n+m}-T_{surr\ 2})+F\bar{q}_{st}\left(c_{0_{x=n+m}}-c_{0,eq\ 2}\right)$$
$$+\bar{q}_{st}\alpha_c\left(c_{0_{x=n+m}}-c_{0,eq\ 2}\right)] \qquad (6.16)$$

where, the subscript ‘2’ refers to the quantities corresponding to the second zone. The numbering of the finite element grid for this second zone two now begins at $x = n + 1$ and ends at $x = n + m$. This numbering is continued from the first zone where at the first drying zone’s last grid point, $x = n$. Making $\Delta x_2 = l_2/m$, where l_2 is the length and m is the number of elements in the second drying zone. Details of the second zone’s grid numbering are showed in Figure 6.2.

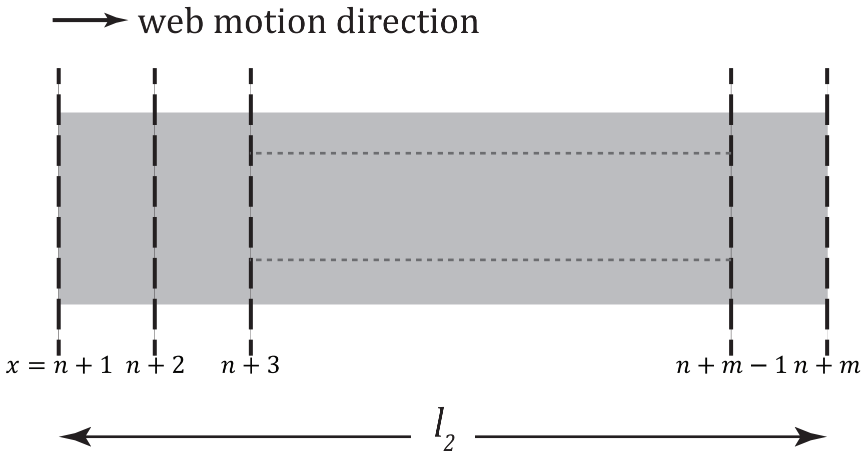

Figure 6.2: Implemented finite difference grid of the second zone

The starting value of $T_{x=n}$, which is the temperature at which the membrane-coating assembly enters the second drying zone, is necessary to solve Equation 6.16 and it is obtained from the solution of the equations of the previous drying zone. To calculate a value for $m_{0_{x=n}}$, the membrane is assumed to still be saturated with water, by being at the grid point where the last of the liquid water is removed from the coating.

The web velocity v_x remains the consistent in both the first and the second drying zones since the membrane web is continuous and moves with a uniform velocity throughout the pilot-scale coating line.

Again, like for the first zone, the dynamics of the drying zone's actuators need to be modeled, which we do again as explained in Section 6.2.3, and this gives us

$$\begin{aligned} \frac{da_{0,surr\,2}}{dt} &= -\alpha_{\star 2}(a_{0,surr\,2} - a_{0,setpt\,2}) \\ \frac{dT_{surr\,2}}{dt} &= -h_{\star 2}(T_{surr\,2} - T_{setpt\,2}) \end{aligned} \tag{6.17}$$

in which, $T_{setpt\,2}$ and $a_{0,setpt\,2}$ refer to the PID controller's set points of the second drying zone. $\alpha_{\star 2}$ and $h_{\star 2}$ are experimentally determined fitting constants analogous to $\alpha_{\star 2}$ and $h_{\star 1}$ from above.

Using Equations 6.15, 6.16, and 6.17, we can now develop the model-based controller and the estimator for the second drying zone.

6.4 NOMINAL OPERATING CONDITIONS AND LINEARIZATION

In this and the forthcoming sections, the details of the development of the model-based controller for the second zone are not discussed, as it would be repetitive since the procedure is identical to the first drying zone's LQG design, which we have discussed in detail above. Equations 6.15, 6.16 and 6.17 are thus used to design the controller, with the additional constraint that the conditions in this second zone need to avoid operation at conditions that create wrinkling as determined previously in Chapter 4.

Wolfram Mathematica™ was used to develop, test and simulate the linear model, the LQR, the Kalman Filter and the LQG.

6.4.1 Defining State Variables, Inputs, Measurements

In order to successfully implement model-based stochastic control it is necessary to identify the state variables that will constitute the state vector. It is also necessary to define the inputs and measurements. These state variables, inputs and measurement are tabulated in Table 6.1 for zone one.

Table 6.1: State variables, inputs and measurements for the first drying zone

State variables	Inputs	Measurements
${m_{0c}}_{x=2}$	$a_{0,setpt\ 1}$	${m_{0c}}_{x=n}$
${m_{0c}}_{x=3}$	$T_{setpt\ 1}$	$T_{x=n}$
$\vdots$		$a_{0,surr\ 1}$
${m_{0c}}_{x=n}$		$T_{surr\ 1}$
$T_{x=2}$		
$T_{x=3}$		
$\vdots$		
$T_{x=n}$		
$a_{0,surr\ 1}$		
$T_{surr\ 1}$		

Although we can control the web velocity v_x, in order to minimize the material expense due to Nafion being very expensive, we choose to use a fixed velocity of 0.002 m/s, which is the minimum operating velocity of the pilot-scale line.

A 1200 Series laser displacement sensor from Laser-View Technologies (Laser-View, 2012) was used to measure t_{total} at the end of the first drying zone since we could not directly measure the molality of water in the coating. Using Equation 3.13, this t_{total} is then converted to ${m_{0c}}_{x=n}$. An infrared thermocouple type-T purchased from Omega (Omega, 2012) is used to measure $T_{x=n}$. The SHT15 digital temperature and humidity sensor, as mentioned in Chapter 5, is used to measure the zone's water activity $a_{0,surr\ 1}$, and temperature $T_{surr\ 1}$.

A table describing the state variables, inputs and measurements for the second drying zone was constructed as for the first zone; again for brevity that table is not repeated here.

6.4.2 Steady-State Nominal Operating Conditions

Before linearizing the system and obtaining the state space representation that are required to implement control, we needed to develop nominal expected values for the state variables during operating conditions. This is done by propagating the plant's non-linear Equations 6.12, 6.13 and 6.14 in time for a set of fixed inputs. Essentially, we are solving for the equilibrium values of the state variables at a given set of input values, while making sure that the obtained equilibrium operating conditions meet the desired goal of the process.

In the first drying zone, the nominal operating conditions were chosen such that the water molality of the coating at the exit of the first zone, $m_{0c_{x=n}}$ is just above zero. In theory, letting $m_{0c_{x=n}}$ equal to zero may be possible for many input combinations, however, we needed to limit our choice of nominal inputs to those actually possible within the capabilities of the coating line.

The coating was applied with the doctor blade and had an applied wetting thickness of 50 microns. We chose $l_1 = 0.62$ meters for the drying length. And for $a_{0,setpt\ 1} = 0.45$ and $T_{setpt\ 1} = 323$ Kelvin, the molality profile that was obtained is plotted in Figure 6.3. This was calculated with $n = 20$ elements and it should be noted that $m_{0c_{x=20}}$ is almost zero.

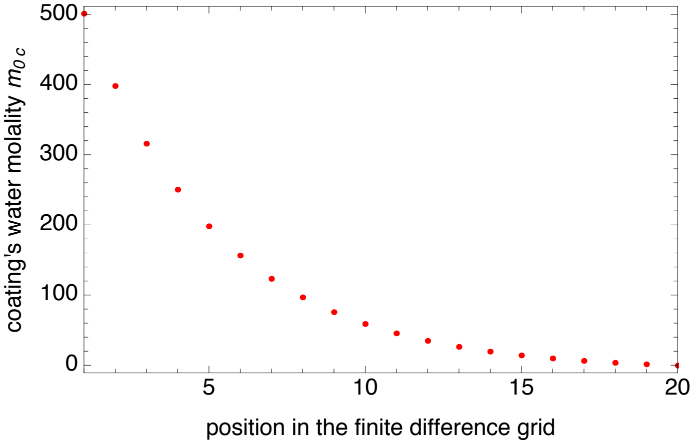

Figure 6.3: The nominal evolution of coating's water molality in the first drying zone

Similarly, Figure 6.4 shows the membrane-coating assembly's temperature at the corresponding grid points in drying zone one.

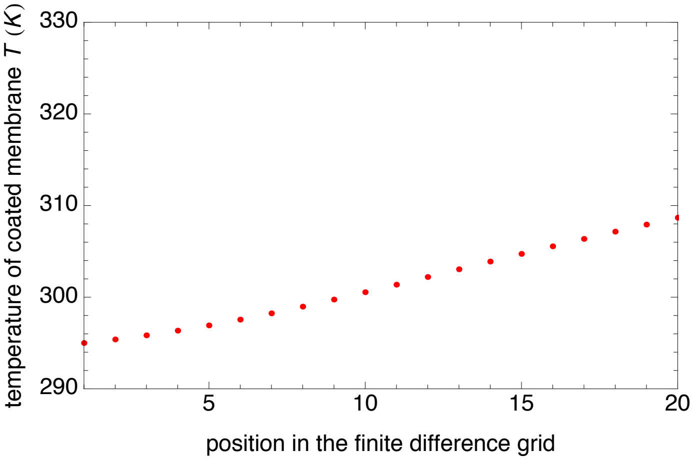

Figure 6.4: The nominal evolution of coated membrane's temperature in the first drying zone

6.4.3 State Space Linearization

As stated before, the governing equations for both zones are continuous-time ordinary differential equations. In Chapter 5 we discussed the design of the drying zone, in which the heater and humidifier are controlled with a PID loop which is implemented using LabView. This control was implemented inside of a LabView's while loop and thus adjustment is not continuous but the on/off signals to the heaters and humidifiers are updated at given time intervals. Since the PID control is not continuous, a discrete time regulator is best suited for this scenario.

To develop a discrete time stochastic controller, one must linearize the system of ordinary differential equations and express it in discrete state space form.

The governing ordinary differential equations expressed in Equations 6.12, 6.13 and 6.14 are of the form

$$\dot{\mathbf{x}} = \mathrm{f}(\mathbf{x}, \mathbf{u}) \tag{6.18}$$

where **x** is the state vector and **u** is the input vector. The state and input vectors are

$$\mathbf{x} = \begin{bmatrix} m_{0c_{x=2}} \\ \vdots \\ m_{0c_{x=20}} \\ T_{x=2} \\ \vdots \\ T_{x=20} \\ a_{0,surr\,1} \\ T_{surr\,1} \end{bmatrix} \tag{6.19}$$

$$\mathbf{u} = \begin{bmatrix} a_{0,setpt\,1} \\ T_{setpt\,1} \end{bmatrix} \tag{6.20}$$

A discrete Taylor linearization (Franklin *et al*, 1988) when performed on the governing equations around the nominal state variable values and inputs, yield a set of linear, time-invariant, discrete-time state equations of the form

$$\mathbf{x(k+1) = Ax(k) + Bu(k)} \tag{6.21}$$

in which the plant matrix **A** has dimensions of 40 x 40 and **B** has dimensions of 40 x 2. It reflects the spatial relationship and a weak coupling between the states. Index **k** notates time. Since we are not interested in all the states, the measurement equation is

$$\mathbf{y(k) = Cx(k)} \tag{6.22}$$

the measurement matrix $\mathbf{C}$ is chosen to reflect a realistic number and placement of sensors that can directly measure the molality, temperature and water activity states

$$\mathbf{y} = \begin{bmatrix} m_{0c_{x=20}} \\ T_{x=20} \\ a_{0,surr\ 1} \\ T_{surr\ 1} \end{bmatrix} \tag{6.23}$$

During a scale up industrial implementation of this approach, more sensors can be added to improve accuracy. It should be noted that laser thickness measurement sensors have been historically more expensive when compared to thermocouple-based temperature sensors. Considering practicality and cost, it is possible to design a system using more inexpensive temperature measurements and less of the more expensive thickness measurements as an indirect method of measuring the molality.

Equations 6.21 and 6.22, together are known as the discrete-time state space model, and are used in the implementation of the model-based controller.

6.5 DESIGN OF THE LINEAR QUADRATIC REGULATOR

The control objective is to keep the system's operating conditions as near as possible to the nominal equilibrium state values as shown in Figures 6.3 and 6.4. This objective makes this a regulation problem and we assume the coating line to exhibit linear behavior around the neighborhood of the operating point. These factors make the LQR an appropriate choice for the controller (Kwakernaak and Sivan, 1972). Implementing an optimal controller like the LQR has an additional advantage in that the controller can be tuned by minimizing a physically meaningful cost function rather than by directly selecting gains.

Figure 6.5 is a block diagram showing the relationship between the LQR and the pilot-scale coating line that is represented by Equations 6.21 and 6.22. Although in the figure, the process and measurement noises, $\mathbf{w}$ and $\mathbf{v}$, are denoted, it has been neglected in the development of the LQR. However, these noise terms are important for the development of the estimator, and are discussed in detail in Section 6.6.

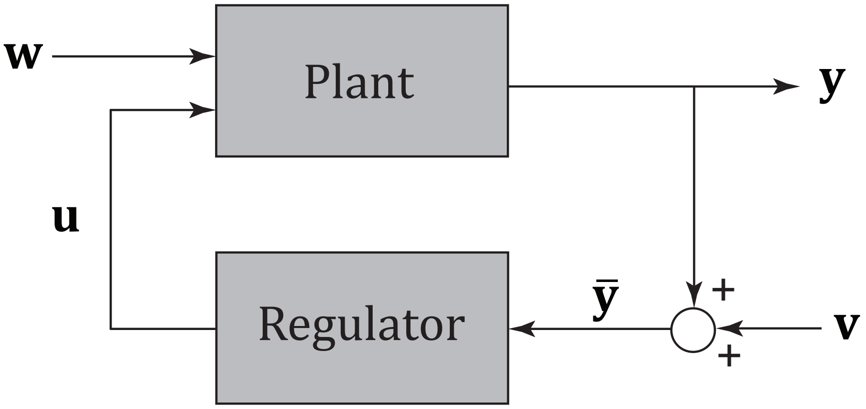

Figure 6.5: Block diagram showing the relationship between the plant and the LQR

6.5.1 Controllability

Since we are interested in controlling the molality of the water in the coating at the exit point of the first drying zone, it is necessary to control the output $\mathbf{y}$ in the measurement Equation 6.22. To successfully accomplish this, the system of discrete-time state space equations must be output controllable.

A state-space model is considered to be output controllable if for any initial time and any initial state, there exists some control input that drives the output to any desired final value in finite time (Ogata, 1997).

A system is said to be output controllable if the output controllability matrix has a full row rank. This is also known as Kalman's criteria of controllability (Ogata, 1997) and the matrix defining this criteria is given by

$$[\mathbf{CB} \quad \mathbf{CAB} \quad \mathbf{CA}^2\mathbf{B} \quad \cdots \quad \mathbf{CA}^{p-1}\mathbf{B}] \tag{6.24}$$

with $p = 40$ since in our case $\mathbf{A}$ is a 40 x 40 matrix. It should be noted by this criteria that our system is output controllable.

6.5.2 Design Process

The cost minimization function that we used is notated by $\mathbf{J}$ and is expressed as (Kwakernaak and Sivan, 1972)

$$\mathbf{J} = \sum_{\mathbf{k}=\mathbf{1}}^{\infty} [\mathbf{y}^{\mathrm{T}}(\mathbf{k})\mathbf{Q}_r\mathbf{y}(\mathbf{k}) \ + \mathbf{u}^{\mathrm{T}}(\mathbf{k})\mathbf{R}_r\mathbf{u}(\mathbf{k})] \tag{6.25}$$

The input that minimizes $\mathbf{J}$ is the state feedback input given by

$$\mathbf{u}(\mathbf{k}) = -\mathbf{K}_r\mathbf{x}(\mathbf{k}) \tag{6.26}$$

in which $\mathbf{K}_r$ is the gain matrix. Since the upper limit in the summation of the cost function shown in Equation 6.25 goes to $\mathbf{k} = \infty$, it is an infinite horizon LQR and $\mathbf{K}_r$ can be computed offline.

The gain matrix $\mathbf{K}_r$ is calculated using

$$\mathbf{K}_r = (\mathbf{R}_r + \mathbf{B}^{\mathrm{T}}\mathbf{P}_r\mathbf{B})^{-1}\mathbf{B}^{\mathrm{T}}\mathbf{P}_r\mathbf{A} \tag{6.27}$$

in which matrix $\mathbf{P}_r$ is the solution to the discrete-time algebraic Ricatti equation

$$\mathbf{P}_r = \mathbf{Q}_r + \mathbf{A}^{\mathrm{T}}[\mathbf{P}_r - \mathbf{P}_r\mathbf{B}(\mathbf{R}_r + \mathbf{B}^{\mathrm{T}}\mathbf{P}_r\mathbf{B})^{-\mathbf{1}}\mathbf{B}^{\mathrm{T}}\mathbf{P}_r] \tag{6.28}$$

The output-weighting matrix $\mathbf{Q}_r$ in Equation 6.25 is defined as a diagonal matrix, in which each of the diagonal elements is the inverse of the variance of the particular output it represents.

The input-weighting matrix is also defined diagonally and represents the maximum permissible change in input between subsequent iterations. It should be noted that if the optimal inputs computed by the LQR falls outside the plant's capability, we saturate the inputs.

6.5.3 Simulation of the LQR

We simulated the LQR assuming full state feedback to check its performance. For the simulation results that are shown in Figure 6.6 and 6.7, a small perturbation from the nominal operating conditions were considered at the start of the simulation to study the performance of the regulator. Figure 6.6 shows the simulated LQR performance for the outputs $m_{0c_{x=20}}$ and $T_{x=20}$ vs time when the initial temperature at the exit of the first zone at the start of the simulation was below the nominal value and the corresponding coating's water molality above the nominal value. Figure 6.7 shows the computed optimal inputs vs time for this simulation.

It can be seen from Figure 6.6 that the controller was able to return the perturbed outputs to the nominal operating conditions in about 400 seconds.

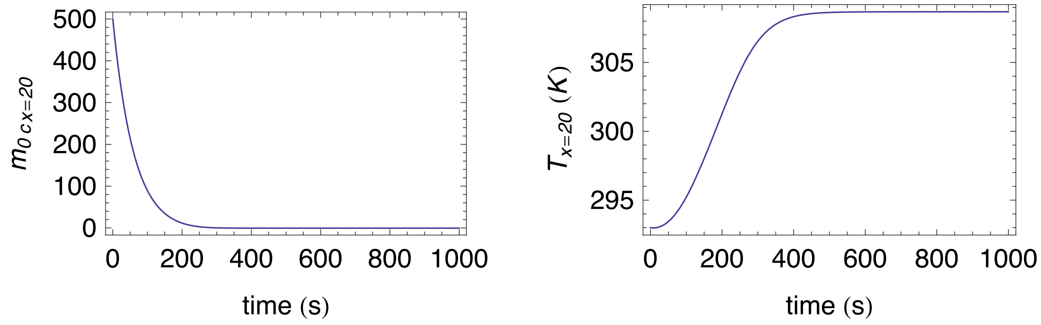

Figure 6.6: Simulated LQR performance indicating water molality and temperature at exit with above nominal initial water molality conditions at the start of the simulation

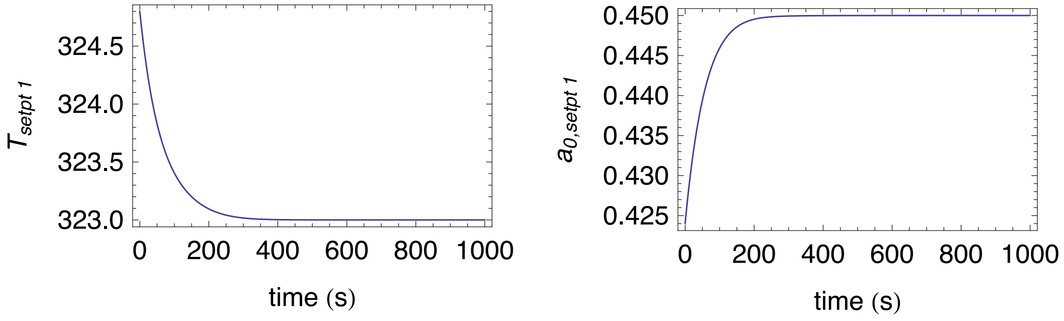

Figure 6.7: Computed LQR inputs for simulation with above nominal initial water molality conditions

The LQR controller was also simulated with a different initial perturbation, in which temperature at the exit was above its nominal condition and these results are shown in Figure 6.8.

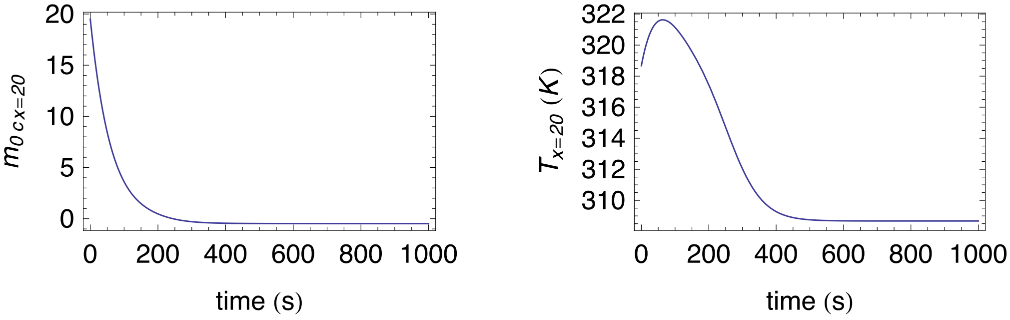

Figure 6.8: Simulated LQR performance for water molality and temperature at exit with above nominal initial temperature conditions

The inputs computed by the LQR for the same are shown in Figure 6.9.

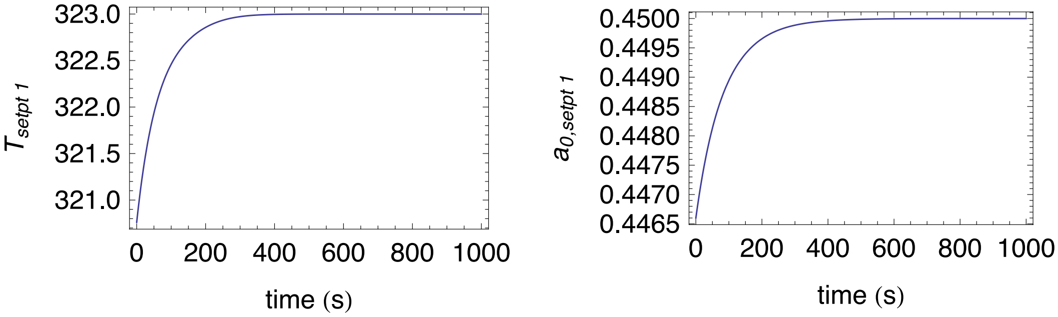

Figure 6.9: Computed LQR inputs for simulation with above nominal initial temperature conditions

By observing the scenarios simulated above, we can demonstrate that we have developed a model-based discrete controller that is capable of controlling our system when perturbations alter the outputs either above or below the nominal operating conditions.

6.6 DESIGN OF THE KALMAN FILTER

The LQR discussed in Section 6.5 computes the control input, based on the assumption that we have complete knowledge of the plant's state variables. As stated before, it is not possible to measure all the state variables and mounting twenty thickness and temperature sensors within a distance of 0.6 meters in coating line in not reasonable. We can however measure the thickness and temperature of the membrane-coating assembly at the exit of first drying zone. However, these measurements can be corrupted by noise arising from several sources that include vibration of the machine and the membrane, electrical noise from the sensors and optical noise from the laser displacement sensor. Hence, an estimator is needed to estimate the plant's true state from these incomplete noisy measurements.

We have chosen to use a discrete-time Kalman filter, commonly abbreviated as a DKF, which "blends" the predictions from the model and the actual measurements to estimate the values of the state variables that are denoted by $\hat{\mathbf{x}}$ in this work. The block diagram of a typical Kalman estimator is shown in Figure 6.10 in which $\mathbf{u}$ is the input vector, $\bar{\mathbf{y}}$ is the measurement vector that is obtained from the system's output sensors and $\hat{\mathbf{x}}$ is the estimated state vector.

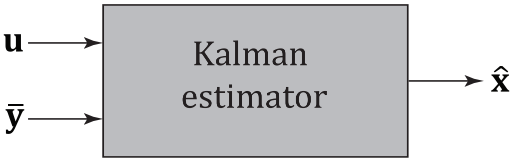

Figure 6.10: The block diagram representation of the Kalman Filter

6.6.1 Observability

Since the design of the LQR assumes full state feedback, it is important to make sure that the estimator can estimate the values of all the states using the measured states designated by the output vector $\mathbf{y}$. Observability is the measure of how well the internal states of a system can be inferred by knowledge of its external outputs (Ogata, 1997).

A system is said to be observable if the observability matrix $\mathbf{O}$ of a system has full row rank (Ogata, 1997), and is designated by

$$\mathbf{O} = \begin{bmatrix} \mathbf{C} \\ \mathbf{CA} \\ \mathbf{CA}^2 \\ \vdots \\ \mathbf{CA}^{p-1} \end{bmatrix} \tag{6.29}$$

The observability matrix for our system has full row rank and hence the values of its states can be estimated by measuring the output vector $\mathbf{y}$.

6.6.2 Design Process

The discrete-time state space model expressed in Equations 6.21 and 6.22 neglects any process and measurement noise arising from a number of sources as mentioned before. The process and measurement noises are denoted by $\mathbf{w}$ and $\mathbf{v}$ respectively, and are assumed to be zero-mean Gaussian in nature. The already expressed discrete-time state space system can be modified to (Kwakernaak and Sivan, 1972)

$$\mathbf{x}(\mathbf{k}+\mathbf{1}) = \mathbf{Ax}(\mathbf{k}) + \mathbf{Bu}(\mathbf{k}) + \mathbf{w}(\mathbf{k}) \tag{6.30}$$

$$\mathbf{y}(\mathbf{k}) = \mathbf{Cx}(\mathbf{k}) + \mathbf{v}(\mathbf{k}) \tag{6.31}$$

It should be noted that the noise $\mathbf{w}$ and $\mathbf{v}$ are uncorrelated with each other in the time domain as they have different sources. The properties of the process and state noise are given by

$$\begin{aligned} E[\mathbf{w}(\mathbf{k})\mathbf{w}(\mathbf{k}+g)^{\mathrm{T}}] &= \begin{cases} \mathbf{Q}_K & g = 0 \\ 0 & g \neq 0 \end{cases} \\ E[\mathbf{v}(\mathbf{k})\mathbf{v}(\mathbf{k}+g)^{\mathrm{T}}] &= \begin{cases} \mathbf{R}_K & g = 0 \\ 0 & g \neq 0 \end{cases} \end{aligned} \tag{6.32}$$

for all time $\mathbf{k}$. $\mathbf{Q}_K$ and $\mathbf{R}_K$ are known as the state and measurement covariance matrices, respectively.

The estimate of the state $\mathbf{x(k)}$ using all measurements available up to time $\mathbf{k-1}$ is

$$\mathbf{\hat{x}(k|k-1) = Ax(k-1|k-1) + Bu(k)} \tag{6.33}$$

When the new measurement at $\mathbf{\bar{y}(k)}$ becomes available, the state estimate is updated by

$$\mathbf{\hat{x}(k|k) = \hat{x}(k|k-1) + K}_K\mathbf{[\bar{y}(k) - C\hat{x}(k|k-1)]} \tag{6.34}$$

in which $\mathbf{K}_K$, which is commonly referred to as the Kalman gain is defined as

$$\mathbf{K}_K = \mathbf{P}_K\mathbf{(k|k-1)C}^{\mathrm{T}}[\mathbf{CP}_K\mathbf{(k|k-1)C}^{\mathrm{T}} + \mathbf{R}_K]^{-\mathbf{1}} \tag{6.35}$$

If the Kalman gain is computed and updated for every iteration, it is known as an optimal Kalman filter. However, our system is considered observable, hence the Kalman gains converge and reach a "steady-state" value. In our design, we implement the Kalman filter with these steady-state Kalman gains, and this is known as the sub-optimal Kalman filter (Maybeck, 1982). It should be noted that in our estimator design, the Kalman gain matrix $\mathbf{K}_K$ is constant and is computed ahead of time.

In Equations 6.35, the covariance of the updated measurement $\mathbf{P}_K\mathbf{(k|k-1)}$ is obtained from

$$\mathbf{P}_K\mathbf{(k|k)} = [\mathbf{I} - \mathbf{K}_K\mathbf{C}]\mathbf{P}_K\mathbf{(k|k-1)}[\mathbf{I} - \mathbf{K}_K\mathbf{C}]^{\mathrm{T}} + \mathbf{K}_K\mathbf{R}_K\mathbf{K}_K \tag{6.36}$$

and

$$\mathbf{P}_K\mathbf{(k|k-1)} = \mathbf{AP}_K\mathbf{(k-1|k-1)A}^{\mathrm{T}} + \mathbf{Q}_K \tag{6.36}$$

To successfully design and implement a discrete-time Kalman filter it is necessary to have knowledge of the state and measurement covariance matrices $\mathbf{Q}_K$ and $\mathbf{R}_K$. The state can be corrupted with noise from either uneven material properties or sudden random changes in machine conditions like vibrations or other noise that might arise due to disturbances in the inputs. Since, there is no real data published for our pilot-scale coating line, we set $\mathbf{Q}_K$ to a diagonal matrix with its elements at 95% confidence intervals for the corresponding inputs.

The diagonal values of measurement covariance matrix $\mathbf{R}_K$ are also set to a 95% confidence interval for the corresponding measurements, which is reasonable according to the sensors manufacturers' specification sheets.

The Kalman filter's design procedure followed above is explained in detail by Athans (1971) and Maybeck (1979).

6.6.3 Simulation of the Estimator

To test if the Kalman estimator that we developed is a suitable substitute for the impossible task of directly measuring every state variable, we ran some simulations. We artificially injected noise into the plant and measurement expressions, and propagated Equations 6.30 and 6.31 for a particular set of inputs. This was later compared to the estimates available from Equation 6.34. The comparison for the exit conditions $m_{0c_{x=20}}$ and $T_{x=20}$ along with the mid point conditions $m_{0c_{x=10}}$ and $T_{x=10}$ are shown in Figures 6.11 and 6.12. The values used to initialize the estimation vector $\hat{\mathbf{x}}(\mathbf{k}=\mathbf{0})$ were deviated from the initial value of the state vector $\mathbf{x}(\mathbf{k}=\mathbf{0})$, to check the ability of the filter to accurately track the state variables.

In Figures 6.11 and 6.12, the blue trace is the state estimate and the red trace is the actual state's value obtained from simulation.

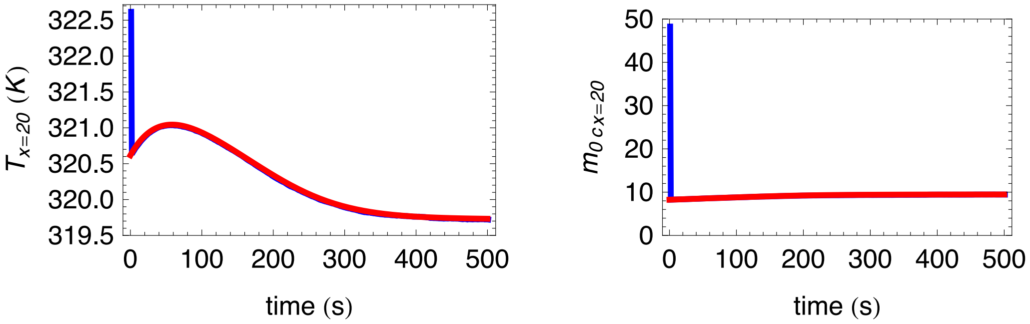

Figure 6.11: Evolution of state variables (red) and estimate (blue) at the first drying zone's exit (grid location $x = 20$)

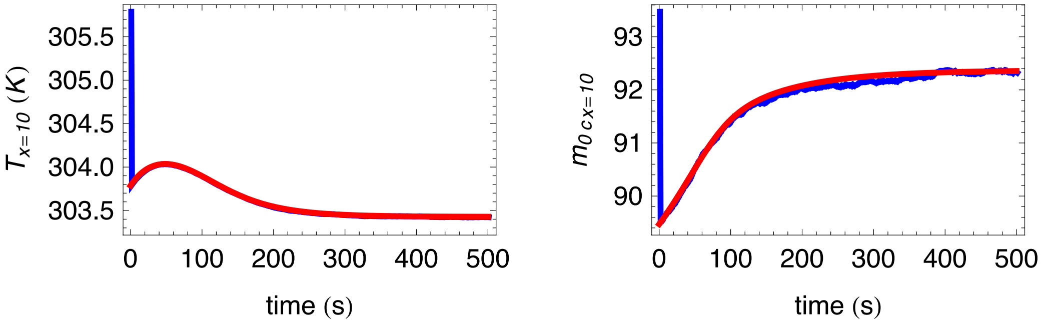

Figure 6.12: Evolution of state variables (red) and estimate (blue) at the first drying zone's mid point (grid location $x = 10$)

From Figures 6.11 and 6.12 it can be noted that the estimates closely follow the actual state variable values obtained from simulation within a few iterations indicating good estimation capabilities.

6.7 IMPLEMENTING AND TESTING THE LQG ON THE MACHINE

6.7.1 Implementation

In Sections 6.5 an LQR that is capable of regulating the system at the nominal operating values was developed. As mentioned before, it is impractical to measure every single state variable; hence we use a Kalman filter to estimate the state variables by measuring the outputs as developed in Section 6.6.

Linear Quadratic Gaussian control is a type of optimal control where all the state variables of the plant are unavailable for measurement and or use as feedback. Moreover, the plant or process undergoing control is subject to a quadratic cost function (Athans, 1971). An LQR used for control or regulation, used in conjunction with a Kalman filter is commonly known as an LQG.

The interaction between the LQG and the plant is shown in Figure 6.13.

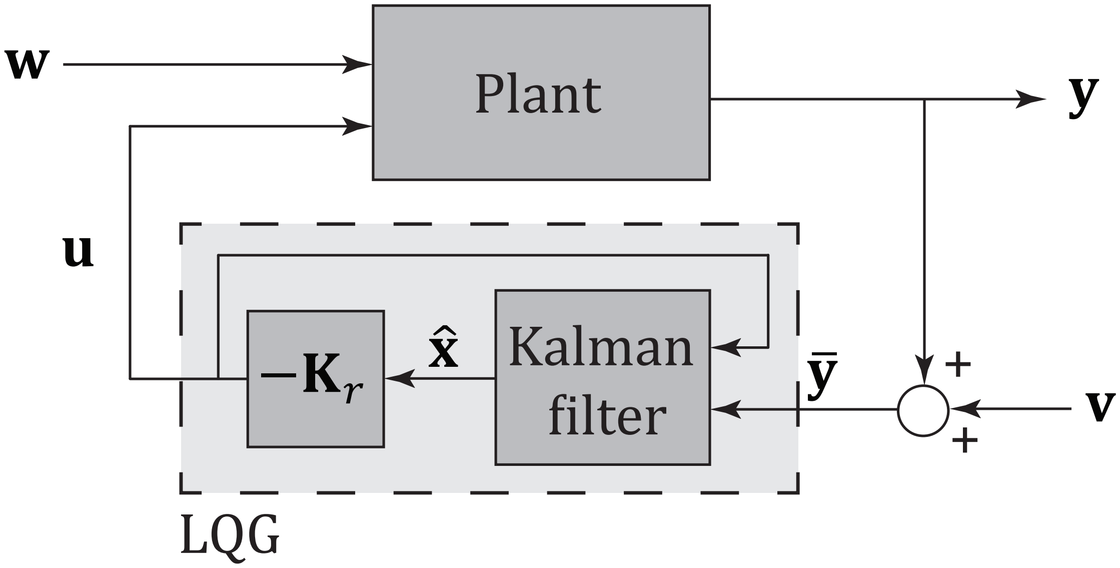

Figure 6.13: A block diagram of an LQG showing its interaction with the plant

As mentioned before we used Wolfram Mathematica to compute and develop matrices $\mathbf{A}$, $\mathbf{B}$, $\mathbf{C}$, $\mathbf{D}$, $\mathbf{K}_r$, and $\mathbf{K}_K$. We also used Mathematica to perform the various simulations and then to compare results. However, the inputs to the pilot-scale coating line have to be routed through the PID controllers in LabView™ since we interact with the pilot-scale coating line through the DAQ. Therefore the LQG was implemented with the help of a MathScript™ node in LabView™ and was updated at the correct interval using a timed while loop inside LabView™.

6.7.2 Testing

We tested the performance of the LQG by using it for control and estimation in our pilot-scale coating machine by coating and drying long pieces of Nafion at the conditions discussed throughout this dissertation and were able to produce wrinkle-free coated PEMs. These tests concured with our hypothesis and verified that the continuous membrane coating process does benefit from a model-based controller.

In Figure 6.14, the photograph on the right is of coated Nafion with the LQG controlling the drying during fabrication in zones 1 and 2. The image on the left was coated without the use of pre-swelling, two-staged drying or control. The wrinkles, and other related coating defects can be clearly seen. The effectiveness of pre-swelling, two-staged drying and model-based control can be seen by comparing the two strips of Nafion side-by-side.

Figure 6.14: Photograph showing non-ideal coating of Nafion (left) next to drying controlled by a model-based LQG

6.8 CONCLUSION

The models that were developed in the previous chapters for the drying of the saturated, coated membrane are in a Lagrangian reference frame and neglect the movement of the web through the drying zone. It is essential to convert this model into an Eulerian reference frame and implement method of lines to make these equations control friendly. These equations were later linearized and converted to a discrete-time state space form. The LQR and Kalman filter were developed using this state space model; and by simulating and studying their performance at multiple scenarios, their effectiveness was verified. Then LQG control, which is a combination of an LQR and a Kalman filter was implemented in the machine and was used to produce wrinkle-free coated Nafion membrane in a roll-to-roll continuous fashion.

Chapter 7: Summary, Conclusions and Future Work

The ultimate aim of this work was to develop and design an automated, continuous, and low-cost MEA fabrication process for a proton exchange membrane fuel cell. A roll-to-roll membrane coating process was selected for its ability to make the entire process continuous. The ionomeric polymer membrane, a key component of a proton exchange membrane fuel cell, has been shown to rapidly absorb water from the liquid ink during direct coating. This rapid absorption of water results in swelling that deforms the membrane which in turn causes wrinkling manufacturing defects. We hypothesized that a model-based optimal control strategy would be beneficial to the MEA fabrication resulting in reducing the manufacturing defects and thus set out to design, develop, implement and test such a method.

Various aspects of MEA manufacturing were studied separately, starting with the development of transient, three-dimensional coupled mass transfer, heat transfer and solid mechanics models to describe membrane swelling. The model exhibited good agreement with experimental results; however its complexity and high computational cost make direct implementation in a model-based controller unfeasible. Reducing this multi-physics model to a zero-dimensional lumped model provided almost identical results when compared with the same experimental data. This reduction was possible due to uniformities encountered in a continuous roll-to-roll process.

Additionally a zeroth-order model was developed that describes the dynamics of the coating during drying. A coupling of the membrane swelling and the drying models was used to account for water movement across the membrane-coating interface. These combined models were then used to design and develop a continuous membrane-coating process.

The applied tractive forces and gradients in water content during continuous manufacturing give rise to wrinkles, which are the main defects during manufacture. A model that predicts these wrinkle associated defects was developed. Simulations from the developed models lead to the design of a continuous coating process that utilized pre-swelling of the uncoated membrane and a two-staged drying of the coated membrane. We built a pilot-scale coating machine to implement and test this coating methodology.

The combined membrane-coating model was modified to allow the implementation of a Linear-Quadratic-Gaussian type control, and this optimal control strategy was implemented on the pilot-scale coating line. Results from testing of the approach were very promising and strongly suggest further development of this method should be pursued.

In that light, additional quantification of characteristic material properties and the corresponding constants used in the models are needed, particularly, the mass and heat transfer coefficients used in this work as they are currently calculated from correlations. Additionally in our pilot-scale line, we employed a Doctor Blade to apply the coating because of its simplicity; however, scale-up may require faster coating techniques and it would be of benefit if additional coating techniques were tested using this approach. Also the feasibility of double-sided coating using this method should be explored as a critical next step in scale-up process leading to the mass manufacturing of MEAs.

While this work was primarily focused on application to Nafion due to its current commercial popularity, other ionomeric polymer membranes are available and the performance of these other membranes in this process is currently unknown and should be investigated. For cost considerations, the coating formulations used to test this process did not contain any catalyst and future research should be done to test the validity of the presented models with actual catalyst containing ink.

Finally, in the advanced optimal control strategy that was implemented, only the drying zone's water activity and temperature were controlled. Controlling additional variables, such as line speed and web tensions, may yield additional flexibility and benefit when scaling up this process for the industry.

In final conclusion, this work has demonstrated a methodology for producing a defect-free ionomeric polymer membrane in a continuous roll-to-roll manufacturing process. It includes the models, simulations and reference hardware designs that can be used as the basis for a successful scale-up effort to mass-produce high-quality low-cost proton exchange membrane fuel cell electrode assemblies.

Nomenclature

ε_v	volumetric strain (dimensionless)
μ_i	chemical potential (J mol^{-1})
$\nabla\mu$	chemical potential gradient (J mol^{-1} m^{-1})
∇T	temperature gradient (K m^{-1})
∇p	pressure gradient (N m^{-3})
$\boldsymbol{v}_0$	velocity of water (m s^{-1})
$\boldsymbol{N}_i$	molar flux of species i (mol m^{-2} s^{-1})
$R_{p,i}$	molar production or consumption rate of species i (mol m^{-3} s^{-1})
$\bar{S}_i$	partial molar entropy (J mol^{-1} K^{-1})
$\boldsymbol{N}_0$	water flux (mol m^{-2} s^{-1})
EW	equivalent weight (kg eq^{-1})
c_i	molar concentration of species i (mol m^{-3})
c_T	total concentration of the entire system (mol m^{-3})
D_{ij}	multicomponent diffusion coefficient (m^2 s^{-1})
D^T_i	thermal diffusion coefficient of species i (m^2 s^{-1})
G	Gibbs free energy (J)
n_i	number of moles or equivalents of species i (mol *or* eq)
m_i	number of moles of species i per mass of dry membrane (mol kg^{-1})
m_0	number of moles of water per mass of dry membrane (mol kg^{-1})
λ_j^θ	secondary reference state activity for j
E_{ij}	binary interaction parameter for species i and j
$\alpha_{\mu,ads}$	adsorption coefficient for a chemical potential driving force (mol^2 s kg^{-1} m^{-4})
$\alpha_{\mu,des}$	desorption coefficient for a chemical potential driving force (mol^2 s kg^{-1} m^{-4})
$\mu_{0,eq}$	chemical potential of water in the membrane when it has come to equilibrium with the surroundings (J mol^{-1})
$\mu_{0,s}$	chemical potential that is computed on the boundary (J mol^{-1})

λ	ratio of moles of water to equivalents of the membrane (mol eq^{-1})
$\mu_{0,eq}$	driving force for interfacial mass transport (J mol^{-1})
f_v	volume fraction of water (dimensionless)
$c_{0,eq}$	concentration of water at equilibrium with the environment (mol m^{-3})
$c_{0,s}$	membrane’s free surface concentration (mol m^{-3})
ρ	density of the membrane-water system (kg m^{-3})
c_p	specific heat of the membrane-water system (J kg^{-1} K^{-1})
$\mathbf{q}_\mathrm{c}$	heat flux due to conduction (J m^{-2} s^{-1})
$\mathbf{q}_\mathrm{d}$	heat flux due to mass transfer (J m^{-2} s^{-1})
$\mathbf{q}_\mathrm{x}$	heat flux compositional gradient (J m^{-2} s^{-1})
$\bar{H}_0$	enthalpy of water per mole (J mol^{-1})
$\bar{q}_{st}$	water’s isosteric heat of sorption or desorption during movement across the membrane-gas boundary (J mol^{-1})
T_s	surface temperature of the membrane (K)
T_{surr}	surrounding temperature (K)
k_a	thermal conductivity of air (W m^{-2} K^{-1})
$c_{p,a}$	specific heat of air (J kg^{-1} K^{-1})
v_a	kinematic viscosity of air (m^2 s^{-1})
μ_a	dynamic viscosity of air (kg m^{-1} s^{-1})
L	length of the membrane in the direction of air flow (m)
v	air flow free stream velocity (m s^{-1})
$c_{p,0}$	specific heat of water (J kg^{-1} K^{-1})
$c_{p,PTFE}$	specific heat of PTFE (J kg^{-1} K^{-1})
$\bar{h}_{fg}$	temperature-dependent heat of vaporization of water (J mol^{-1})
$\mathbf{T}$	stress tensor (N m^{-2})
$\mathbf{b}$	body force per unit mass (N kg^{-1})
$\mathbf{C}$	tensor of elasticity (N m^{-2})
ϵ	strain tensor (dimensionless)

β	linear coefficient of thermal expansion for the membrane-water system (m K^{-1})
$\bar{V}_0$	partial molar volume of water (m^3 mol^{-1})
$\boldsymbol{v}_i$	velocity of the moving species i (m s^{-1})
ρ_m	dry density of the membrane (kg m^{-3})
K	bulk modulus of the membrane (N m^{-2})
M_0	molar mass of water (kg mol^{-1})
ρ_m	density of the membrane (kg m^{-3})
ρ_0	density of water (kg m^{-3})
$\boldsymbol{V}$	volume of the domain (m^3)
$\boldsymbol{A}$	surface area in Γ over which drying is considered (m^2)
Bi_m	mass transfer Biot number (dimensionless)
Bi_h	heat transfer Biot number (dimensionless)
m_{0c}	ratio of moles of water in the coating to mass of dried coating (mol/kg)
ρ_s	density of the dry coating (kg m^{-3})
$\boldsymbol{A_c}$	area over which the coating drying is considered (m^2)
$\boldsymbol{V_c}$	volume of the coating (m^3)
α_{coat}	mass transfer coefficient for the coating (m s^{-1})
$c_{0c,surr}$	surroundings' liquid water concentration for coating (mol m^{-3})
$\mathcal{D}_{0,air}$	diffusion coefficient of water in air (m^2 s^{-1})
v_a	kinematic viscosity of air (m^2 s^{-1})
L_c	length of the coating in the direction of air flow (m)
v	air's free stream velocity (m s^{-1})
ρ_{coat}	effective density of the coating (kg m^{-3})
$c_{p,coat}$	specific heat of the coating (J kg^{-1} K^{-1})
T_{surr}	temperature of the surroundings (K)
$\mathcal{D}_{0,coat}$	diffusion coefficient of water in the coating (m^2 s^{-1})
ρ_{eff}	coating-membrane system's density (kg m^{-3})
$c_{p,eff}$	coating-membrane system's specific heat capacity (J kg^{-1} K^{-1})

ε_t	porosity of dried coating (dimensionless)
δ	constrictivity of dried coating (dimensionless)
τ	tortuosity of dried coating (dimensionless)
m	the number of half-waves in the membrane’s buckled shape in the x direction
n	the number of half-waves in the membrane’s buckled shape in the y direction
α_c	mass transport barrier for membrane with concentration driving force (m s^{-1})
$c_{0c,surr\ 1}$	surrounding water concentration for the coating in zone 1 (mol m^{-3})
$c_{0,eq\ 1}$	membrane’s equilibrated water concentration of the membrane in zone 1 (mol m^{-3})
$T_{surr\ 1}$	first zone’s temperature (K)
V_0	reference volume of the dry membrane (m^3)

Subscripts

0	water
m	membrane
c	coating
i	species index

Bibliography

Athans, Michael. "The Role and Use of the Stochastic Linear-Quadratic-Gaussian Problem in Control System Design." *IEEE Transactions on Automatic Control* AC-16, no. 6 (December 1971): 529-552.

Barbir, F. *PEM Fuel Cells-Theory and Practice*. New York: Elsevier, 2005.

Beisel, J A, and J K Good. "The Instability of Webs in Transport." *Journal of Applied Mechanics* 78, no. 1: 011001.

Bird, Robert Byron, Warren E Stewart, and Edwin N Lightfoot. *Transport Phenomena*. New York, USA: John Wiley and Sons, Inc. , 2007.

Burnett, D J, A R Garcia, and F Thielmann. "Measuring Moisture Sorption and Diffusion Kinetics on Proton Exchange Membranes Using a Gravimetric Vapor Sorption Apparatus." *Journal of Power Sources* 160, no. 1 (2006): 426-430.

Devaraj, Vikram. "Compression/Injection Molding of Bipolar Plates for Proton Exchange Membrane Fuel Cells." Master's thesis, The University of Texas at Austin, 2009.

Dubau, L, C Coutanceau, E Garnier, J M Leger, and C Lamy. "Electrooxidation of Methanol at Platinum-Ruthenium Catalysts Prepared from Colloidal Precursors: Atomic Composition and Temperature Effects." *Journal of Applied Electrochemistry* 33 (2003): 419-429.

DuPont. *Product Information: DuPont Nafion PFS Membranes*. Fayetteville, NC, 2004.

"8020." The Industrial Erector Set. Accessed 2012. http://8020.net.

FCT. Fuel Cell Technologies. Accessed 2012. http://www.fuelcelltoday.com.

Franklin, Gene F, J David Powell, and Abbas Emami-Naeini. *Feedback Control of Dynamic Systems*. Massachusetts: Addison-Wesley Publishing Company, 1988.

Frey, T, K A Friedrich, L Jorissen, and J Garche. "Preparation of Direct Methanol Fuel Cells by Defined Multilayer Structures." *Journal of Electrochemical Society* 152, no. 3 (2005): A545.

Ge, S, X Li, B Yi, and I M Hsing. "Absorption, Desorption, and Transport of Water in Polymer Electrolyte Membranes for Fuel Cells." *Journal of The Electrochemical Society* 152, no. 6 (2005): A1149.

Grathwohl, Peter. *Diffusion in Natural Porous Media: Contaminant Transport, Sorption/ Desorption and Dissolution Kinetics*. Massachusetts: Kluwer Academic Publishers, 1998.

Hayre, Ryan. *Fuel Cell Fundamentals*. N.p.: John Wiley & Sons, 2006.

Higuchi, Eiji, Hiroyuki Uchida, and Masahiro Watanabe. “Effect of Loading Level in Platinum-Dispersed Carbon Black Electrocatalysts on Oxygen Reduction Activity Evaluated by Rotating Disk Electrode.” *Journal of Electroanalytical Chemistry* 583, no. 1 (2005): 69-76.

Hsu, C H, and C C Wan. “An Innovative Process for PEMFC Electrodes Using the Expansion of Nafion Film.” *Journal of Power Sources* 115 (2003): 268-273.

Huang, De Chin, Pei Jung Yu, Feng Jiin Liu, Shu Ling Huang, Kan Lin Hsueh, Yen Cho Chen, Chun Hsing Wu, Wen Chen Chang, and Fang Hei Tsau. “Effect of Dispersion Solvent in Catalyst Ink on Proton Exchange Membrane Fuel Cell Performance.” *International Journal of Electrochemical Science* 6 (2011): 2551-2565.

Huang, Xinyu, Roham Solasi, Yue Zou, Matthew Feshler, Kenneth Reifsnider, David Condit, Sergei Burlatsky, and Thomas Madden. “Mechanical Endurance of Polymer Electrolyte Membrane and PEM Fuel Cell Durability.” *Journal of Polymer Science Part B: Polymer Physics* 44, no. 16 (2006): 2346-2357.

Incropera, F P, and D P DeWitt. *Fundamentals of Heat and Mass Transfer*. 5th ed. New Jersey, USA: John Wiley and Sons, 2007.

Jones, Deborah J, and Jacques Roziere. “Advances in the Development of Inorganic-Organic Membranes for Fuel Cell Applications.” *Advances in Polymer Science* 215 (2008): 219-264.

Joon, K. “Fuel Cells - a 21st Century Power System.” *Journal of Power Sources* 71 (1998): 12-18.

Kalman, R E. “A New Approach to Linear Filtering and Prediction Problems.” *Journal of Basic Engineering* 82, no. 1 (1960): 35-45.

Khandelwal, M, and M Mench. “Direct Measurement of Through-Plane Thermal Conductivity and Contact Resistance in Fuel Cell Materials.” *Journal of Power Sources* 161, no. 2 (2006): 1106-1115.

Koraishy, Babar Masood. “Continuous Manufacturing of Direct Methanol Fuel Cell Membrane Electrode Assemblies.” PhD diss., The University of Texas at Austin, 2010.

Kusoglu, A, A Karlsson, and M Santare. “Mechanical Response of Fuel Cell Membranes Subjected to a Hygro-Thermal Cycle.” *Journal of Power Sources* 161, no. 2 (2006).

Kwakernaak, Huivert, and Raphel Sivan. *Linear Optimal Control Systems*. New York: Wiley-

Interscience, 1972.

Ladewig, Bradlwy P. “Physical and Electrochemical Characterization of Nanocomposite Membranes of Nafion and Functionalized Silicon Oxide.” *Chemistry of Materials* 19, no. 9 (2007): 2372-2381.

Larminie, James, and Andrew Dicks. *Fuel Cell Systems Explained*. N.p.: John Wiley & Sons, 2000.

Laser-View Technologies. Accessed 2012. http://www.laser-view.com.

Lindermeir, A, G Rosenthal, U Kunz, and U Hoffmann. “On the Question of MEA Preparation for DMFCs.” *Journal of Power Sources* 129, no. 2 (2004): 180-187.

Liu, Zhixiang, Zongqiang Mao, and Cheng Wang. “A Two Dimensional Partial Flooding Model for PEMFC.” *Journal of Power Sources* 158, no. 2 (2006): 1229-1239.

Majsztrik, P, A Bocarsly, and J Benziger. “Water Permeation Through Nafion Membranes: The Role of Water Activity.” *The Journal of Physical Chemistry, B* 112, no. 51 (2008): 16280-9.

Malvern, L E. *Introduction to the Mechanics of a Continuous Medium*. Englewood Cliffs, New Jersey: Prentice-Hall, Inc. , 1969.

Mao, Qing, Gongquan Sun, Suli Wang, Hai Sun, Guoxiong Wang, Yan Gao, Aiwei Ye, Yang Tian, and Qin Xin. “Comparative Studies of Configurations and Preparation Methods for Direct Methanol Fuel Cell Electrodes.” *Electrochimica Acta* 52, no. 24 (2007): 6763-6770.

Maybeck, Peter S. *Stochastic Models, Estimation and Control Vol. 2 & Vol. 3*. New York: Academic Press, 1982.

Mehta, V, and J S Cooper. “Review and Analysis of PEM Fuel Cell Design and Manufacturing.” *Journal of Power Sources* 114, no. 1 (2003): 32-53.

Mehta, Viral S. “Analysis of Design and Manufacturing of Proton Exchange Membrane Fuel Cell.” Master’s thesis, University of Washington, 2002.

Meyers, J P, and J Newman. “Simulation of the Direct Methanol Fuel Cell.” *Journal of The Electrochemical Society* 149, no. 6 (2002): A718-A728.

Mills, Anthony F. *Mass Transfer*. 2nd ed. Upper Saddle River, NJ, USA: Prentice Hall, 2001.

Moin, Parviz. *Fundamentals of Engineering Numerical Analysis*. Cambridge: Cambridge University Press, 2010.

Mortenson, Michael E. *Geometric Transformations*. New York, USA: Industrial Press Inc. , 1995.

Newman, John, and Karen E Thomas-Alyea. *Electrochemical Systems*. 3rd ed. New Jersey, USA: John Wiley and Sons, Inc., 2004.

Ogata, Katsuhiko. *Modern Control Engineering*. 3rd ed. New Jersey: Prentice Hall, 1997.

Omega. Accessed 2012. http://www.omega.com.

Park, In Su, Wen Li, and Arumugam Manthiram. "Fabrication of Catalyst-Coated Membrane-Electrode Assemblies by Doctor Blade Method and Their Performance in Fuel Cells." *Journal of Power Sources* 195 (2010): 7078-7082.

Prabhuram, J, X Wang, C L Hui, and I Ming Hsing. "Synthesis and Characterization of Surfactant-Stabilized Pt/C Nanocatalysts for Fuel Cell Applications." *Journal of Physical Chemistry B* 107: 11057-11064.

Prasanna, M, E A Cho, T H Lim, and I H Oh. "Effects of MEA fabrication method on durability of polymer electrolyte membrane fuel cells." *Electrochimica Acta* 53, no. 16 (2008): 5434-5441.

Roark, Raymond J, and Warren C Young. *Formulas for Stress and Strain*. New York, USA: McGraw-Hill Book Company, 1975.

Satterfield, M B, and J B Benziger. "Non-Fickian Water Vapor Sorption Dynamics by Nafion Membranes." *The Journal of Physical Chemistry* 112, no. 12 (2008): 3693-704.

Shen, Chunhui, Mu Pan, Qiong Wu, and Runzhang Yuan. "Performance of an Aluminate Cement/Graphite Conductive Composite Bipolar Plate." *Journal of Power Sources* 159, no. 2 (2006): 1078-1083.

Silverman, Timothy J. "Dynamic Modeling of Membrane Swelling in Fuel Cell Manufacturing." PhD diss., The University of Texas at Austin, 2010.

Solasi, Roham, Yue Zou, Xinyu Huang, Kenneth Reifsnider, and David Condit. "On Mechanical Behavior and In-Plane Modeling of Constrained PEM Fuel Cell Membranes Subjected to Hydration and Temperature Cycles." *Journal of Power Sources* 167, no. 2 (2007): 366-377.

Solasi, Roham, Yue Zou, Xinyu Huang, and Kenneth Reifsnider. "A Time and Hydration Dependent Viscoplastic Model for Polyelectrolyte Membranes in Fuel Cells." *Mechanics of Time Dependent Materials* 12, no. 1 (2008): 15-30.

Springer, T E, T A Zawodzinski, and S Gottesfeld. “Polymer Electrolyte Fuel Cell Model.” *Journal of the Electrochemical Society* 138, no. 8 (1991): 2334.

Srinivasan, Supramaniam. *Fuel Cells: From Fundamentals to Applications*. New York, USA: Springer, 2006.

Strang, Gilbert, and George Fix. *An Analysis of the Finite Element Method*. 2nd ed. Wellesley, MA: Wellesley-Cambridge Press, 2008.

Takamatsu, T, and A Eisenberg. “Densities and Expansion Coefficients of Nafion Polymers.” *Journal of Applied Polymer Science* 24, no. 11 (1979): 2221-2235.

Tang, Y, A Karlsson, M Santare, M Gilbert, S Cleghorn, and W Johnson. “An Experimental Investigation of Humidity and Temperature Effects on the Mechanical Properties of Perfluorosolfonic Acid Membrane.” *Materials Science and Engineering: A* 425, no. (1-2) (June 2006): 297-304.

Timoshenko, S P. *Theory of Plates and Shells*. New York, USA: McGraw-Hill Book Company Inc., 1940.

Timoshenko, S P, and J M Gere. *Theory of Elastic Stability*. 2nd ed. New York, USA: McGraw-Hill Book Company, 1961.

Timoshenko, S P, and J N Goodier. *Theory of Elasticity*. 3rd ed. New York, USA: McGraw-Hill Book Company, 1970.

Tsuchiya, Haruki, and Osamu Kobayashi. “Mass production cost of PEM fuel cell by learning curve.” *International Journal of Hydrogen Energy* 29 (2004): 985-990. Accessed September 8, 2010.

Verwer, J G, and J M Sans-Serna. “Convergence of Method of Lines Approximations to Partial Differential Equations.” *Computing* 33, no. 3-4 (1984): 297-313.

Vielstich, Wolf, Arnold Lamm, and Hubert A Gasteiger. *Handbook of Fuel Cells: Fundamentals, Technology, Applications*. Vol. 1. New York, USA: John Wiley and Sons, 2003.

Weber, A Z, and J Newman. “Device and Materials Modeling in PEM Fuel Cells.” *Topics in Applied Physics* 113 (2009).

———. “A Theoretical Study of Membrane Constraint in Polymer-Electrolyte Fuel Cells.” *AIChE Journal* 50, no. 12 (2004): 3215-3226.

———. “Transport in Polymer-Electrolyte Membranes.” *Journal of the Electrochemical Society*

151 (2004): A311.

Wheeler, D, and G Sverdrup. *2007 Status of Manufacturing: Polymer Electrolyte Membrane (PEM) Fuel Cells*. NTIS/GPO 924988.

Wu, H, P Berg, and X Li. “Non-Isothermal Transient Modeling of Water Transport in PEM Fuel Cells.” *Journal of Power Sources* 165, no. 1 (2007): 232-243.

Xie, Zhong, Xinsheng Zhao, Makoto Adachi, Xhiqing Shi, Tetsuya Mashio, Atsushi Ohma, Kazuhiko Shinohara, Steven Holdcraft, and Titichai Navessin. “Fuel Cell Cathode Catalyst Layers from ‘Green’ Catalyst Inks.” *Energy and Environmental Science* 1 (2008): 184-193.

Zawodzinski, T, C Derouin, and S Radzinski. “Water Uptake by and Transport Through Nafion 117 Membranes.” *Journal of the Electrochemical Society* 140, no. 4 (1993).

Vita

Vikram Devaraj was born in Madras - India, the son of Kalyani Devaraj and Devaraj Ranganathan. He completed his high school at Chinmaya Vidyalaya, Madras, India in 2003 and graduated from Sri Venkateswara College of Engineering, Madras, India with a Bachelor's degree in Mechanical Engineering in 2007. After starting graduate school at The University of Texas at Austin in 2007, he graduated with an MS in 2007 and a PhD in 2012.

Vikram loves entrepreneurship, scuba diving, aeromodelling, and automatic watches.

Permanent address:
"GEETHAM"
Old #52, Rajeswari Street
Metha Nagar, Chennai
Tamil Nadu, India – 600 069
Ph: +91-44 23740722
Email: devarajan.vikram@gmail.com
vikram@utexas.edu